FABRICATION AND CHARACTERIZATION OF NBN
INAS/GASB/B-AL(X)GA(1-X)SB TYPE-II SUPERLATTICE DETECTORS
WITH DUAL-COLOR DETECTION IN MWIR

A THESIS SUBMITTED TO
THE GRADUATE SCHOOL OF NATURAL AND APPLIED SCIENCES
OF
MIDDLE EAST TECHNICAL UNIVERSITY

BY

UTKU ÇEKMEZ

IN PARTIAL FULFILLMENT OF THE REQUIREMENTS
FOR
THE DEGREE OF MASTER OF SCIENCE
IN
MICRO AND NANOTECHNOLOGY

APRIL 2022

Approval of the thesis:

**FABRICATION AND CHARACTERIZATION OF NBN
INAS/GASB/B-AL(X)GA(1-X)SB TYPE-II SUPERLATTICE DETECTORS
WITH DUAL-COLOR DETECTION IN MWIR**

submitted by **UTKU ÇEKMEZ** in partial fulfillment of the requirements for the
degree of **Master of Science** in **Micro and Nanotechnology, Middle East
Technical University** by,

Prof. Dr. Halil Kalıpçılar
Dean, Graduate School of **Natural and Applied Sciences**   _____

Prof. Dr. Deniz Üner
Head of the Department, **Micro and Nanotechnology**   _____

Prof. Dr. Tayfun Akın
Supervisor, **Micro and Nanotechnology Dept., METU**   _____

Assoc. Prof. Dr. Kıvanç Azgın
Co-Supervisor, **Mechanical Eng. Dept., METU**   _____

Examining Committee Members:

Prof. Dr. Haluk Külah
Electrical and Electronics Eng. Dept., METU   _____

Prof. Dr. Tayfun Akın
Electrical and Electronics Eng. Dept., METU   _____

Prof. Dr. Yüksel Ergün
Physics Dept., Eskişehir Technical University   _____

Assoc. Prof. Dr. Alpan Bek
Physics Dept., METU   _____

Assoc. Prof. Dr. Serdar Kocaman
Electrical and Electronics Eng. Dept., METU   _____

Date: 28.04.2022

I hereby declare that all information in this document has been obtained and presented in accordance with academic rules and ethical conduct. I also declare that, as required by these rules and conduct, I have fully cited and referenced all material and results that are not original to this work.

Name Last name : Utku Çekmez

Signature :

ABSTRACT

FABRICATION AND CHARACTERIZATION OF NBN INAS/GASB/B-AL(X)GA(1-X)SB TYPE-II SUPERLATTICE DETECTORS WITH DUAL-COLOR DETECTION IN MWIR

Çekmez, Utku
Master of Science, Micro and Nanotechnology
Supervisor: Prof. Dr. Tayfun Akın
Co-Supervisor: Assoc. Prof. Dr. Kıvanç Azgın

April 2022, 112 pages

Type-II superlattice detectors with nBn structure made it possible to detect at higher temperatures due to the suppressing of the dark current components originating from Shockley-Read-Hall (SRH). In this context, the $Al_xGa_{1-x}Sb$ layer with wider band-gap energy was designed to act as an electron barrier between the n-doped N-Structure InAs/AlSb/GaSb type-II superlattice layers, whose active layers are capable of dual-color detection at mid-wavelength. In this thesis work, the fabrication processes of the growth design were carried out in pixel size. The test detectors with mesa form and different perimeter-to-area ratios (100×100, 150×150, 200×200, 300×300 μm^2) were acquired by making the etching optimization known as shallow etch (T1) and deep etch (T2) in METU-MEMS Center.

The electrical and optical characterizations of the samples were completed by making the temperature-dependent dark current density measurements and the blackbody responsivity measurements. Keithley 2635B SMU was used in dark

current density measurement, but since the lowest current value that can measure for the device is 10^{-12} A, the dark current density values of the samples could not be measured properly at lower temperatures than 160 K. Therefore, the dark current density analysis of 300 μm pixels from T1 and T2 were done at 160 K. The minimum dark current levels were obtained as 7.32×10^{-12} A and 4.74×10^{-10} A at 0.25 V for the shallow etch and the deep etch, respectively. Although low-level dark current values were achieved at low voltage bias, the dark current levels of the samples were found as 1.85×10^{-6} A and 1.44×10^{-6} A for the shallow etch and the deep etch, respectively, at 2 V, which the high photoresponsivity exists for mid-wavelength. The differential-resistance $\times$ detector area ($R_0.A$) at 0.25 V were calculated as 7.86×10^7 $\Omega.cm^2$ for shallow etch and 2.02×10^5 $\Omega.cm^2$ for deep etch.

The measured spectral responsivity data sent by the manufacturer company of the structure was used between 3-5 μm wavelength range and 2 V voltage bias for optical calculation. The blackbody responsivity measurements of the samples were obtained at 800 K (λ_{peak}=3.6 μm) with cavity blackbody. The peak responsivity values of the samples were found as 1.5 A/W and 0.46 A/W at the λ_{peak} wavelength for the T1 and T2 using the photocurrents of the samples at 2 V voltage bias and spectral responsivity data. The external quantum efficiency and thermal noise limited specific detectivity of the samples were estimated 50% and 1.7×10^{11} Jones for T1 and 15% and 5×10^{10} Jones for T2.

The dark noise values of the samples were calculated as theoretically by using the differential resistance values and the dark current values at 2 V. The thermal noise and the shot noise values were found as 1.63×10^{-13} A/$\sqrt{Hz}$ and 7.70×10^{-13} A/$\sqrt{Hz}$ for T1, 1.51×10^{-13} A/$\sqrt{Hz}$ and 6.79×10^{-13} A/$\sqrt{Hz}$ for T2.

Keywords: T2SL, nBn, Dual-color, Barrier, InAs/GaSb/B-Al$_x$Ga$_{1-x}$Sb

ÖZ

ORTA DALGA BOYUNDA ÇİFT RENKLİ ALGILAMA YAPABİLEN NBN INAS/GASB/B-AL(X)GA(1-X)SB TİP-II SÜPERÖRGÜ DEDEKTÖRLERİN FABRİKASYONU VE KARAKTERİZASYONU

Çekmez, Utku
Yüksek Lisans, Mikro ve Nanoteknoloji
Tez Yöneticisi: Prof. Dr. Tayfun Akın
Ortak Tez Yöneticisi: Doç. Dr. Kıvanç Azgın

Nisan 2022, 112 sayfa

nBn yapılı Tip-II süperörgü dedektörler Shockley-Read-Hall (SRH) kaynaklı karanlık akım bileşenlerini baskılaması sebebiyle daha yüksek sıcaklıklarda algılama yapabilmeyi mümkün kılmıştır. Bu kapsamda aktif yüzeyleri orta-dalga boyunda çift renkli algılama yapabilen, n-tipi malzeme katkılı N-tasarım InAs/AlSb/GaSb tip-II süperörgü katmanlar arasına geniş bant enerjisine sahip $Al_xGa_{1-x}Sb$ katman bir elektron bariyer görevi görecek şekilde tasarlanmıştır. Bu tez çalışmasında büyütülen yapının piksel boyutunda fabrikasyon adımları gerçekleştirilmiştir. Sığ aşındırma (T1) ve derin aşındırma (T2) olarak bilinen aşındırma optimizasyonları yapılarak mesa yapısında ve farklı alan-çevre oranlarına sahip test dedektörleri (100×100, 150×150, 200×200, 300×300 μm^2) ODTÜ-MEMS Merkezi'nde elde edilmiştir.

Sıcaklığa bağlı karanlık akım yoğunluğu ölçümleri ve karacisim tepkisellik ölçümleri yapılarak örneklerin elektriksel ve optik karakterizasyonları tamamlanmıştır. Karanlık akım yoğunluğu ölçümlerinde Keithley 2635B SMU kullanılmış, fakat cihazın ölçebileceği minimum akım seviyesi 10^{-12} A olduğundan

160 K'den düşük sıcaklıklarda karanlık akım yoğunluğu değerleri düzgün şekilde ölçülememiştir. Bu sebeple T1 ve T2 örneklerindeki 300 μm'lik piksellerin karanlık akım yoğunluğu analizleri 160 K'de yapılmıştır. Sığ aşındırma ve derin aşındırma örnekleri için en düşük karanlık akım seviyeleri 0.25 V'ta sırasıyla 7.32×10^{-12} A ve 4.74×10^{-10} A olarak elde edilmiştir. Düşük voltaj değerlerinde düşük karanlık akım seviyelerine ulaşılsa da, orta dalgaboyunda yüksek fototepkiselliğin olduğu 2 V'ta sığ aşındırma ve derin aşındırma için örneklerin karanlık akım değerleri sırasıyla 1.85×10^{-6} A ve 1.44×10^{-6} A olarak bulunmuştur. 0.25 V'taki diferansiyel direnç × dedektör alanı ($R_0.A$) değerleri sığ aşındırma için 7.86×10^{7} $\Omega.cm^2$ ve derin aşındırma için 2.02×10^{5} $\Omega.cm^2$ olarak hesaplanmıştır.

Optik hesaplamalar için yapıyı üreten firmadan gönderilen 3-5 μm aralığındaki ve 2 V kutuplama voltajında ölçülmüş spektral tepkisellik verileri kullanılmıştır. Örneklerin karacisim tepkisellik ölçümleri 800 K'de (λ_{tepe}=3.6 μm) oyuk karacisim ile yapılmıştır. Örneklerin λ_{tepe} dalga boyundaki tepe tepkisellik değerleri, 2 V'taki fotoakım değerleri ve spektral tepkisellik verileri kullanılarak T1 ve T2 için 1.5 A/W ve 0.46 A/W olarak bulunmuştur. Örneklerin harici kuantum verimliliği ve termal gürültü limitli spesifik dedektivite değerleri T1 için %50 ve 1.7×10^{11} Jones, T2 için %15 ve 5×10^{10} Jones olarak hesaplanmıştır.

Örneklerin karanlık gürültü değerleri 2 V'taki diferansiyel direnç ve karanlık akım değerleri kullanılarak teorik olarak hesaplanmıştır. T1 için termal gürültü ve shot gürültü değerleri 1.63×10^{-13} A/$\sqrt{Hz}$ ve 7.70×10^{-13} A/$\sqrt{Hz}$, T2 için 1.51×10^{-13} A/$\sqrt{Hz}$ ve 6.79×10^{-13} A/$\sqrt{Hz}$ olarak hesaplanmıştır.

Anahtar Kelimeler: T2SL, nBn, Çift-renk, Bariyer, InAs/GaSb/B-Al$_x$Ga$_{1-x}$Sb

To my family…

ACKNOWLEDGMENTS

I would like to express my gratitude to my supervisor, Prof. Dr. Tayfun Akın, and co-supervisor Assoc. Prof. Dr. Kıvanç Azgın for their guidance, advice, criticism, encouragements and insight throughout the research.

I would like to thank Prof. Dr. Yüksel Ergün and Prof. Dr. Mustafa Hoştut for sharing their precious design with me and allowing me to study on it, their invaluable suggestions and comments.

I also want to thank Dr. Selçuk Özer for sharing his extensive knowledge and experience at every stage of the thesis study.

I would like to thank Orhan Akar for his enlightening knowledge, support, and help in the cleanroom.

I would like to express my gratitude to my colleagues, Kübra Ceren Hancı, Semih Çavdar and, most of all Murat Artuç for their excellent friendship, motivating me throughout the study.

I am thankful to Ahmet Murat Yağcı and Kadir Ulak for their invaluable support during the wire-bonding and the packaging steps.

I am pleased to Seval Şahin and Adem Saraç for helping me receive training the devices and sharing their extensive process knowledge during the fabrication steps of the thesis study.

I would like to thank Tolga Orçun Şengöz for helping with optical measurements.

Last but best, I would like to express my deepest love and appreciation to my family for always being with me.

TABLE OF CONTENTS

LIST OF TABLES

TABLES

xiv

CHAPTER 1

INTRODUCTION

The region is known as the "Infrared Spectrum" which corresponds to electromagnetic waves between 0.7 µm and 1000 µm, emitted from objects whose temperatures are above 0 K. The infrared imaging is widely used in many areas such as civilian [1] [2] and military [3] applications.

The discovery of infrared imaging was based on the study of Sir William Herschel in 1800 [3]. After that, the thermoelectric effect was revealed by Seebeck in 1820s [4]. A few years later, Nobili developed the first thermopile by connecting numbers of Seebeck's thermocouples [4]. The infrared imaging was stepped into a new age with the discovery and the enhancement of bolometer by Langley in the late 1800s [5]. The first photon-based detector, known as a photoconductor, was developed by Case in 1917 [6]. The emergence of today's modern infrared detectors has accelerated with The Second World War. The developments of InSb and HgCdTe, known as narrow band-gap semiconductors, have facilitated the emergence of infrared photon detectors with high performance. In 1970, Esaki and Tzu published the first proposal of the new infrared structure named "Superlattice" [7], and it has evolved the infrared technology to the quantum well-infrared photodetector (QWIP) and type-II superlattice (T2SL) detectors. Even though HgCdTe based photon detectors are dominance the market because of their superior electrical and optical parameters, type-II superlattice detectors can be a significant alternative to HgCdTe photodetectors since advantages such as adjustable operation wavelength from SWIR to VLWIR [8], lower production cost, better uniformity, and higher electron effective mass that leads to lower dark current [9]. Laboratories worldwide have started to work on this new type of photodetector. Different structures were designed

and performed, such as p-i-n, nBn, N-structure, CBIRD (complementary barrier infrared detector) benefitting from the advances of MBE technology. In particular, the structures with the barrier layer (nBn, XBn, pBp) gave excellent results.

Therefore, the main purpose of this thesis study is to fabricate the test detectors with the different pixels sizes of nBn structured T2SL detector, which is capable of dual-color detection in the MWIR band and make electro-optical characterization. In the first chapter of the thesis, the history of infrared detection is briefly explained. Then, the fundamental laws of the infrared radiation, the term of the atmospheric transmission window, the infrared detector types, and the performance parameters of photon detectors are presented, respectively. Finally, the objective of the thesis and thesis organization are indicated at the end of the chapter.

1.1   Fundamentals of Infrared Radiation

The infrared waves also follow Maxwell's Law as it is a particular region of the electromagnetic wavelength. Maxwell has said if the particles inside the material are accelerated, they cause the release of energy. Based on this law, when the temperature of an object is increased, the charge carriers of it will be accelerated and thus, the energy called radiation is emitted from the object. The relationship between the released energy and the wavelength of it can be given as,

$$E = \frac{hc}{\lambda}$$
(1.1)

where λ is the wavelength, c is the speed of the light, h is Planck's constant.

1.2   Blackbody Radiation

The interaction of the incident radiation with the objects results in absorbance (α), reflectance (ρ), or transmittance (τ) [10]. Kirchoff has formulated the relationship as Kirchoff Law of thermal radiation, which is,

$$\alpha + \rho + \tau = 1 \tag{1.2}$$

Moreover, the blackbody has been defined as an ideal object that absorbs all incident electromagnetic radiation at any wavelengths by Kirchoff with the same law. That means, there is no reflection ($\rho = 0$) or transmission ($\tau = 0$) from the black bodies. Furthermore, the emissivity (ε) of the blackbody is equal to the absorbance (α) of it since the ratio of the absorbed radiation must be equal to the ratio of the re-emitted radiation from an object or a surface at thermal equilibrium. Therefore, the emissivity of the blackbody is equal to 1, and this re-emitted radiation is called *blackbody radiation*. In order to define the emissivity of an object, the term exitance of object and blackbody should be known. The ratio of the emitted radiation power from the object per unit area of the object, which is known as object exitance to the emitted radiation power from the blackbody per unit area of the blackbody, which is known as blackbody exitance at the same temperature and the same wavelength corresponds to the emissivity of the object.

$$Emissivity\ (\varepsilon) = \frac{M_{object}}{M_{blackbody}} \tag{1.3}$$

The spectral radiant exitance of a blackbody at a certain wavelength and a certain temperature above absolute zero is stated by Planck's Radiation Law and given as

$$M(\lambda, T) = \frac{2\pi hc^2}{\lambda^5} \frac{1}{e^{hc/\lambda k_B T} - 1} \tag{1.4}$$

where $M(\lambda, T)$ is the spectral radiance exitance in terms of W/cm^2.µm, h is the Planck constant, c is the speed of the light, λ is the wavelength of the radiation, k_B is the Boltzmann constant, and T is the temperature of the blackbody in K. By dividing spectral radiant exitance to the energy of a photon, the spectral photon radiant exitance can be found in unit of photons/cm^2.sec.µm. Moreover, the emitted energy of the blackbody can be defined as the spectral radiance $L(\lambda, T)$ too. The relationship between the spectral radiant exitance (W/cm^2.µm) and the spectral radiance (W/sr.cm^2.µm) is stated as

$$M(\lambda, T) = \pi . L(\lambda, T) \qquad (1.5)$$

The changing of the spectral exitance of the blackbody with respect to the wavelength can be seen in Figure 1.1 for several temperatures. As seen from the figure, the emitted radiant energy of the blackbody increases with the temperature, and the wavelength of the peak exitance shifts to the lower wavelength.
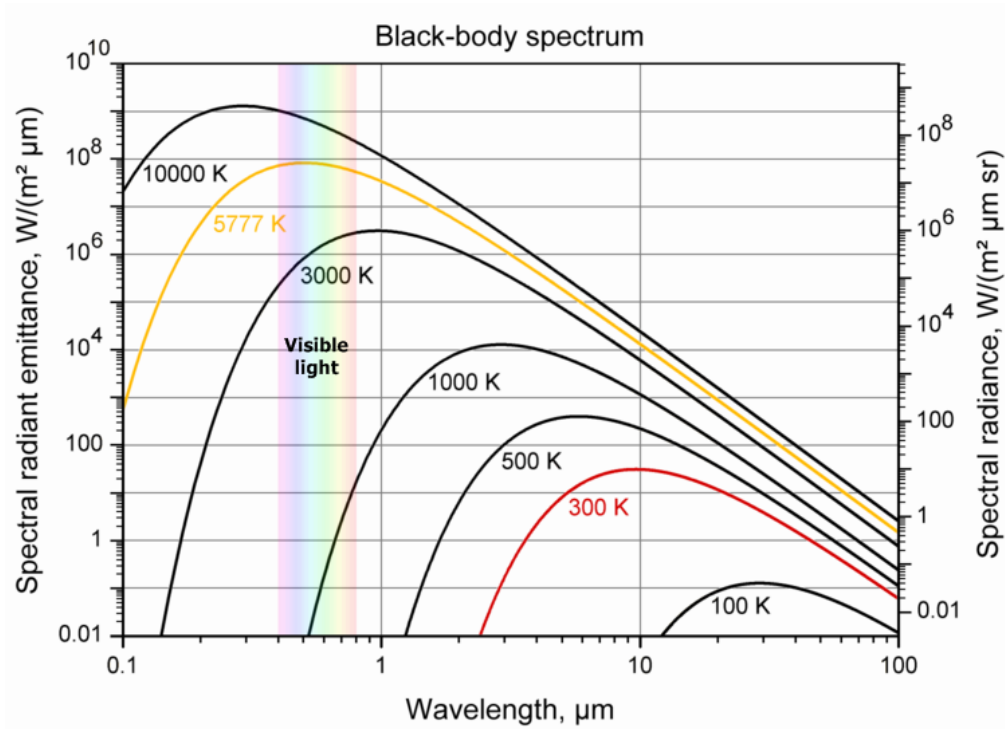
Figure 1.1: Spectral radiant emittance of a blackbody at different temperatures [11].

The wavelength of the blackbody peak emittance is calculated by Wien's Displacement Law for a certain temperature. When the spectral radiant exitance of Planck's Law is differentiated with respect to λ, the wavelength of the maximum emission (λ_{peak}) is found as,

$$\lambda_{peak} = \frac{2898 \ \mu m . K}{T \ [K]} \qquad (1.6)$$

The peak emission wavelength of the objects at room temperature (300K) corresponds to around 10 µm. The Stefan-Boltzmann Law defines the total radiated

energy of blackbody at temperature T by integrating Planck's Law for all wavelengths from 0 to ∞.

$$M_{total} = \sigma . T^4 \tag{1.7}$$

where $\sigma = 5.67 \times 10^{-8}$ W/m^2.K^4 is the Stefan Boltzmann constant, T is the temperature of the blackbody.

1.2.1 Atmospheric Transmission

The atmosphere has a crucial role in infrared imaging systems since the propagation medium of infrared radiation is air. The emitted radiation by the target affects from the atmosphere that is the background of the target. Moreover, the emitted radiation from the object attenuates because of either scattering of infrared rays by particles or absorption by the atmospheric gas molecules such as H_2O, CO_2, O_3, N_2, N_2O, NH_3, and CH_4 during the propagation.

The scattering phenomenon occurs by changing the direction of the incoming rays due to the interaction of the photons with the particles such as dust, fog, and smog. The scattering mechanism can be either Rayleigh scattering or Mie scattering depending on how large the size of the particles than the wavelength of the incident radiation. The smaller particle size from the wavelength leads to Rayleigh scattering, and its rate is inversely proportional with the wavelength, whereas Mie scattering, which is nonselective with respect to the wavelength, occurs if the particle size is larger than the wavelength of incident radiation. Therefore, infrared imaging is more useful than visible imaging for scattering condition [12].

The absorption of the emitted radiation by gas molecules is a more significant mechanism. These molecules in the air absorb the emitted radiation at particular wavelengths and lead to form atmospheric transmission windows, which are relatively transparent for infrared radiation. Figure 1.2 shows the atmospheric transmission spectrum and the absorbing gases molecules for the infrared region.

As seen from the figure, H_2O and CO_2 are the dominant gases that lead to the absorption of IR for the infrared spectrum.
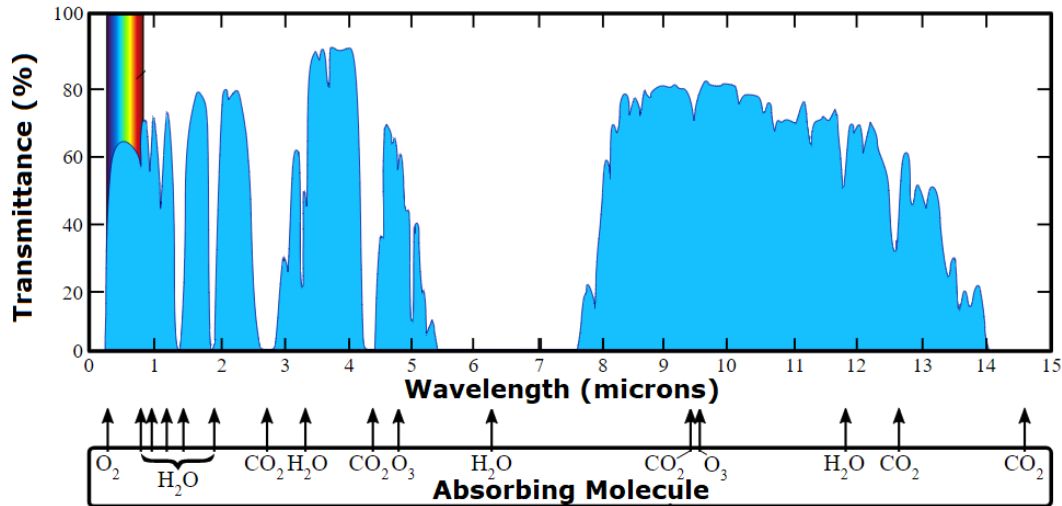
Figure 1.2: Atmospheric transmission spectrum and absorbing molecules for the infrared region [13].

The atmospheric transmission spectrum is subdivided due to the absorbing gas molecules with respect to transparency. These sub-bands are defined as follows:

- *0.7 – 1.4 μm, Near Infrared, (NIR):* This range begins from the end of the visible region and ends to the transmission is blocked due to the absorptions by H_2O molecules around 1.38 um. NIR region is mostly used for fiber optic telecommunications and imaging.

- *1.4 – 3.0 μm, Short-Wavelength Infrared, (SWIR):* Not only H_2O molecules but also CO_2 molecules affect the transmission in this region. This range is useful for systems that operate at night glow which is the natural light emerges. Moreover, SWIR provides better imaging than VIS for hazy and foggy weather.

- *3.0 – 5.0 μm, Mid-Wavelength Infrared, (MWIR):* This range is one of the most suitable with LWIR region for long-distance thermal imaging since the imaging is occurred by directly sensing the photons released from the object at close the room temperature. Also, the transparency of the atmosphere is relatively high for both MWIR and LWIR. If the exhaust gases and the hot

6

object such as engines or missiles are desired to detect, MWIR region is the better choice.

- *8.0 – 12.0 μm, Long-Wavelength Infrared, (LWIR):* This sub-band is the most appropriate range for thermal imaging since the peak emission wavelength of objects around at room temperature (300 K) corresponds in this range.

- *12.0 – 25.0 μm, Very Long-Wavelength, (VLWIR):* This band is used to image scenes colder than the room temperature, such as astronomical applications.

- *25.0 – 1000 μm, Far Infrared, (FIR):* The region has the lowest radiant power. It is used in Terahertz lasers or astronomical applications that very cold objects are imaged.

Each of the infrared sub-bands has its own advantages or disadvantages for usage areas. For SWIR region, the photon flux from objects at room temperature is too low, therefore, the imaging systems operating at SWIR need manmade, or natural light sources for illuminating the object desired to detect. Thus, the photon flux will be increased, and the object will be clearly imaged in environments such as at night glow. The biggest advantage of SWIR imaging systems is giving better images than visible systems for fogy and dusty weathers since SWIR has longer wavelengths, and that reduces Rayleigh scattering.
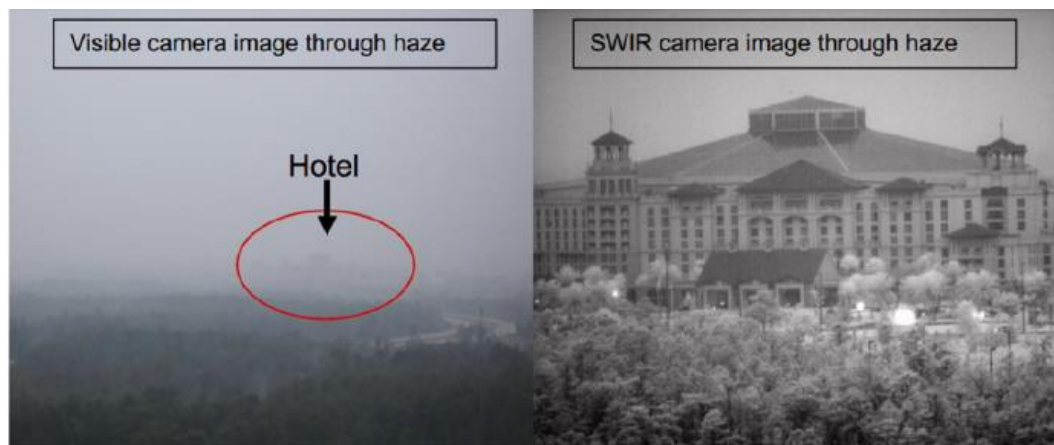
Figure 1.3: Images of the hazy environment taken by visible and SWIR cameras, respectively [14].

For MWIR systems, the thermal contrast allows to observe the temperature variation on the target scene more clearly, and it is two times greater than LWIR systems. Moreover, MWIR range gives better image quality for a scene with low scattering and for marine applications, where are higher humidity environments. However, MWIR imaging systems are heavily affected by radiation sources in battlefield environments since the emittance of the hot and room temperature objects extends to a large range for this sub-band. For LWIR imagers, environments with cold and low humidity are more suitable. Another advantage of this sub-band is lower sensitivity for scattering mechanisms than SWIR and MWIR since the scattering rate decreases with increasing the radiation wavelength. LWIR range is also more appropriate under battlefield conditions since the longer wavelength can penetrate the obscurants at the target scene more effectively.

Figure 1.4: Images taken by dual-band MW/LW SLS FPA fabricated on VISTA at 80 K [15].

Consequently, choosing the right infrared sub-band for detection depends on many variables such as the atmospheric conditions, which are humidity, climate, gas content, and weather or the background of the target to detect, or the temperature of the objects. In recent years, dual-band imagers, a combination of two sub-bands and dual-color imaging systems, defined as splitting the sub-band into two windows, have been produced to enhance infrared imaging systems. Thus, the deficiencies of different infrared regions can be minimized during the detection.

1.3 Types of Infrared Detectors

Infrared detectors can be classified into two main groups concerning operation principles: thermal detectors and photon detectors.

1.3.1 Thermal Detectors

The emitted radiation from an object causes a change in the physical properties of the detector's active material, such as conductivity, polarization, transmission, and dimension. The detection occurs by converting this change to electrical signals via electronic circuitry. Thermal detectors are not spectrally selective, which means they can absorb radiant power from all wavelengths of the electromagnetic region, but their operation region is limited by optics [16]. Thermal detectors have low sensitivity and slow response time since they need time for altering their physical properties due to heating. They do not require cryogenic cooling as they usually operate at room temperature, making them low cost. However, isolation is essential for thermal detectors not to be affected by ambient temperature fluctuations.

Consequently, thermal detectors are mostly preferred for low-cost and low-performance usage areas such as civilian applications. Thermocouples, thermopiles, bolometers, pyroelectric, and pneumatic detectors are the most well-known thermal detectors. Last but not least, the bolometers are the best performing thermal detector among them.

1.3.2 Photon Detectors

In photon detectors, absorption of the incident radiation occurs by interacting the incoming photons with the electrons in the active material of the detector. Thus, the electrons are excited from the lower energy state to the higher energy state, leading to the generation of electron-hole pairs (EHPs), known as free carriers. Then, these free carriers are collected at the contacts by an electric field, externally applied or

internally built, and the photogenerated current emerges. So, the emitted radiation from the object is converted to electrical signals, and detection occurs by photon detectors. The photons of the incoming radiation have low energy. Therefore, the photo-excitation can be suppressed by thermal excitation. In order to prevent that, the photon detectors are cooled to cryogenic temperatures. Even though cooling systems increase the cost of the photon detectors, the wavelength selectivity, which is a desired feature for dual-band operations, high signal-to-noise ratio, and a short response time are just some of the many advantages of photon detectors. They are used in military and medical applications mainly.

Photon detectors can be divided into two groups concerning the generation of the electric field: photoconductive and photovoltaic detectors.

Photoconductive Detectors: The photogenerated EHPs by absorbing infrared radiation are collected at contact regions with the help of externally applied bias to prevent any recombination process. The total flowing current through the detector increases thanks to the photocurrent, which is generated by the absorption since the conductivity of the detector increases. This current can be seen as a voltage across the load resistance R_L in Figure 1.5.
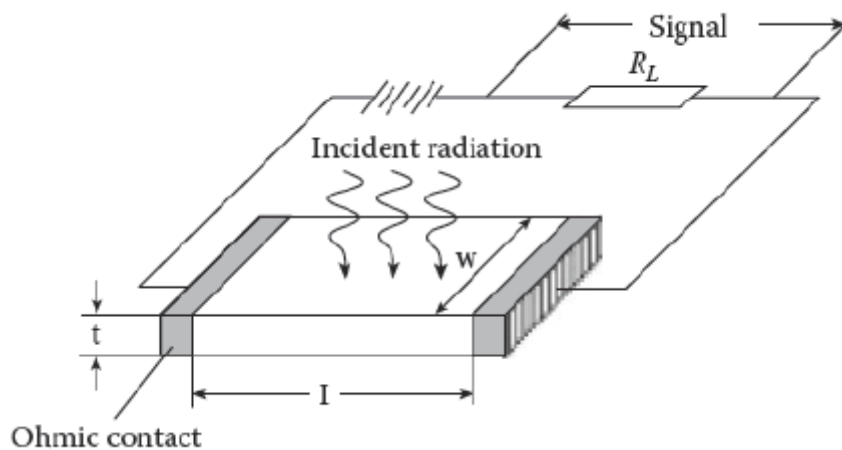
Figure 1.5: The operation of the photoconductive detectors [17].

The generated photocurrent I_{photo} is calculated as follow:

$$I_{photo} = q\eta w l \phi_s g_{photo} \qquad (1.8)$$

where q is the charge of the electron, η is the quantum efficiency, w is the width and l is the length of the photoconductor, ϕ_s is the incident photon flux density, and g_{photo} is the photoconductive gain, determined by the material properties of the detector. The gain of photoconductive detectors can be defined as the ratio of the free carriers which are collected by the circuit to the photogenerated free carriers in the detector. If the gain g_{photo} is greater than unity, many photogenerated carriers have reached the contacts before the recombination. On the other hand, when the photogenerated carriers have recombined before reaching the contacts, g_{photo} will be smaller than unity. Therefore, the large bias levels should be applied to generate photocurrent in photoconductor, but this causes an increase in power consumption for each pixel on the detector, which is undesired for large-format FPAs.

Photovoltaic Detectors: In photovoltaic detectors, the photoexcited EHPs are collected at the contacts via an internal built-in electric field created in a p-n junction. The structure and the operation principle of p-n junction as photon detectors can be seen in Figure 1.6. When p-type and n-type semiconductors have formed a p-n junction, which can be homojunction or heterojunction to whether p-type and n-type semiconductors are the same material or not, the majority hole carriers in the p-type semiconductor and the majority electron carriers in the n-type semiconductor constitute a depletion region around the junction. Thus, a built-in electric field is created in the junction. The photogenerated free carriers within the diffusion lengths and depletion region diffuse and sweep to the opposite side through the junction, respectively, due to the built-in electric field. Then, these carriers, which are not exposed to recombination, generate photocurrent and contribute to the reverse current (dark current), which is the thermally generated current of the junction.

As understood, photovoltaic detectors such as p-n, p-i-n, or heterostructure diodes can operate with low-level reverse bias, which causes low power consumption to

collect photogenerated carriers, unlike photoconductive detectors. That is the main reason why photovoltaic detectors are more preferred than photoconductive detectors.

W: depletion region width L_n, L_p: minority carrier diffusion lengths
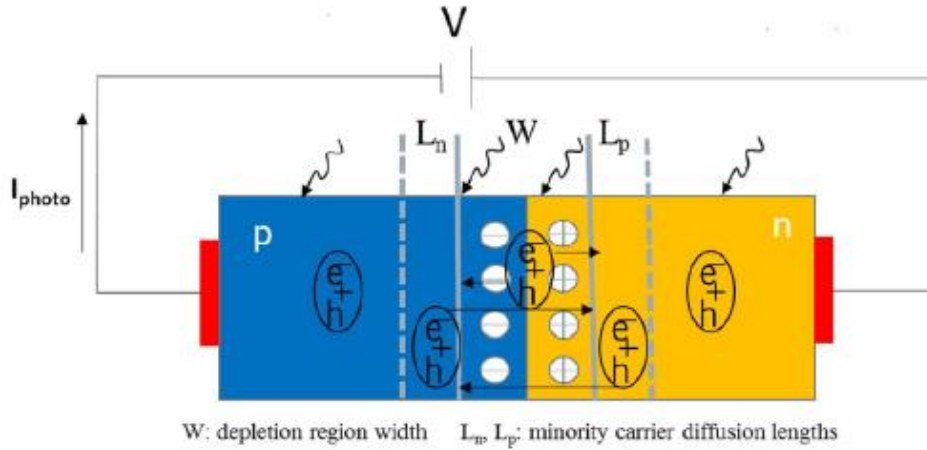
Figure 1.6: The structure and the operation of a p-n junction as a photovoltaic detector [18].

The photocurrent in photovoltaic detectors is expressed as

$$I_{photo} = q\eta A\phi_s \qquad (1.9)$$

where q is the electron charge, η is the quantum efficiency, A is the area of the photodiode, and ϕ_s is the incident photon flux density. The dark current of the photodiode has to be as low as possible from the photogenerated current for high-performance detection. The I-V curve of the photodiode can be seen in Figure 1.7.

The diffusion current is the only source of the dark current in an ideal photodiode, and it is proportional to the temperature of the photodiode. Therefore, photodiodes are cooled to suppress dark current. However, since photodetectors are not an ideal photodiode, there are different dark current mechanisms, which will be explained in Section 1.4.
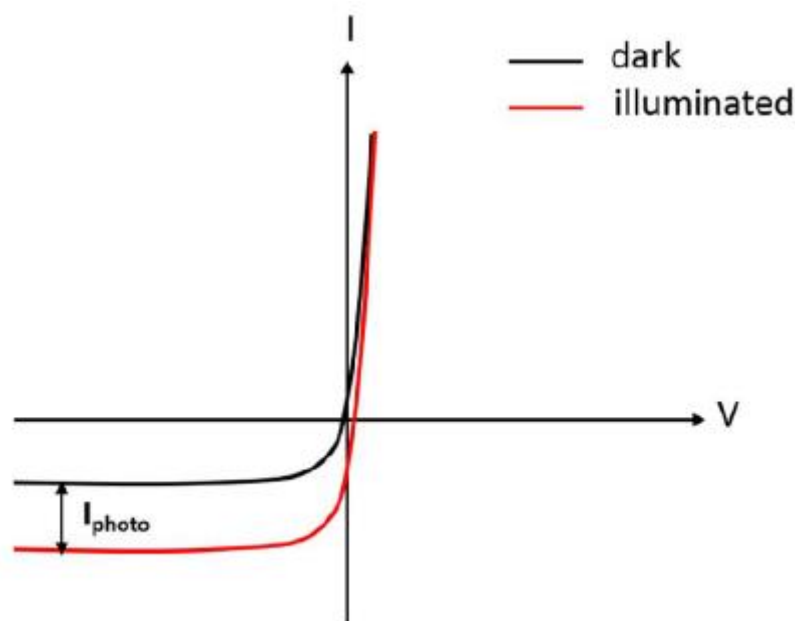
Figure 1.7: The I-V curve of the photovoltaic diode.

Photon detectors are also classified with respect to the interaction mechanism of the electrons and the holes with the absorption: the most important ones are the intrinsic, the extrinsic, and the band-gap engineering detectors.

Intrinsic detectors: The minority electron carriers excite from the valence band to the conduction band of the detector when the power of the incident radiation is equal to the band-gap energy or greater than the band-gap energy of the photodetector, as represented in Figure 1.8. Thus, the photocurrent is generated by minority EHPs. Although there are many semiconductor alloys such as InSb, InAs, HgCdTe, and InGaAs for intrinsic detectors, the most preferred ones are InSb and $Hg_xCd_{1-x}Te$. InSb is the binary material with fixed band-gap energy, corresponding to 5.5 µm cut-off wavelength. That means InSb detectors can only be used in the MWIR range, and dual-band or dual-color detection can not be done with InSb detectors. On the other hand, the band-gap of the ternary alloy $Hg_xCd_{1-x}Te$ can be tuned from SWIR to LWIR range by changing the composition of Hg. Besides the wavelength tuning possibility, its high quantum efficiency has made MCT detectors the most preferred detector where high performance is desired. However, several problems for MCT

13

such as high production cost, lattice mismatch, nonuniformity for especially LWIR range have led to search alternative detector materials.
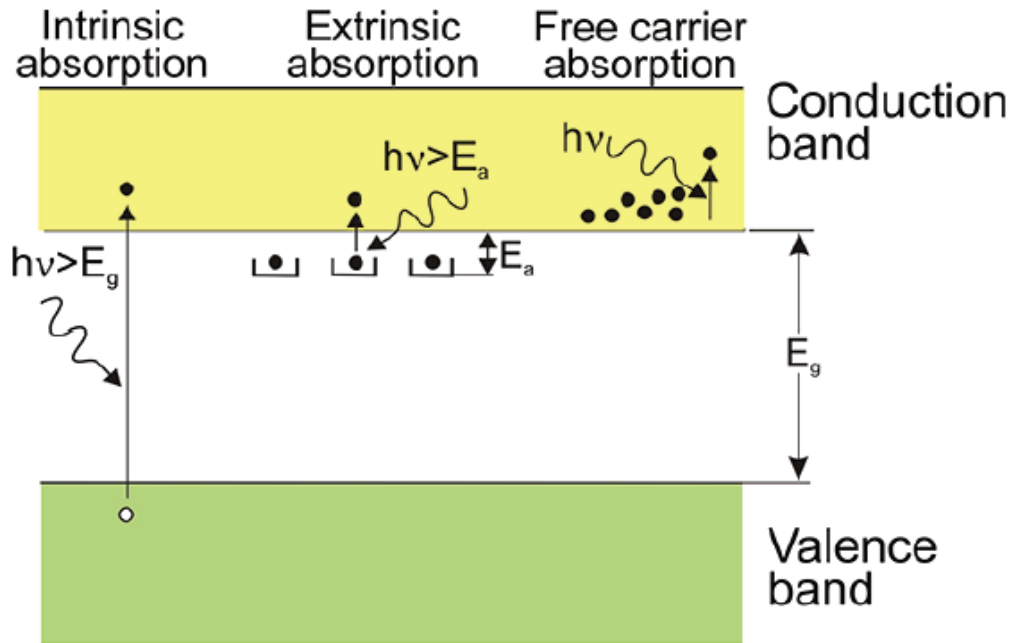
Figure 1.8: The photo-excitation processes for intrinsic, extrinsic, and free carrier absorption in semiconductors [19].

Extrinsic detectors: The extrinsic detectors are fabricated by intentionally doping with impurities to a large band-gap semiconductor to create new energy levels close to the conduction band of the semiconductor. The photogenerated free electrons excite from the impurity levels to the conduction band during absorption, as shown in Figure 1.8, and the detection occurs. Therefore, the cut-off wavelength of the detector is determined by the activation energy of the impurities. Si and Ge doped with III or V impurities are commonly used extrinsic detectors. The cooling process of extrinsic detectors is more significant than the intrinsic detectors for the same cut-off wavelength. However, they are favorable for VLWIR range, which has a quite low background flux conditions like astronomical applications.

The band-gap engineering detectors: Although the intrinsic photon detectors are the most preferred for infrared detection, the fact that InSb based detectors can only

operate in MWIR band or growth and fabrication difficulties of MCT based detectors, led the researchers to search for alternatives. As a result of these researches, a detector structure with artificial energy states for excitation called superlattice was discovered. Type-I, mostly known as QWIP, and Type-II Strain Layer Superlattice detectors are the best promising designs of superlattice structure.
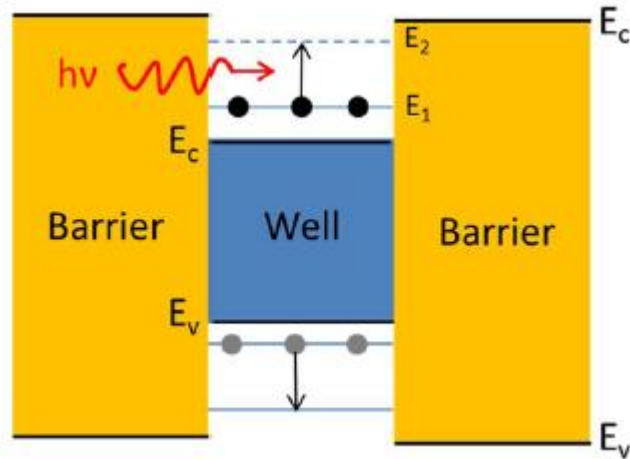
Figure 1.9: The illustration of QWIP and the optical transition
between sub-bands [18].

In QWIPs, a narrow band-gap semiconductor is sandwiched between large band-gap semiconductors to form a quantum well. Thus, the subbands localized in specific energy states inside the quantum well are created as in Figure 1.9. The carriers on these subbands can be excited to the higher subbands and then tunnel along to the continuum states, or they can also be transmitted directly from the subbands to the continuum states by absorption. The photoexcited carriers are collected at the contacts due to external bias and increase the current flow through the detector, as illustrated in Figure 1.10. The operation wavelength of QWIPs is specified by the energy difference between the first two localized energy states, and it can be tuned by changing the dimensional or compositional parameters of the barrier and quantum well. Thus, the operational wavelength becomes adjustable at QWIPs.
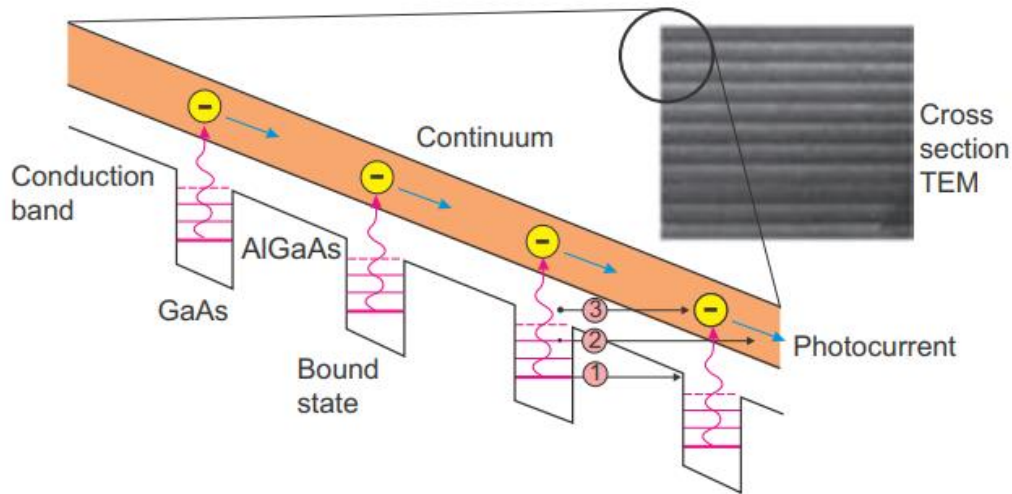
Figure 1.10: The conduction band diagram of AlGaAs/GaAs QWIPs under bias and TEM image of the design [20].

Even though QWIPs have many advantages, such as low-cost production with high uniformity, high yield, and stability, tunable operational wavelength, dual-band or dual-color detection, the low quantum efficiency of QWIPs prevents them from being a substantial alternative to MCT.

The Type-II Strain Layer Superlattice detectors are the most competitive detectors for MCT thanks to their promising features such as high quantum efficiency, adjustable operational wavelength, or lower dark current level, etc. In T2SLs, two different semiconductors in broken band alignment are grown periodically to create an artificial band-gap between the electron minibands and the hole minibands, as shown in Figure 1.11. The photon energy that needs for photo-excitation corresponds to the difference between these minibands. More details about T2SL will be given in Chapter 2.
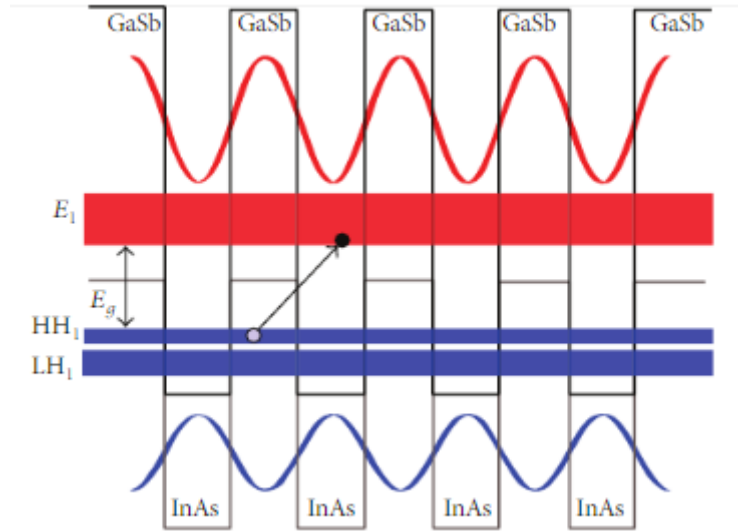
Figure 1.11: The band alignment of Type-II InAs/GaSb system [21].

1.4 The Figure of Merits for Photon Detectors

The performance evaluations of infrared detectors are made by comparing the figure of merits. These parameters are given below.

Quantum Efficiency (QE): Quantum efficiency is defined as the percentage of the photons on the detector that cause photo-excitation by generating the electron-hole pairs (EHPs). It is equal to 1 for the detectors in an ideal case. However, QE is less than 1 in real terms since there are many mechanisms to affect the generation of EHPs, such as reflection or lower absorption due to fabrication problems.

Responsivity (R): Responsivity is the ratio of the output signal to the input signal of the detector. The input signal is the incident radiant power in Watts, and the output signal can be either voltage or current. Therefore, the responsivity can be defined as the produced electrical signal in return for unit radiation power absorbed by the detector. It is given as:

$$R = \frac{Signal\ Output}{Incident\ Radiant\ Power} \qquad (1.10)$$

17

The incident radiant power P is expressed as:

$$P = E \times A_d \qquad (1.11)$$

where E is the irradiance or incident photon flux density on the detector area in $Watt/cm^2$, A_d is the area of the detector in cm^2. The unit of responsivity is either A/W or V/W. There is a relation between detector responsivity and the operational wavelength of the detector, which is known as spectral responsivity. It is identified with the wavelength range (spectrum) and the peak responsivity value. On the other hand, the responsivity can also be characterized for spectral radiant exitance of a blackbody, called blackbody responsivity. All incident radiation is considered to be absorbed by the detector for blackbody responsivity. The blackbody responsivity value must be specified with the blackbody temperature since the spectral blackbody exitance is changed with the temperature. The responsivity can be presented in terms of QE,

$$R = q\eta g \frac{\lambda}{hc} \qquad (1.12)$$

where q is the electron charge, η is the external quantum efficiency, g is the photoconductive gain which is the material-dependent value for the photoconductive detectors, and equal to 1 for photovoltaic detectors, λ is the wavelength of the radiation, h is the Planck constant, and c is the speed of the light.

Noise: The electrical noise can be identified as the undesired signals, which create fluctuations in the measured signal at the detector output. It is impossible to eliminate the noise completely. Therefore, the best option is to suppress the noise as low as possible for getting a high signal-to-noise ratio (SNR). Some of the main noise mechanisms in photon detectors are Johnson noise, shot noise, and 1/f noise.

The Johnson noise is also known as thermal noise since it is generated by the motion of the charge carriers at a temperature above absolute (0 K). It is formalized as:

$$i_n = \sqrt{\frac{4k_B T \Delta f}{R_0}} \qquad (1.13)$$

where k_B is the Boltzmann constant, T is the temperature in K, Δf is the measurement bandwidth, and R_0 is the differential resistance at zero bias.

The shot noise emerges due to the discreteness of electron charges. The random generation and flowing behaviors of electron charges lead to fluctuations in the output signal. The shot noise is given as:

$$i_{sn}^2 = 2qI_d \Delta f \qquad (1.14)$$

where q is the electron charge, I_d is the total dark current, and Δf is the measurement bandwidth.

The 1/f noise, also called pink or flicker noise, is inversely proportional to frequency. It has not a standard formula yet due to its complexity. For T2SL detectors, the frequently-dependent noise was observed because of the sidewall leakage current [22].

Noise Equivalent Power (NEP): Noise is the detrimental signal that emerges at the detector output and causes performance degradation. Since signal-to-noise ratio (SNR) increases with the radiant input power, it can not be used to measure the detector performance. The NEP is defined as the incident power, corresponding to acquire SNR, which is equal to 1 at the detector output. NEP is found as:

$$NEP = \frac{i_{noise}}{R} \qquad (1.15)$$

where i_{noise} is the detector's noise in amperes, R is the responsivity of the detector.

Detectivity: Detectivity is the inverse of NEP, and they are both critical parameters to evaluate the detector performance. However, they can be affected by the detector's active area and the measurement bandwidth. Therefore, the detectivity had

normalized to the detector's active area and the measurement bandwidth. This normalized detectivity is referred to as the specific detectivity ($D*$), and it is presented as:

$$D*= \frac{R\sqrt{A_d \Delta f}}{i_{noise}} \qquad (1.16)$$

where R is the responsivity, A_d is the active area of the detector, Δf is the signal bandwidth, and i_{noise} is the noise of the detector in amperes. The unit of specific detectivity is $cm\sqrt{Hz}/W$ and it is called Jones.

Noise Equivalent Temperature Difference (NETD): NETD is used to compare the performance of FPAs, and it is defined as the minimum detectable temperature difference between the object and its background, which is equal to the noise at the detector output.

Dark Current: Dark current mechanisms occur in the surface, bulk, or depletion region of a photodetector. The dominance of each mechanism changes with the temperature and the applied voltage. The dominant dark current mechanism of the detectors with respect to the temperature and the applied bias can be found by fitting the calculated current level to the measured current level. Therefore, the undesired dark current mechanisms can be suppressed by improving the growth conditions, fabrication process, and structural design [23]. Dark current mechanisms in photon detectors are diffusion, generation-recombination, band-to-bant tunneling, trap-assisted tunneling, and shunt current, as seen in Equation 1.17.

$$I_{total} = I_{diff} + I_{G-R} + I_{BTB} + I_{TAT} + I_{shunt} \qquad (1.17)$$

The diffusion current is originated by the thermally generated minority carriers, state near the depletion region of the junction. The minority carriers, which are at a distance of at least a diffusion length to the depletion region, flow through the depletion region to provide charge neutrality on the junction. It is dominated at high

temperatures and under small reverse biases. The formula of the diffusion current density can be expressed as [24]:

$$J_{diff} = n_i^2 \sqrt{q k_B T} \left(\frac{1}{N_D} \sqrt{\frac{\mu_h}{\tau_h}} + \frac{1}{N_A} \sqrt{\frac{\mu_e}{\tau_e}} \right) \left(e^{\frac{qV}{k_B T}} - 1 \right) \qquad (1.18)$$

where n_i is the intrinsic carrier concentration, q is the electron charge, k_B is the Boltzmann constant, T is the temperature in Kelvin, N_D is the n-type and N_A is the p-type doping concentration, respectively, μ_h and μ_e is the mobility of holes and electrons, respectively, τ_h and τ_e is the lifetime of holes and electrons, respectively, and V is the bias voltage. Since the diffusion current is increased with temperature, it can be reduced by cooling.

There are three generation-recombination (G-R) mechanisms in photon detectors, two of them are intrinsic, and one of them is extrinsic. When a relaxation of an electron from the conduction band to an empty state in the valance band takes place, the band-to-band recombination occurs, and it is an intrinsic mechanism. Another intrinsic mechanism is the Auger recombination. It occurs when an electron recombines with a hole. The energy coming from this recombination is taken by another conduction electron in order to excite to a higher energy state. The last G-R mechanism is known as Shockley-Read-Hall (SRH). It is an only extrinsic mechanism and is caused by defects in the depletion region of the junction. The electrons in these defects are thermally excited to the conduction band and increase the dark current of the detector. The SRH-based dark current density under the reverse bias is given as:

$$J_{gr} = \frac{q n_i w}{\tau_{gr}} \frac{2 k_B T}{q(V_{bi} - V)} \sinh \left(-\frac{qV}{2 k_B T} \right) f(b) \qquad (1.19)$$

where q is the electron charge, n_i is the intrinsic carrier concentration, w is the depletion width, τ_{gr} is the carrier generation-recombination lifetime in the depletion region, V_{bi} is the built-in voltage detector, V is the applied voltage, k_B is the

Boltzmann constant, T is the temperature in Kelvin, $f(b) = \int_0^\infty 1/(x^2 + 2bx + 1)\, dx$, and $b = \exp(-qV/k_BT)$.

The generation-recombination-based dark current is more dominant than the diffusion mechanism at low temperature since the effect of the diffusion current is reduced faster with cooling. Moreover, in order to suppress the G-R current, the detectors with a unipolar barrier are demonstrated. A barrier with a wider band-gap is placed to the depletion region of detectors. Thus, the G-R dark current is reduced by suppressing the SRH. For this aim, different designs with the barrier such as nBn, XBn, CBIRD are presented, and they will be presented in Chapter 2.

The band-to-band tunneling is observed when the large reverse bias is applied to the detector. The conduction band of the detector is aligned with the valence band, and the carriers in the valence band are excited to the conduction band by tunneling. The band-to-band tunneling current density can be given as:

$$J_{btb} = \frac{q^3 E(V) V}{h^2} \sqrt{\frac{2m_T}{E_g}} \exp\left(\frac{8\pi\sqrt{2m_T E_g^3}}{3qhE(V)}\right) \tag{1.20}$$

where q is the electron charge, $E(V)$ is the electric field, V is the applied voltage, h is the Planck constant, m_T is the tunneling effective mass, and E_g is the band-gap.

The charge carriers in the valence band of the detector are thermally excited to the trap state. Then, they make tunneling to the conduction band by biasing, and the trap-assisted tunneling current is generated. The current density of trap-assisted tunneling is expressed as:

$$J_{tat} = \frac{\pi^2 q^2 m_T M^2 N_T V}{h^3 (E_g - E_T)} \exp\left(\frac{8\pi\sqrt{2m_T(E_g - E_T)^3}}{3qhE(V)}\right) \tag{1.21}$$

where q is the electron charge, m_T is the tunneling effective mass, M^2 is the matrix element associated with the trap potential, N_T is the activated trap density, V is the bias voltage, h is the Planck constant, E_g is the band-gap, E_T is the trap energy location below the effective conduction band edge, and $E(V)$ is the electric field.

The tunneling-based dark current is decreased in type-II superlattice detector thanks to the larger effective electron mass. The details will be given in Chapter 2.

The shunt current is generated due to both the dislocations which form during epitaxial growth and the inadequate passivation process, which is made to prevent bonding between the free carriers and the dangling bonds that form due to the etching process in order to create mesa structures to get contact from the detector. The formula of this mechanism is calculated as:

$$J_{shunt} = \frac{V}{R_{shunt}A} \tag{1.22}$$

where V is the bias voltage, R_{shunt} is the detector shunt resistance, and A is the junction area. Recently, the shunt current mechanism has been greatly reduced with the passivation methods for T2SL detectors.

1.5   Motivation and Thesis Organization

The interest in the type-II superlattice detector is increasing day by day. The different structure designs have been proposed to enhance the performance of superlattice detectors to the level of MCT-based infrared detectors. Therefore, the suppression of the dark current mechanisms is crucial for detection. The nBn and the N-structure designs are promising structures separately to reduce the dark current, as seen recently. For this aim, a new structure with the combination of nBn and N-structure is designed. The motivation of this thesis work is to fabricate this new design and investigate the performance by measuring the performance parameters.

The organization of the thesis is presented as:

In Chapter II, the history and the developments of type-II superlattice detectors are proposed. The advantages of T2SL over the other detector type are mentioned. Then, the different structures and their improvements are defined to emphasize the advantages of barriers and supercells.

In Chapter III, the fabrication steps of the test detectors are explained. The different sizes of pixels are patterned on the new design. The etching optimization is completed by trying the different etching depths. Then, the samples are packaged on 84 pin LCC to be ready for measuring.

In Chapter IV, the electrical and the optical characterizations were done by measuring temperature-dependent dark current density and blackbody responsivity and calculating the performance parameters of the processed samples.

In Chapter V, the thesis study is summarized. The obtained results and the improvements to be done for characterization of the structure were discussed for future work.

CHAPTER 2

TYPE-II SUPERLATTICE DETECTORS

The advances in infrared imaging have increased rapidly by realizing the importance of infrared imaging in several areas such as military, medical diagnostics, space applications. The market was dominated mainly by MCT, InSb, InGaAs detectors until the middle of the 1980s. A new material called superlattice was revealed by Tsu and Esaki in the 1970s [7], and they put a crucial milestone for detector technology. Then, QWIP emerged as an alternative to these former detector technologies as a continuation of Tsu and Esaki's study. Even though these detector technologies have excellent futures for IR imaging, they have their own disadvantages, such as the MWIR range limited detection for InSb ones, the low production yield, and the high fabrication cost of MCT detectors, the SWIR range limited imaging of InGaAs detectors and low quantum efficiency of QWIP. Therefore, a Type-II superlattice detector has been revealed as a promising alternative that has all deficiencies of former detector technologies.

The T2SL based photodetectors can be grown and fabricated with high yield, high uniformity, and low cost via the mature III-V growth technology. The effective band-gap of T2SL can be varied from 0.4 eV to below 0.1 eV by adjusting the thickness of the constituent layers [25]. Thus, the operational wavelength of T2SL detectors can be tuned from SWIR to VLWIR range, or multi-band imaging can be obtained. Moreover, the performance of T2SL detectors improves at higher temperature since a large effective electron mass causes a longer Auger recombination rate [26] and suppress the tunneling effect. The high quantum efficiency can be achieved at the level of MCTs since the photon absorption through the normal direction is allowed in T2SLs.

In this chapter, the history of T2SL detectors will be represented as a beginning. The following three sections explain the general information about superlattice band alignment, 6.1 A° Family, and the T2SL structures. State of the art about T2SL detectors is discussed in section five. The performance parameters of T2SL detectors are given in the last section of the chapter.

2.1   Historical Perspective of T2SL Detectors

The interest in IR imaging systems has moved to superlattice structure because of the superior advantages, which emerged with the study by Esaki et al. in the 1970s [7]. After that, in 1977, the idea of type-II superlattice was proposed as a new type of bilayer semiconductor by Sai-Halasz et al. [27]. The theoretically analyzed type-II superlattice structure can be defined as the lower conduction band (CB) edge is located in one material while the higher valence band (VB) edge is located in another material. Thus, the localization of the electron wavefunctions is formed in the lowest conduction band of one semiconductor, and the localization of the hole wavefunctions is formed at the highest valence band of the other semiconductors, which can be seen in Figure 2.1. Therefore, the positions of the conduction band edge and the valence band edge can be tuned independently.
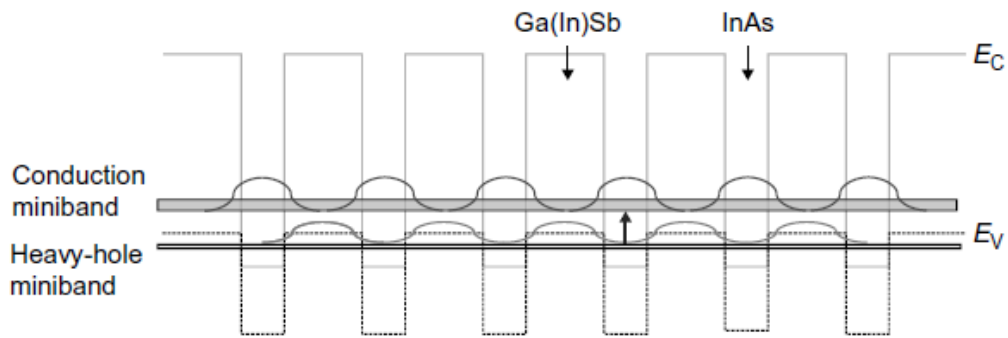
Figure 2.1: The illustration of the spatial separation of the conduction band and the heavy-hole valence band wavefunctions in an InAs/Ga(In)Sb type-II broken-gap (misaligned) superlattice [28].

It was also mentioned that the CB edge of InAs should be lower than the VB edge of GaSb by 0.14 eV, which can be led to interaction between these sub-bands. The essential future that creates type-II superlattice is known as broken-gap alignment between InAs and GaSb. It was noticed by W. Frensley during his Ph.D. thesis research under the supervisor of H. Kroemer [29] in 1977. In the same year, the broken-gap alignment between InAs and GaSb was theoretically calculated by Harrison using a combination of several methods [30]. Even though Harrison does not emphasize this extra-ordinary alignment, Frensley and Kroemer noticed it and, they pointed out the opportunity of interband tunneling between these subbands. Next year, Sai, Esaki, and Harrison proposed that the superlattice formed by thin InAs and GaSb layers can act as a semiconductor with a specific energy band-gap, whereas the superlattice with thick InAs/GaSb layers behaves like a semimetal. That means the band-gap of InAs/GaSb superlattice can be adjusted small or even smaller than InAs or GaSb individually [31]. The IBM Group has made experimental studies by using molecular beam epitaxy (MBE) to grow InAs/GaSb superlattice, which has theoretically calculated band-gap energy to demonstrate the decreasing of band-gap with increasing layer thickness. The band-gaps of the grown samples with these experiments, which have different layer thicknesses are varied from 265 to 360 meV at 10K [32]. Moreover, the superlattice structure with this new alignment is called type-II superlattice (staggered or broken-gap) to separate it from the type-I superlattice [31].

Schulman and Mcgill revealed the idea of using the CdTe-HgTe superlattice as an infrared detector in 1979 [33], and they indicated that InAs/GaSb superlattice should also have similar band-gap properties. However, the possibility of insufficient size of the optical matrix element due to the spatially separated hole and electron wave functions have worried them in the type-II superlattice. Then, Smith et al. reconsidered the CdTe-HgTe superlattice and discovered the advantages of the CdTe-HgTe superlattice over the MCT alloy, such as the lower band to band tunneling due to the shorter tunneling lengths for same band-gap, the independence of cut-off wavelength from the composition, decreased diffusion current of p-side

caused by the larger electron mass [34]. These futures are also acceptable for InAs/GaSb superlattices. Chang and Schulman discussed the possibility of the weak oscillator strength in T2SL in 1985 [35], and the optical properties of type-II superlattice have been calculated. They acquired that the oscillator strength of optical transition for InAs/GaSb is proportional with $1/MN$, where M and N determine the number of InAs and GaSb monolayers for each period, respectively, and reduces sharply with a layer thickness of InAs/GaSb. This phenomenon was clarified by Kroemer in 2004 [36]. The separately localized electron and hole wave functions in InAs and GaSb overlap in the nearest heterointerfaces. That means the optical transition is proportional to the number of interfaces rather than the layer thickness, and the optical transition does not occur in most parts of InAs/GaSb volume. For this reason, Smith and Mailhiot proposed the type-II InAs/GaInSb strain layer superlattice detector in 1987 [37].
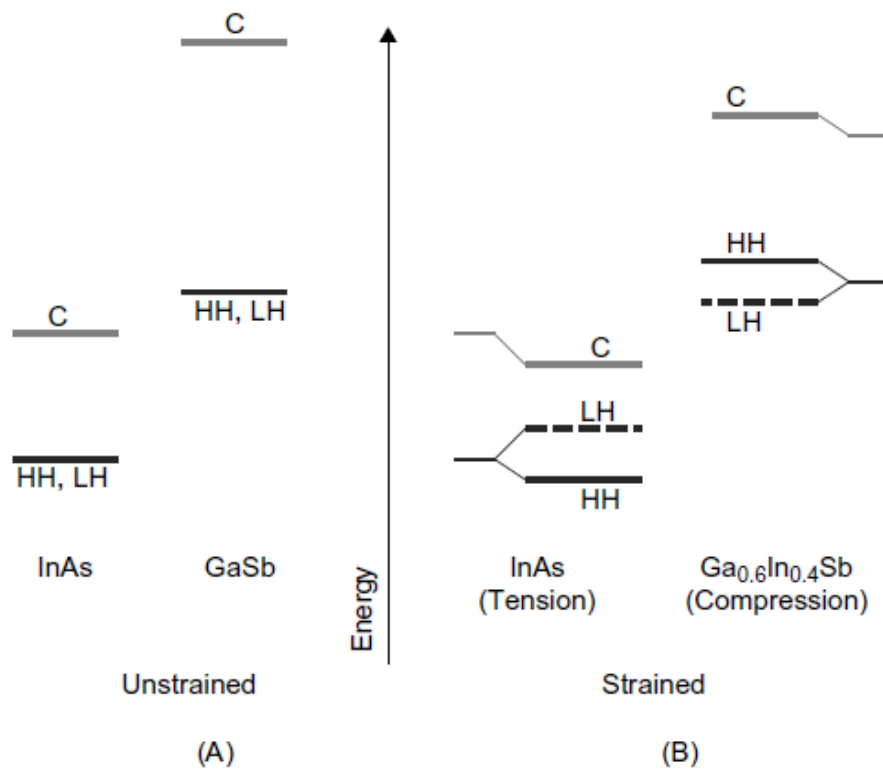
Figure 2.2: The schematic illustration of band edge energy positions for unstrained InAs and GaSb and strained InAs and $Ga_{0.6}In_{0.4}Sb$ [37].

They designed InAs/Ga$_{0.6}$In$_{0.4}$Sb by applying tensile and compressive strain to InAs and GaInSb, respectively. Thus, lower InAs CB edge and raised heavy-hole (HH) band edge of GaInSb, which lead to the deeper InAs CB quantum well and GaInSb HH quantum well, are obtained as shown in Figure 2.2. Therefore, the optically active volumes of InAs/GaInSb can be increased by forming narrower quantum wells without increasing the band-gap of the superlattice. They also indicated two crucial things: using the n on p diodes for infrared detection is feasible since the electron mobility is greater than the hole mobility, and GaSb is the most suitable substrate to grow InAs/GaInSb superlattice. In 1990, Miles et al. experimentally proved the absorption of InAS/GaInSb strain layer superlattices in LWIR [38]. In the following years, the theoretical analysis about Auger recombination rate of the superlattice with respect to the bulk semiconductors has been worked [39] [40]. The experimental study to measure Auger lifetime of InAs/GaInSb was revealed by Youngsdale et al. in 1994 [41]. Furthermore, the fundamental studies that improved the type-II superlattice as an infrared detector, such as the theoretical analysis of the electrical and the optical properties of the InAs/GaSb superlattice, were done [42] [43] [44] [45]. In 1998, the research group of Razeghi presented the results about InAs/GaSb superlattice [26]. They reported that InAs/GaSb superlattice has a significant absorption coefficient like InAs/GaInSb because of the higher joint density of states than bulk alloys, even though it has weaker oscillator strength. The lattice mismatch (0.6%) between InAs and GaSb leads to unstrained or minimally strained layers, unlike InAs/GaInSb, but InAs/GaSb superlattice has promised advantages over the strain layer InAs/GaInSb superlattice.

T2SL technology stepped into a new era between 1996 and 2005 with the development of the first generation antimonide-based superlattice detectors and FPAs with high performance. In particular, thanks to studies of Fuchs et al. in 1997 [46] and Johnson et al. in 1996 [47], high-performance InAs/GaInSb SLS photodiodes operate in the LWIR range are presented. Thus, antimonide-based superlattice detectors draw attention, leading to the generation of the first 256×256

29

FPA by Walther et al. in 2005 [48]. Besides these, essential progress in design, growth, fabrication, and characterization, which cause improvements in detector performance, were obtained [49] [50]. GaSb is the most suitable substrate for producing SL since it is almost lattice-matched with InAs/GaSb superlattice. However, commercially available GaSb substrates had some deficiencies such as poor surface morphology, high defect density, limited size, and high cost during these years. Therefore, GaAs substrate with better quality and easy to find in large sizes as an alternative to GaSb was studied by Bennett [51] and was shown experimentally with rewarding results by Brown [52].

The studies of type-II superlattice detectors rapidly increased after 2006 and mainly focused on two things: heterostructure designs to decrease the dark current, enhance quantum efficiency and improve fabrication processes to acquire higher uniformity and repeatability for large format FPA production. The heterojunction superlattice designs such as nBn [53], pBp [54], XBn [52], and also double heterojunction design superlattice [56] detectors were presented. The single-band T2SL nBn detectors [57], the dual-band T2SL nBn detectors [58], the SL pMp detector [59], and the SL pBn detector [60], the p-π-M-n SL detector [61], and the complementary barrier infrared detector (CBIRD) [62] structures have studied by researches. Moreover, complex supercells were used in heterojunction superlattice designs such as W [63], M [59], and N [64] structures. Detailed information about the popular structures will be given in Section 2.3.

The dark current density of bulk superlattice has been reduced by the heterostructure designs. However, the surface leakage currents of the mesa sidewalls become more distinguishable. Since surface leakage current affects from the etching process parameters, post-etch cleaning, and surface passivation, several studies about decreasing the surface leakage current have been published [65] [66]. In particular, the surface passivation methods have made a significant improvement in reducing the surface leakage current [67] [68] [69].

30

Although there have been many studies since the first SL proposal, the progress of SL detectors is summarized by presenting the milestones.

2.2 General Theory of InAs/GaSb SLS Type-II Superlattice

In this section, the binary compounds used in SL structures will be explained. Then, the superior properties of SL, which cause the best alternative of infrared detectors, will be presented one by one.

2.2.1 6.1 Aº Family

The binary compounds InAs (a=6.0584 Aº), GaSb (a=6.0959 Aº), and AlSb (a=6.1355 Aº) are named as 6.1 Aº material system by Kroemer in 2004 [36] since their lattice constants of them are almost equal to 6.1 Aº. The band-gap energies of them with respect to the lattice constant and the band alignments of 6.1 Aº materials can be seen in Figure 2.3.
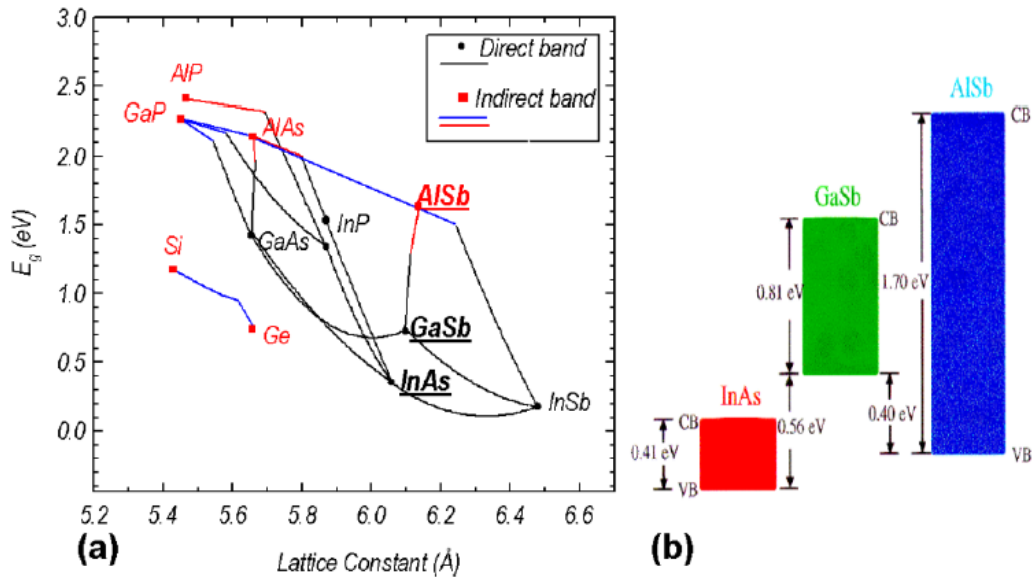
Figure 2.3: (a) The band-gap energies versus the lattice constant of 6.1 Aº family members. (b) InAs, GaSb, and AlSb band gap energies [70].

These semiconductors have crucial optical and electrical properties for infrared detection, such as high quantum efficiency thanks to the intense normal-incidence band-to-band absorption, which leads to a direct band-gap for GaSb in SWIR range, InAs in MWIR range, and InAs/GaSb superlattice in SWIR, the MWIR, and LWIR range. Additionally, the phonon scattering that emerged by the intersubband absorption mechanism is prevented with the valence-to-conduction band IR absorption mechanism with the direct band-gap of the 6.1 A° family. The impurities that occurred by the lattice mismatch, the other mechanism to cause the phonon scattering, is decreased by using InAs, GaSb, and AlSb semiconductors. Since the phonon scattering reduces the operating temperature of the detectors, InAs/GaSb superlattice detectors can operate at a higher temperature.

The band alignments of the 6.1 A° family members with respect to each other are known as The type-I (used in QWIP), type-II staggered, and type-II broken (or misaligned) alignments can be seen in Figure 2.4. Moreover, different structures called complex supercells can be produced by inserting AlSb in SL InAs/GaSb type-II superlattice with different positions.
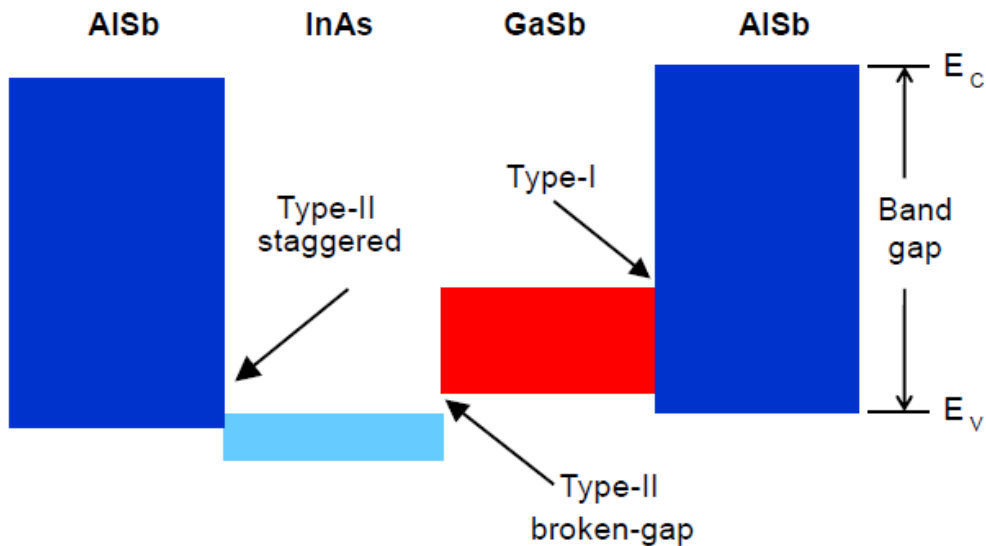
Figure 2.4: The energy band alignment of nearly lattice-matched InAs/GaSb/AlSb 6.1 A° family [71].

2.2.2   Tunneling Suppression

The tunneling property of the T2SL detector is controlled by the evanescent waves in the band-gap as in all photodiodes. Since the InAs layer is split as a heavy-hole (HH) band and a light-hole (LH) band due to the strain InAs layer to GaSb substrate, these evanescent waves cause tunneling leakage, is combined with the conduction band edge and the light-hole edge. Thus, the tunneling effect is suppressed on InAs/GaSb superlattice detectors. Moreover, the tunneling probability is higher on materials with lower effective mass. Unlike MCT detectors, the magnitude of the electron effective mass is related to the overlap between the electron wavefunction in neighbor InAs wells. That means the electron effective mass of T2SL is not dependent on the band-gap of the semiconductor, unlike MCT. The tunneling leakage on T2SL detectors is less than the bulk photodetector like MCT in the same bandgap energy due to the larger electron effective mass. In conclusion, the tunneling leakage is reduced by strain layer of InAs and higher electron effective mass on T2SL detectors.

2.2.3   Auger Recombination

Auger recombination can be expressed as the recombination of the electron and the hole in direct (or band-to-band) transition, which generated energy is transferred to another electron and hole with respect to the type of Auger recombination. Auger 1 and Auger 7 are the types of Auger recombination. In n-type material, the recombination of the majority electron in the conduction band with the minority hole in the valence band is known as Auger 1 recombination. The energy emerged by this recombination is transferred to another majority electron in the conduction band to be excited to a higher energy level. In p-type material, the recombination of the majority hole with the minority electron is known as Auger 7 recombination, and the released energy is transferred to a different majority hole to be excited deeper inside the valence band. However, since the valence band is split as the heavy hole and the

light hole due to the intentionally strained, the Auger 7 recombination is suppressed in the p-type material. That leads to decreasing the diffusion current, which is one of the dark current mechanisms in the photon detector. Hence, the superlattice detectors can be operated at high temperatures.

2.3   Type-II Superlattice Structures

With the increasing interest in superlattice detectors, different alternative structures were presented to develop the performance of type-II superlattice detectors by reducing the dark current. Since the dark current is decreased due to the larger electron effective mass and suppression of Auger recombination in T2SL detectors, alternative designs were presented to reduce other dark current mechanisms. In this section, the development of the T2SL structures and their abilities are presented.

2.3.1   p-i-n Structure

The p-i-n structure can be identified as the oldest type-II superlattice detector. In p-i-n T2SL, an intrinsic region is inserted in the standard p-n junction for absorption, as shown in Figure 2.5. The p-type region of InAs/GaSb T2SL is formed by doping GaSb layer with Be (Beryllium) atom, and the n-type region is acquired by doping InAs with Si (Silicon) or Ti (Titanium).
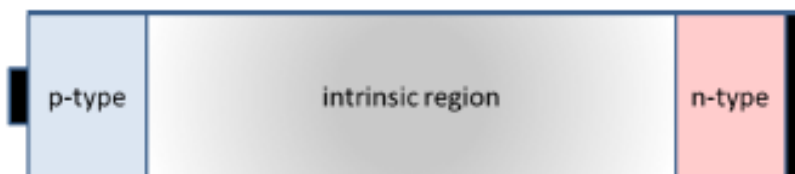
Figure 2.5: The schematic illustration of p-i-n T2SL.

2.3.2   M-Structure

The M-structure superlattice detector was proposed by Nguyen et al. in 2007 [72]. The AlSb layer is inserted in the middle of the GaSb layer at the InAs/GaSb type-II superlattice to use the AlSb layer with a high band-gap as a barrier for blocking the electron and the hole. Since the band alignments of AlSb-GaSb-InAs-GaSb-AlSb layers resemble the letter M, this new design is named as M-structure. The schematic diagram of it can be seen in Figure 2.6. In particular, this structure has shown a lower dark current by suppressing tunneling current for LWIR range.
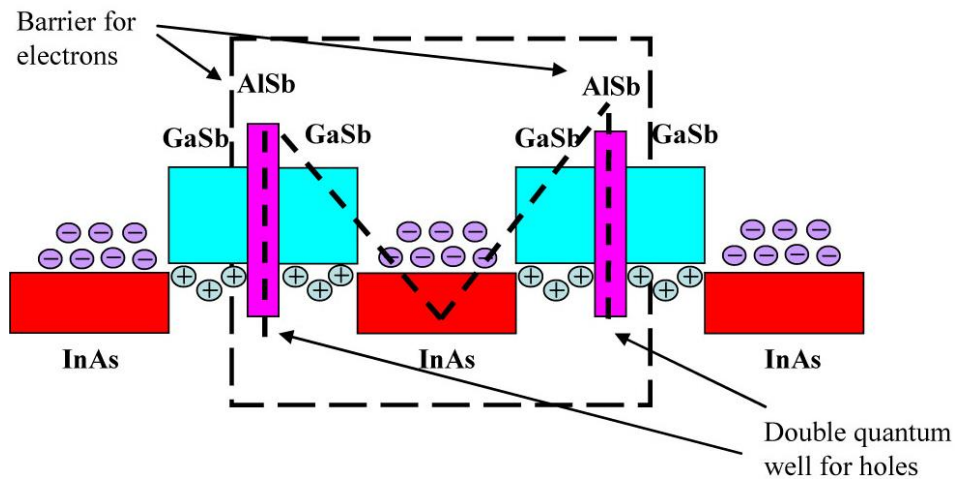
Figure 2.6: The schematic illustration of M-structure InAs/GaSb T2SL [72].

2.3.3   Complementary Barrier Infrared Detector (CBIRD)

CBIRD structure was proposed by Ting et al. in 2009 [62]. The illustration of the energy band diagram of CBIRD is shown in Figure 2.7. The lightly p-doped InAs/GaSb absorber is inserted between an n-doped InAs/AlSb hole barrier superlattice and InAs/GaSb electron barrier with a wider band-gap. The bottom contact layer of the structure is a heavily n-doped InAsSb. The electron and hole barriers have, respectively, almost zero conduction and valence band offset with respect to InAs/GaSb absorber since they behave as complementary unipolar

barriers. The hole barrier reduces the dark current with SRH-based. Moreover, trap-assisted tunneling is also reduced by the hole barrier with the wider gap. The electron barrier blocks the extra electron coming from the bottom contact.
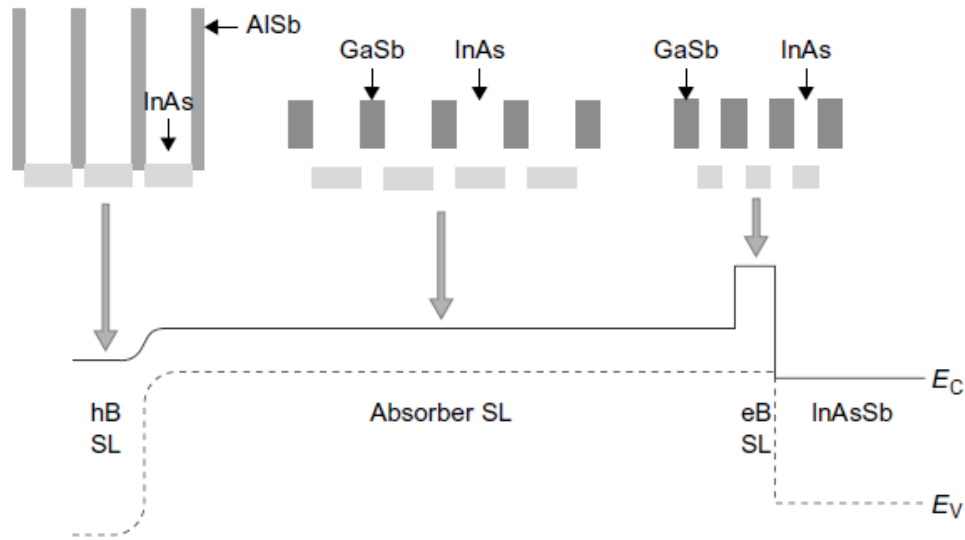
Figure 2.7: The schematic energy band diagram of CBIRD operates in LWIR [28].

2.3.4   N-Structure

Two thin monolayers AlSb have been placed asymmetrically between InAs and GaSb layer to act as an electron barrier, as seen in Figure 2.8 [64]. In the symmetrical case under the bias, the overlap between electron and hole wavefunction will be increased on one side of AlSb layer, whereas it will be decreased on the other side due to the direction of the electric field. When the asymmetrical barrier is inserted in the direction of bias, the enhancement of the absorption without any loss of overlap has achieved. Therefore, the dark current caused by the diffusion current has reduced with N-structure.
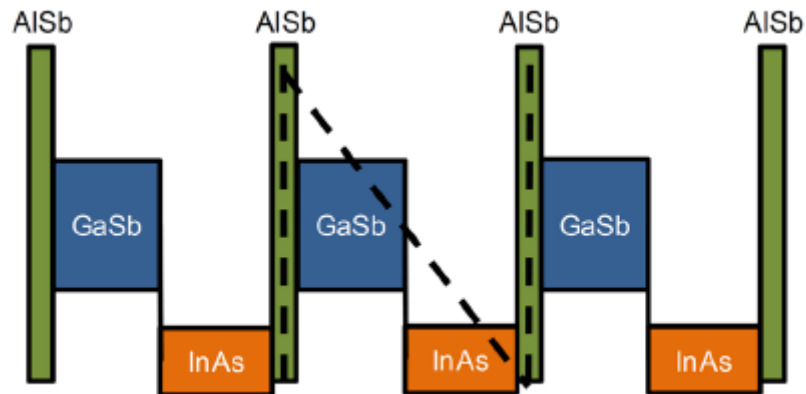
Figure 2.8: The schematic of the band alignments at N-structure T2SL [64].

2.3.5   nBn Structure

In nBn superlattice detectors, a large band-gap barrier layer is sandwiched between two n-type semiconductors that behave as absorbing layers. Hence, the majority electron carriers will be blocked by the barrier layer, whereas the minority hole carriers move between the contact layer [53]. This structure is also known as a unipolar barrier since the barrier layer blocks one carrier type (electron) and allows the other (hole).

The greatest advantage of the nBn structure is reducing the dark current, which is associated with Shockley-Read-Hall current thanks to the electron barrier layer. Decreasing SRH with nBn structure enables a higher operational temperature with respect to the p-i-n structure superlattice detector. In particular, the critical design parameter to suppress SRH and to produce a detector with a low, diffusion-limited dark current is to make the doping type of the barrier and the active layers the same [73]. Moreover, the surface leakage current is decreased significantly by the barrier layer since it behaves as a self- passivation layer.

Recently, bias selectable dual-band or dual-color nBn T2SLs were proposed [74] [75]. As shown in Figure 2.9, the operational wavelength can be changed by switching the polarity of the bias voltage.
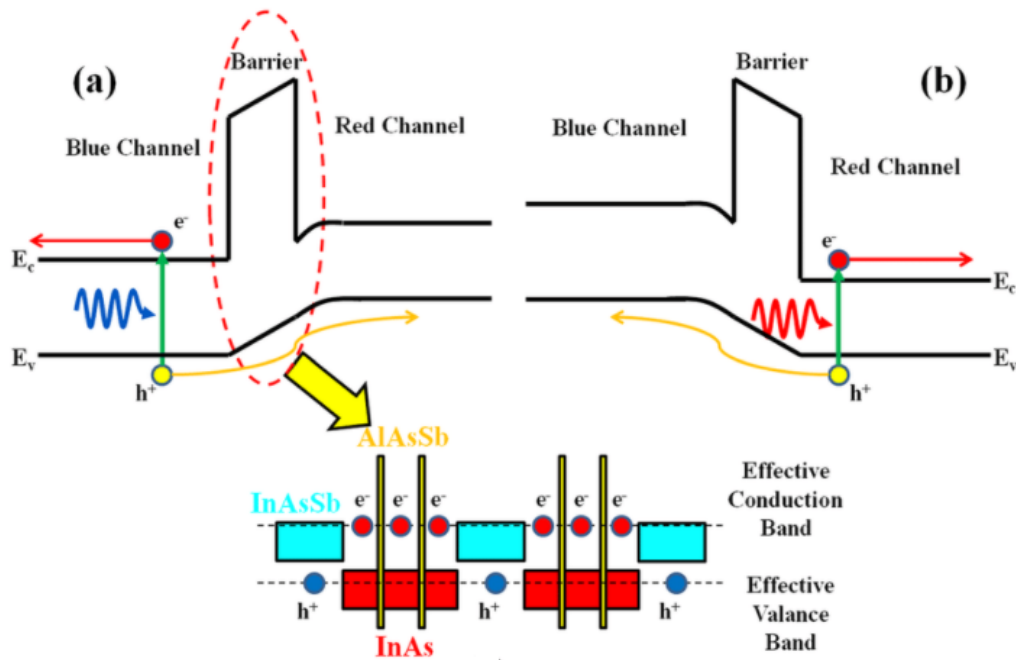
Figure 2.9: The band alignments of nBn T2SL with respect to the bias polarities [75].

Although there are many structure types for T2SL detectors, the major ones such as p-i-n, nBn, M-structure, N-structure, and CBIRD were presented here.

2.4   Recent Developments of T2SL Infrared Detectors FPA

The first superlattice FPA was proposed by Walther et al. in 2005 [48]. This IR camera has 40 µm pitch 256×256 MWIR FPA with 5.4 µm cut-off wavelength. The quantum efficiency of FPA is %30, and the detectivity values exceed 10^{13} Jones at 77 K in cut-off wavelength. The NETD of FPA was measured as 11.1 mK for 5 ms integration time with f/2 optics. The image taken by this FPA can be seen in Figure 2.10. In 2006, Razeghi et al. demonstrated 20 µm pitch 256×256 MWIR FPA with

bigger than 30% external quantum efficiency and 10^{11} Jones detectivity at 77 K in the 10 µm range. The peak NETD value of the FPA was around 0.2-0.3 K at 85 K.

Figure 2.10: The image was taken by the first superlattice 256×256 MWIR FPA by Walther et al. in 2005 [48].

The images were taken by this detector can be seen in Figure 2.11.
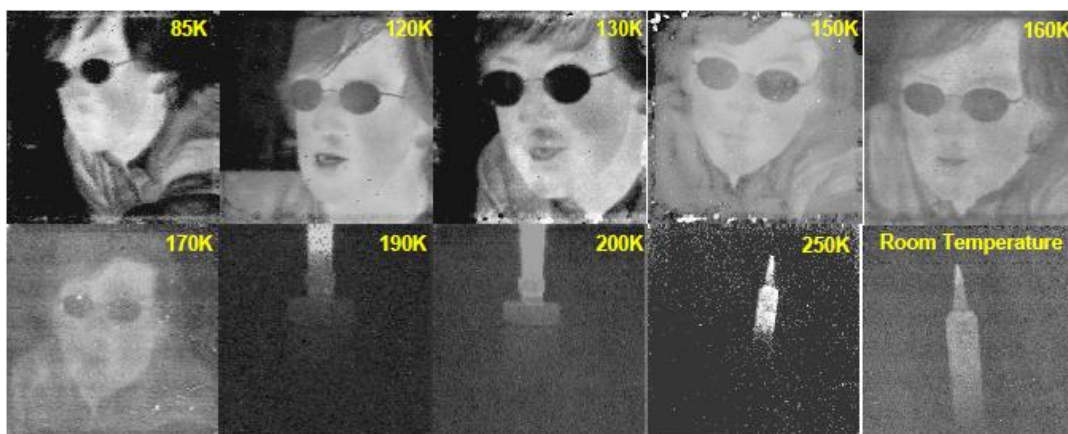
Figure 2.11: The IR images acquired with MWIR FPA with 5 µm cut-off wavelength at room temperature [76].

39

In the following year, Little et al. showed 320×256 MWIR FPA superlattice. The same year, Walther and his colleague demonstrated 24 µm pitch 288×384 single FPA and 40 µm pitch 288×384 dual-color FPA [77]. The single color FPA showed 27.9 mK NETD with 4.9 um cut-off wavelength, 1 ms integration time, and f/2.4 optics at 77 K, shown in the left side of Figure 2.12. Again in 2007, Center for Quantum Devices from NWU demonstrated a 25 µm pitch 320×256 FPA with a 12 µm cut-off wavelength which has 340 mK mean NETD, shown in the right side of Figure 2.12 [78].
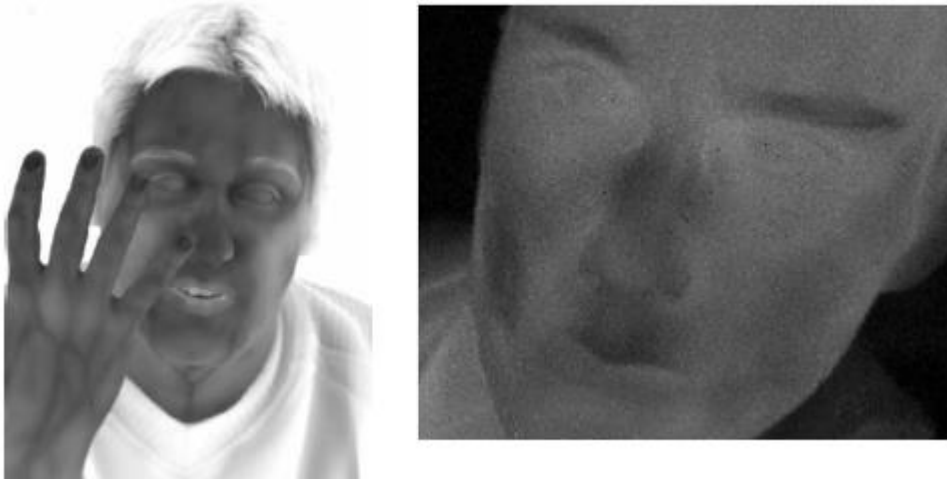
Figure 2.12: The thermal images were taken by Walther et al. single color FPA in the left [77] and by Center Quantum Device detector in the right [78].

The last FPA of 2007 was proposed by researchers from Raytheon Vision System and Jet Propulsion Laboratory. It was a p-i-n structure LWIR FPA superlattice with 30 um pitch with 256×256 arrays which has 10.5 µm cut-off wavelength. In 2008, 256×256 MWIR FPA with nBn T2SL detector was presented by Kim et al. [79]. The same year, Plis et al. revealed nBn based T2SL FPA with single-band and dual-band InAs/GaSb SLs [80]. The single-band FPA, which has 24 um pitch 320×256 array size, was shown 23.8 mK NETD value with 16.3 ms integration time and f/4 optics as seen in Figure 2.13.

Figure 2.13: Thermal image taken by 320×256 InAs/GaSb nBn based superlattice with 16.3 ms integration time at 77 K [80].

In 2009, dual-color 40 µm pitch 384×288 InAs/GaSb SL FPA was revealed by Rutz et al., and NETD values of the blue channel and the red channel are 25.9 mK and 14.3 mK, respectively, with 0.2 ms integration time as shown in Figure 2.14 [81]. In 2010, Sundaram et al. presented 320×256 LWIR FPA made from InAs/GaSb SLS detector [82].

Figure 2.14: The infrared image taken with 384×288 dual-color InAs/GaSb SL camera. The blue channel corresponds to between 3-4 µm and the red channel corresponds to between 4-5 µm are represented by cyan and red colors, respectively [81].

In 2011, Walther et al. presented dual-color 40 µm pitch MWIR T2SL FPA in 288×384 array size [83]. The blue channel, which operates between 3-4 µm, had 18 mK NETD and the red channel, which operates between 4-5 µm, had 10 mK NETD with 1.5 ms integration time and f/1.5 optics. The images taken with dual-color FPA can be seen in Figure 2.15.

Figure 2.15: Thermal images taken with dual-color FPA. The left is the blue channel, and the right is the red channel [83]. White regions correspond to the colder places.

In 2013, Razeghi et al. demonstrated MWIR/LWIR dual-band 256×320 T2SL FPA with 5 µm and 12 µm cut-off wavelengths at 77 K, shown in Figure 2.16 [84].

Figure 2.16: Thermal image taken with dual-band 256×320 T2SL FPA [84].

In the same year, M-Structure 15 µm pitch 640×512 array size T2SL FPA was presented by Martijn et al. [85]. The quantum efficiency of FPA is 65% without anti-reflection coating with 5 µm cut-off wavelength. The NETD value is 41 mK with 21 ms integration time and f/4 optics at 90 K, as shown in Figure 2.17.

Figure 2.17: 15 µm pitch 640×512 FPA images at 90 K.

In 2014, Katayama et al. showed FPA, which had 320×256 pixel format and 30 µm pitch with 6 µm cut-off wavelength. At 77 K, the NETD value is 250 mK with 200 ms integration time and f/2.3 optics [86]. The thermal image taken with these FPA can be seen in Figure 2.18.
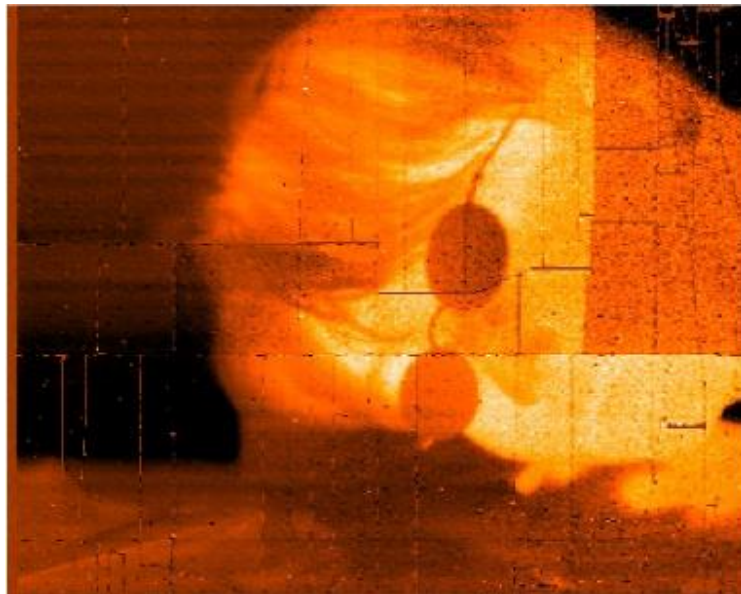
Figure 2.18: The image taken with FPA of Katayama et al. at 77 K [86].

The following year, Razeghi and her colleagues revealed the pMp design, which is also one of the unipolar designs T2SL FPA with 27 µm pitch and 320×256 array size [87]. The peak responsivity of FPA was acquired as 2.4 A/W, and the quantum efficiency was measured as 68.6% at 4.2 um wavelength. The NETD value is 11 mK and 15 mK at 81 K and 110 K, respectively, with 3.5×10^{11} Jones detectivity, as seen in Figure 2.19.

Figure 2.19: Thermal images taken with 320×256 pixel format FPA at temperatures from 81 K to 150 K [87].

In 2016, Miura et al. demonstrated a p-i-n type InAs/GaSb T2SL FPA with 320×256 array size and 30 µm pitch. NETD of the FPA is 31 mK with 1.2 ms integration time and f/2.3 optics at 77 K [88]. The thermal image of this camera can be seen in Figure 2.20.

Figure 2.20: Infrared image of Miura et al. FPA [88].

The same year, Zhou et al. revealed 384×288 pixels MWIR p-i-n T2SL FPA with 25 µm pitch [89] FPA had 18 mK NETD with 50% cut-off wavelength of 4.1 um from 77 K to 100 K, as shown in Figure 2.21.

Figure 2.21: Outdoor image of p-i-n T2SL FPA [89].

In 2017, XBn LWIR FPA with 15 µm pitch and 640×512 array size called Pelican-D was demonstrated by Klipstein et al. [90]. The quantum efficiency is approximately 50%, NETD is 13 mK with 1.3 ms integration time, and f/2.7 optics. The same year, dual-band MWIR/LWIR HD-format superlattice-based FPA with 12 µm pitch and 1280×720 array size was proposed with the partnership of HRL Laboratories and VISTA program [15]. The NETD for MWIR is 27.44 mK and for LWIR 27.62 mK with f/4.21 optics at 80 K, as shown in Figure 1.4 previously. Again in 2017, Sharifi et al. presented 2k×2k with 10 µm pitch and 1k×1k 5 with µm pitch MWIR FPAs [91]. NETD value of 2k×2k superlattice-based FPA is 22 mK and 30 mK with f/3.9 optics at 120 K and 150 K, respectively, as shown in Figure 2.22.

Figure 2.22: The images taken with 2k×2k superlattice-based FPA at 120 K and 150 K, respectively [91].

Jenkins et al. showed 5 µm pitch 1k×2k array size MWIR FPA with quantum efficiency larger than 60% without anti-reflection coating as shown in Figure 2.23 [92]. Again in 2017, Jiang et al. proposed a combination of PπMN and unipolar barrier bias selectable dual-band MWIR/LWIR FPA with 320×256 array size [75].

Figure 2.23: Images captured with 5 µm pitch 1k×2k array size MWIR FPA at 150 K [92].

In 2018, Ting et al. proposed e-SWIR, MWIR, and LWIR T2SL FPAs with a unipolar barrier in a conference proceeding [93]. e-SWIR FPA with 640×512 array size had 25% quantum efficiency without AR coating at 200 K. The image taken with e-SWIR FPA at 180 K is shown in the left of Figure 2.24.
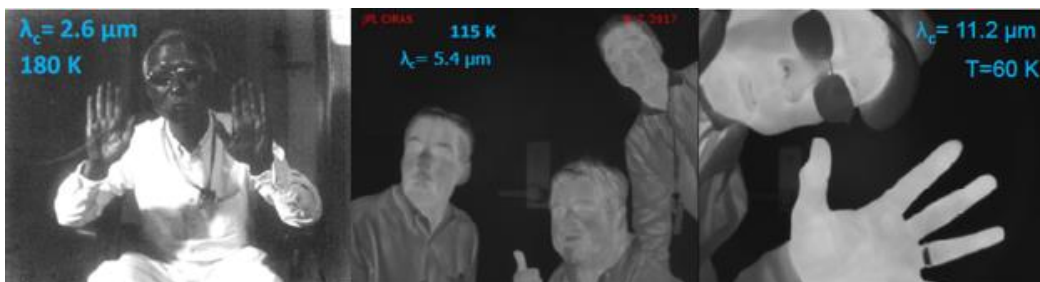
Figure 2.24: The images taken with 640×512 e-SWIR, MWIR, and LWIR FPAs, respectively.

MWIR FPA with 640×512 had 20.0 mK NETD with f/7.8 optics at 115 K, as seen in the middle of Figure 2.24. LWIR FPA with 640×512 pixel array had 37% quantum efficiency and 11.2 um cut-off wavelength without AR coating at 60 K, as shown in the right of Figure 2.24. Razeghi and his colleagues presented the latest bias selectable SWIR/MWIR dual-band type-II superlattice-based FPA, fabricated at their laboratory in 2021, as shown in Figure 2.25 [94].
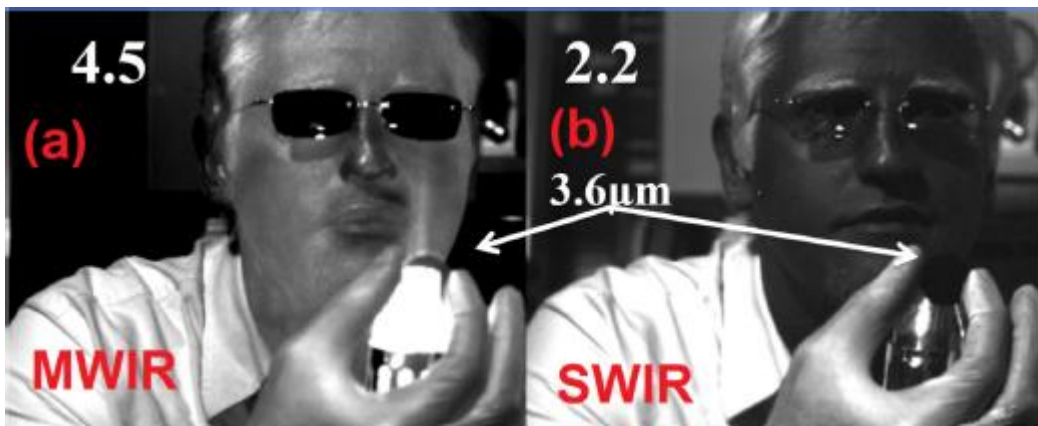
Figure 2.25: Infrared images shot with bias selectable SWIR/MWIR dual-band superlattice-based FPA. The person held a heat gun behind a narrow-band filter, centered at 3.6 µm. The heat-gun can be seen with MWIR part of FPA but cannot be seen with SWIR part of FPA [94].

CHAPTER 3

FABRICATION OF TEST PIXELS

In this chapter, the fabrication steps of the samples to be characterized will be presented. Two different mask sets were used to produce test samples. The first mask set, named MAPO (Mesa Array and Process Optimization), has no passivation layer. Therefore, the second mask set, named SLS TEST, was designed by Selçuk Özer to investigate the effect of the passivation process. Some part of the processed structure is the patented product. Therefore, the details of the process flow will not be shared. The applied process steps to samples for two mask sets will be explained, respectively.

3.1   nBn T2SL Epilayer Design

The structure of the processed is known as nBn type-II superlattice structure. The $Al_xGa_{1-x}Sb$ electron unipolar barrier layer is stated between N-Structure InAs/AlSb/GaSb with n-doped superlattice active layers, as shown in Figure 3.1. Thus, the SRH-based dark current level will be reduced, as mentioned in Section 2.3.5. In the absorption layers of the design, which is known N-Structure InAs/AlSb/GaSb T2SL, two monolayers of AlSb are placed between InAs and GaSb layers through the growth direction to behave as an electron barrier leading to reducing the diffusion current by blocking the thermally-generated electrons. Moreover, the AlSb barrier between InAs/GaSb layers has enhanced the overlap between the electron and hole wavefunctions [64] and caused to increase the optical absorption. Two absorption layers with different band-gap energy cause the pixels to be processed to operate at different wavelengths according to the bias polarization. The schematic illustration of the processed design and its SEM image can be seen in Figure 3.1 and Figure 3.2, respectively.
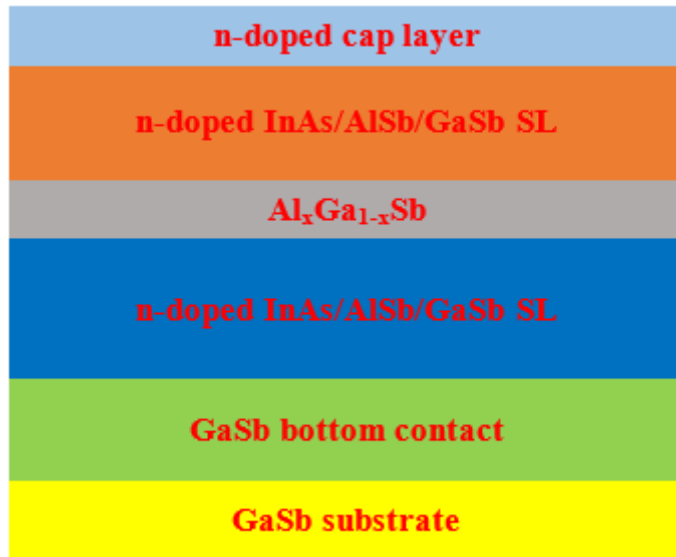
Figure 3.1: The schematic illustration of processed design.
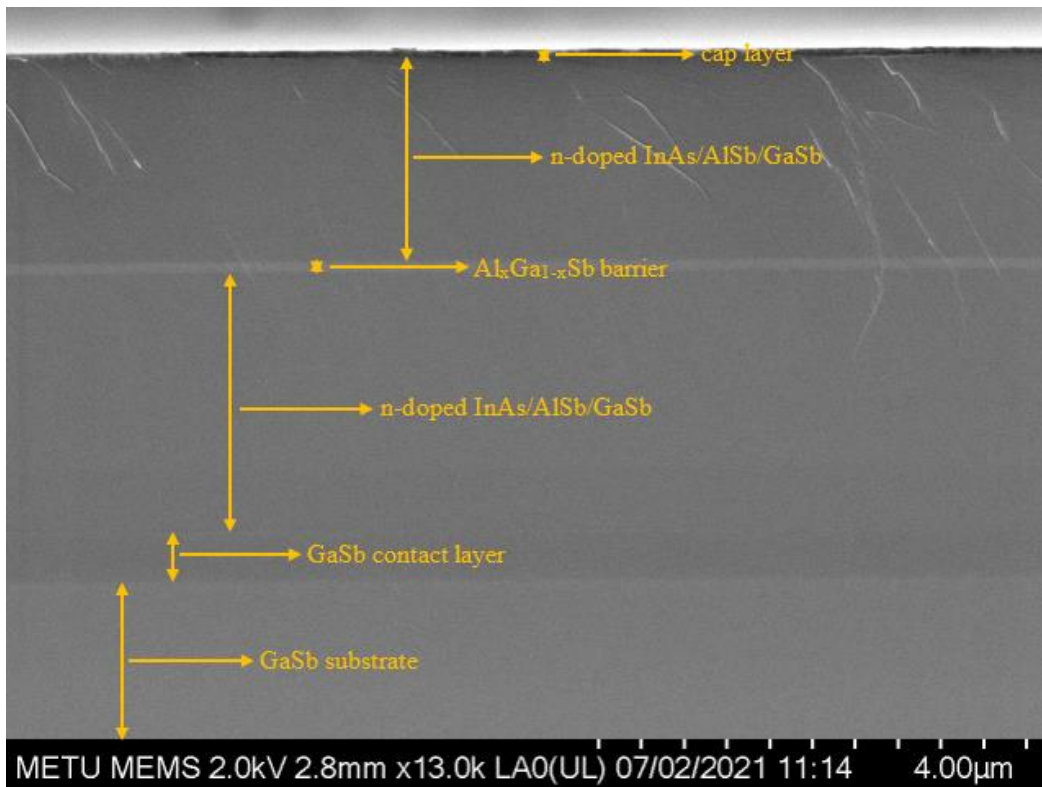
Figure 3.2: The SEM image of the processed design and the layers in it.

3.2   Operation Mechanism of Structure

The structure is designed to detect dual-color in MWIR with respect to the bias polarization. The energy band levels are illustrated in Figure 3.3 under no bias.
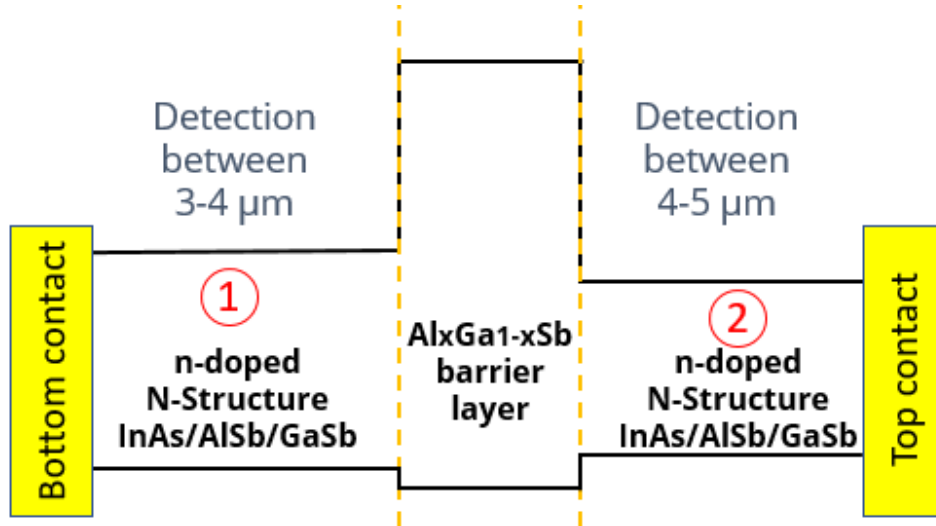
Figure 3.3: The energy band levels of the structure under no bias.

The majority electron carriers in the blue channel (4-5 µm) cannot flow the circuit due to the barrier layer when the positive bias is applied to the bottom contact and the detection occurs only in the red channel (3-4 µm), as seen in Figure 3.4. In the other case, when the top contact is biased with a positive voltage, the majority electron carriers in the red channel will be blocked by the barrier layer, and the blue channel will be active for detection, as in Figure 3.5. Thus, the detection will be occurred depending on the bias selectivity.
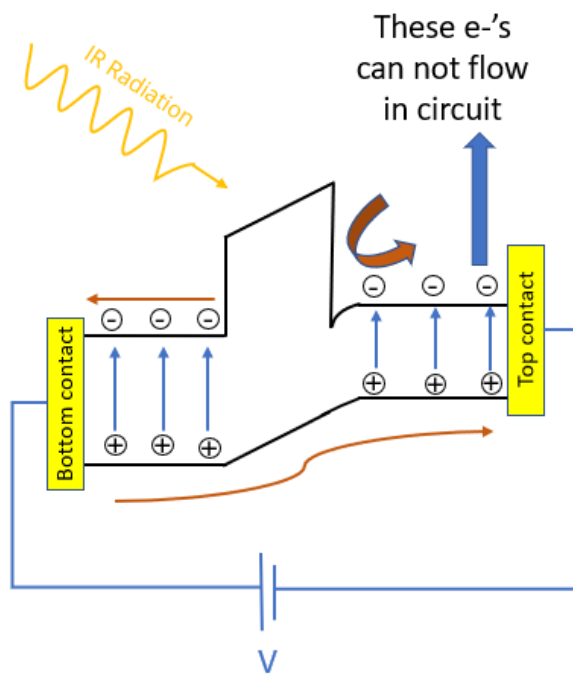
Figure 3.4: The energy band diagram of the structure when the positive bias is applied to bottom contact.
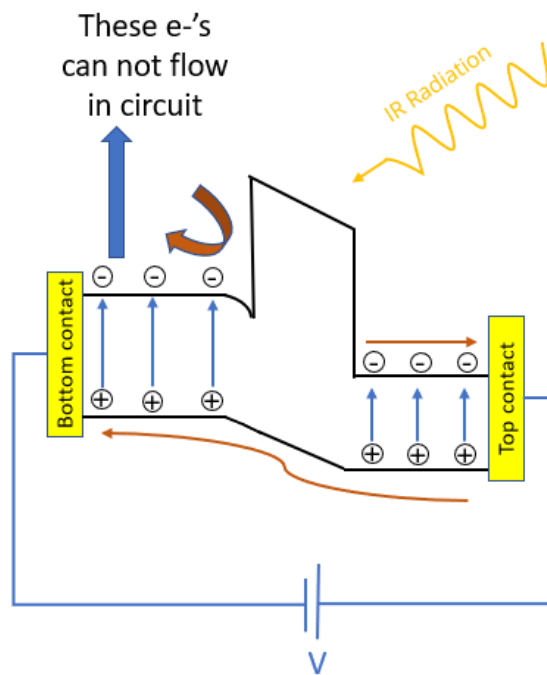
Figure 3.5: The energy band diagram of the structure when the positive bias is applied to the top contact.

3.3 Process Steps for MAPO Samples

The final pattern of MAPO mask set can be seen in Figure 3.6. There are different pixels sizes, ranging from 100 µm to 250 µm without the optical aperture and 300 µm with the optical aperture on MAPO pattern. Since this mask set has no passivation layer, the process steps except passivation, which are the sample cleaning, ground etch lithography, ohmic contact lithography, annealing step, mesa lithography, dicing, mesa etch lithography, and final cleaning steps were applied to the samples and will be explained below, respectively.
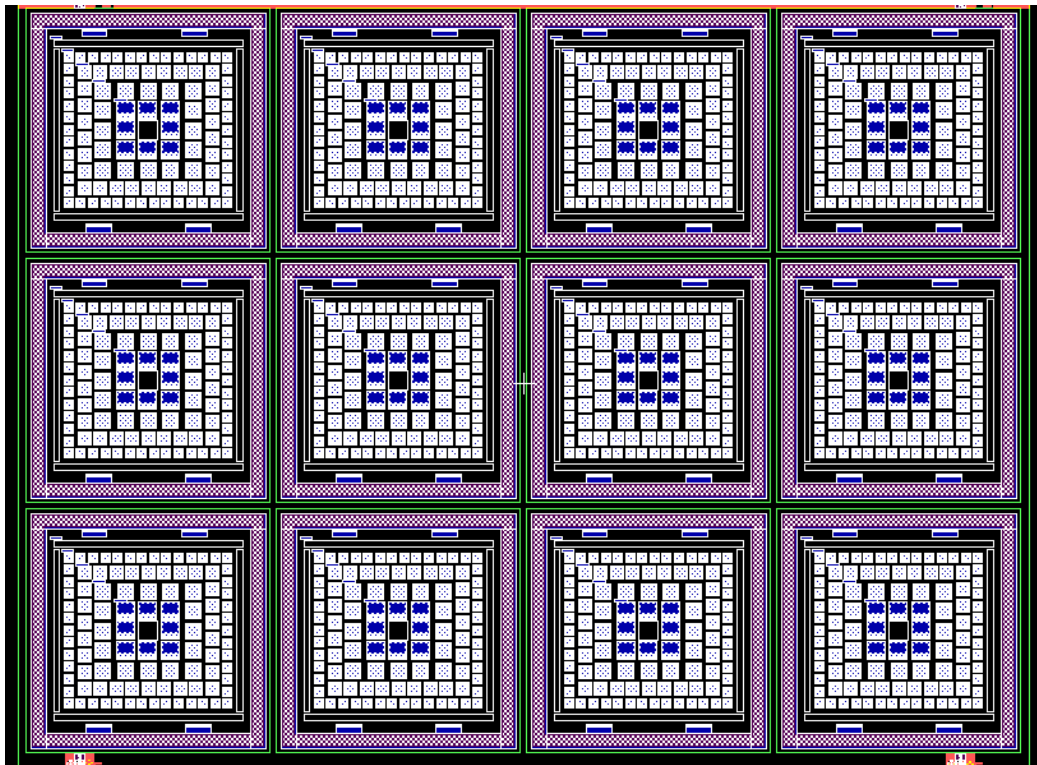
Figure 3.6: Final pattern of MAPO mask set.

3.3.1 Sample Cleaning

In order to make a die-level fabrication, two dies, labeled D1 and D2 with 18.2 mm × 15.7 mm size, were diced. Then, the coated photoresist on the dies used

to protect the surface of the wafer from dicing operation was cleaned with acetone and alcohol, respectively. Moreover, the impurities or defects leftover from the growth process were cleaned with a solvent consist of deionized water and hydrochloric acid by dipping. The difference between the two dies is that the cap layer of D2 was etched before ground etch lithography. Hence, the same process steps will be applied to D1 and D2, and the difference in the dark current density level will be investigated. Therefore, the reference sample with the pattern and D2 without any pattern were etched together within the solution to citric acid, deionized water, phosphoric acid, and hydrogen peroxide for one and half minutes. The SEM images of the reference sample with an etched cap layer can be seen in Figure 3.7. The deionized water and hydrochloric acid cleaning were repeated for D2.
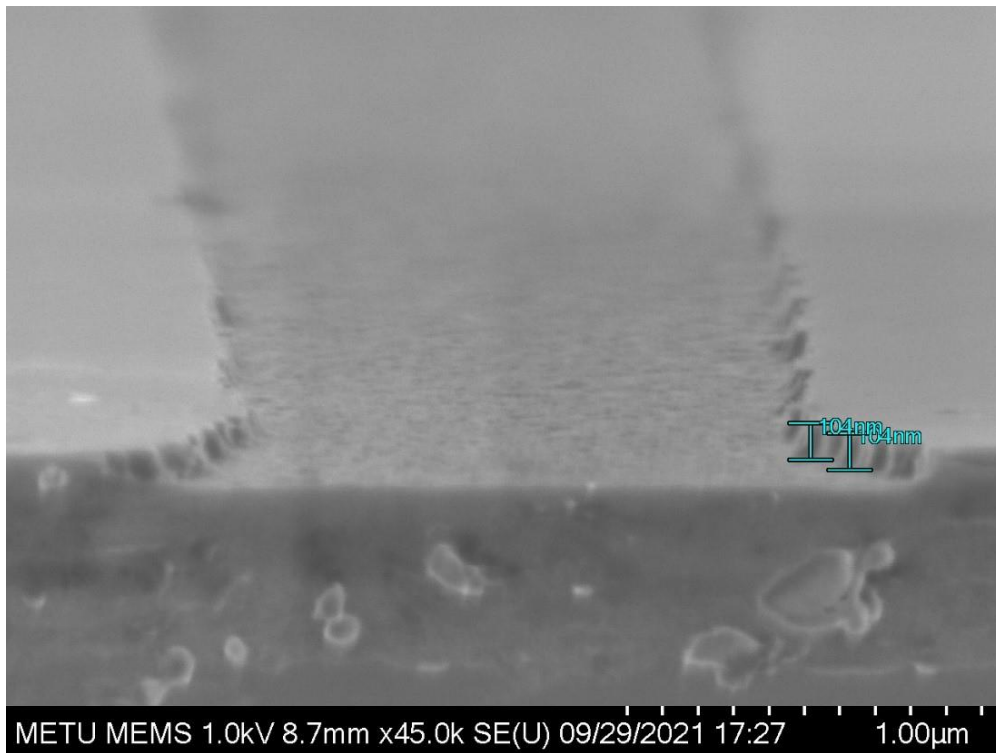
Figure 3.7: The SEM image of the reference sample with 100 nm etch depth. The thickness of the cap layer is 100 nm.

3.3.2   Ground Etch Lithography

The cleaned D1 and D2 were coated S1813 photoresist with specific rpm and time values via BIDTEC SP-100. Then, the soft bake operation to solidify PR was completed for D1 and D2 at 115 ℃ for one minute with a hot plate. The back-side cleaning of photoresist residuals was done with acetone to prevent the leveling problem during the exposing step. Firstly, the edge-bead pattern was exposed to D1 and D2 with the specified recipe with EVG 620 NT mask alignment system, and the exposed edge-bead pattern was developed with the MF-319 developer. Then, the ground etch pattern was exposed to D1 and D2 according to the adjusted recipe with EVG 620, and again the ground etch pattern on the dies was developed with the MF-319 for a certain time. Thus, the ground etch pattern was transferred on D1, as seen in Figure 3.8.
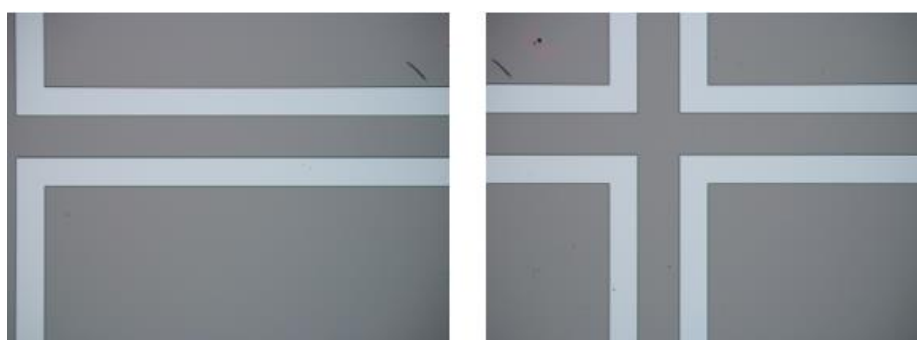
Figure 3.8: The ground etch pattern on D1 after development with MF-319 by taking with the optical microscope.

Before the wet etch step, the hard bake operation was executed at 120 ℃ for five minutes to stabilize the exposed pattern for etching steps. In order to see the effect of the ground contact depth, it was decided to get two different ground contacts from the bottom contact layer and the bottom superlattice layer of D2. The wet etch solution containing citric acid, deionized water, phosphoric acid, and hydrogen peroxide was prepared to etch until the bottom contact of the nBn type-II superlattice structure. Before dipping D1 and D2 into the solution, the thickness of the PR was measured with Dektak 8 Surface Profiler. The thickness of the PR on D1 and D2 is

1400 nm approximately. Therefore, to reach the bottom contact layer for D1 and bottom superlattice layer for D2, the total-etch depth must be equal to 4.7 µm and 3.4 µm at least, respectively.

The dies dipped into the solution several times, and the etch depths were measured with Dektak 8 after every dip step. The total-etch depths were measured as 4.7 µm and 3.4 µm for D1 and D2, respectively, as desired. Then, the left side of D2 was coated S1813, and the hard bake step was repeated. Thus, the right side of D2 was etched to reach the inside of the bottom contact layer. After that, the dies were cleaned with acetone and alcohol, and the solvent consist of deionized water and hydrochloric acid, respectively. The images of D1 and D2 after the ground etch step can be seen in Figure 3.9 and Figure 3.10, respectively.
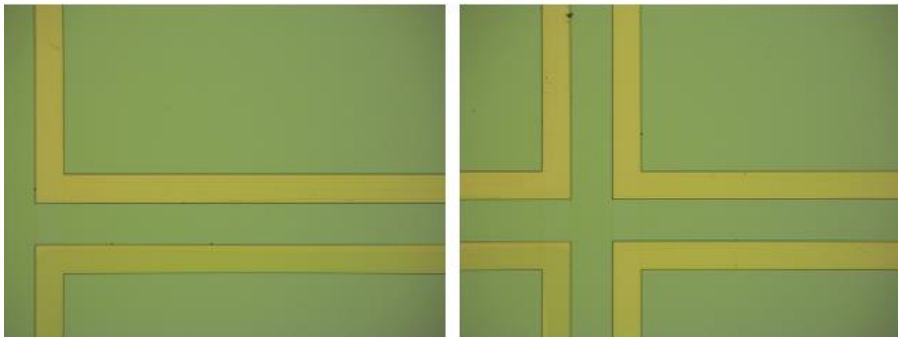
Figure 3.9: The optical microscope images of D1 after ground etch.
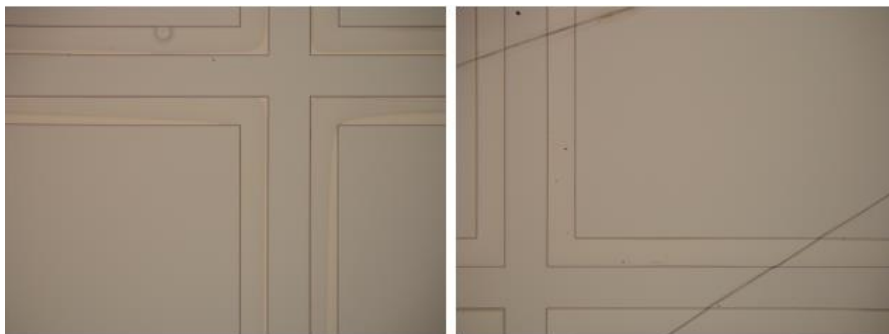
Figure 3.10: The optical microscope images of D2 after ground etch.

3.3.3 Ohmic Contact Lithography and Annealing

In this step, the pixels with different sizes were patterned on the dies to get a connection from the top of the pixels. Therefore, SPR220-3 PR, which is thicker than S1813, was spin-coated with BIDTEC SP-100 to protect the formed pattern previously. The soft bake step was performed at 115 ºC for one minute. The back-side cleaning of D1 and D2 was completed with acetone. Then, the edge-bead pattern was exposed via EVG620 and developed with the MF-319 developer. The ohmic contact pattern was exposed via EVG620 and developed with MF-319 for a specific time. The PR residuals from lithography were cleaned with oxygen plasma after ensuring the dimensions of pixels were as desired. The optical microscope images of D1 at the end of ohmic contact lithography can be seen in Figure 3.11.
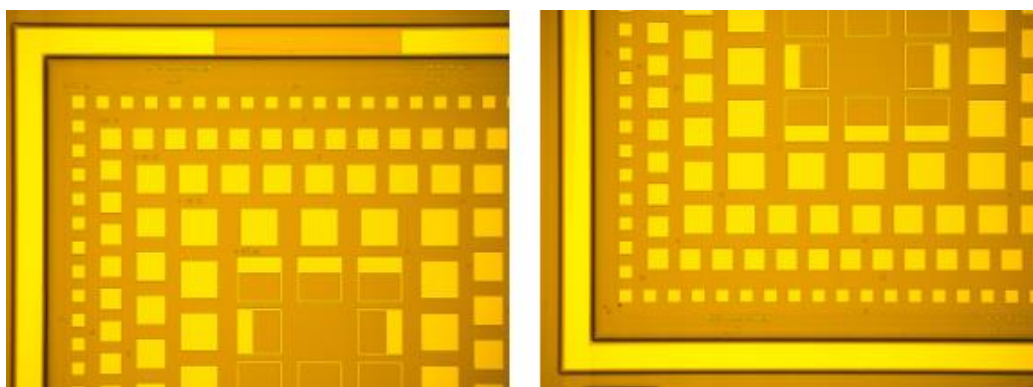
Figure 3.11: Optical microscope images of D1 after ohmic contact lithography with oxygen plasma.

The deposition of the ohmic metals, which are Titanium/Platinum/Gold, respectively, were deposited in desired thicknesses with the optimized recipe via BESTEC-II Sputter Systems. After that, D1 and D2 were immersed and left in acetone to remove the deposited metals from the dies where there is no pattern for a day.

D1 and D2 dies were cleaned with acetone to remove ohmic metal residuals on the surface of the samples. However, some of the deposited metals which should be lift-off was not released. Therefore, D1 and D2 were vibrated in acetone using

ultrasonic cleaner at a particular time and power value. The oxygen plasma was applied to the dies for two minutes. The optical microscope images of D1 and D2 are shown in Figure 3.12 and Figure 3.13 at the end of the ohmic contact lithography process.
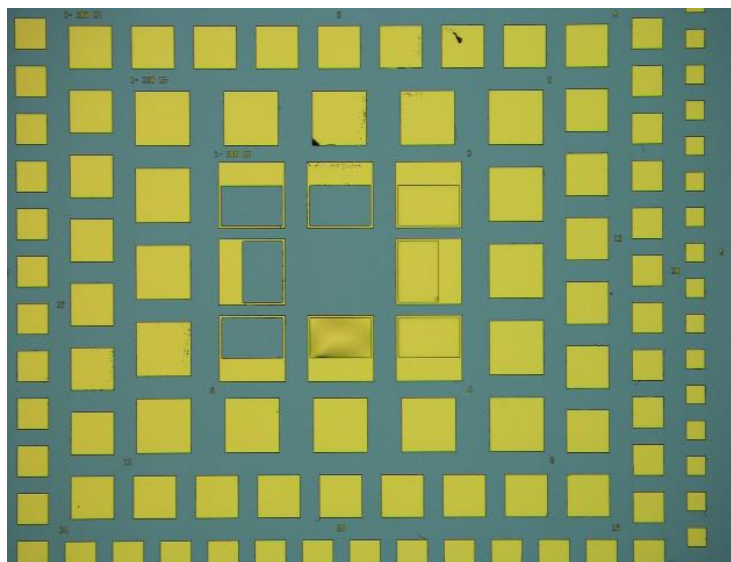
Figure 3.12: The optical images of D1 after ohmic contact lithography.
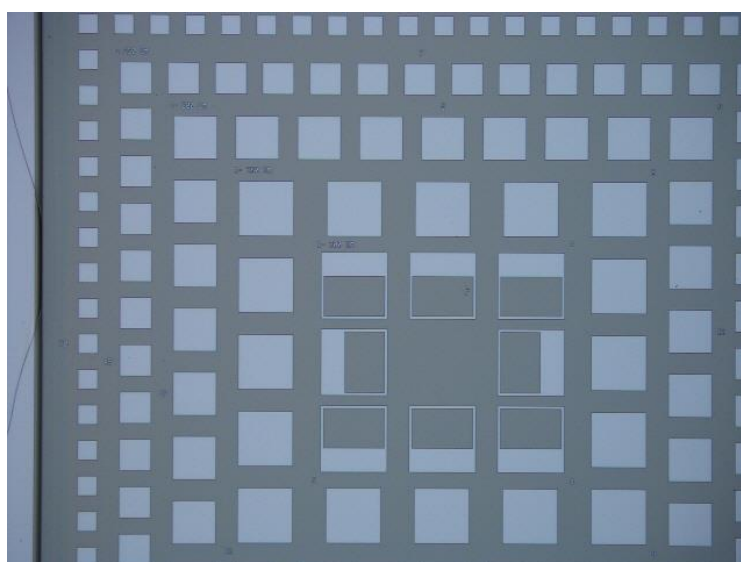
Figure 3.13: The optical images of D2 after ohmic contact lithography.

After that, the annealing operation was completed at 290 ℃ for one minute with FC150 since it can be used as a rapid heater under vacuum in order to make the contact points with ohmic characteristics.

3.3.4 Mesa Etch Lithography and Dicing

In order to etch the surfaces other than the pixel structures in the dies, the mesa etch mask was patterned on D1 and D2. The S1813 photoresist was spin-coated on dies with specific spin speed and time. Then the dies were heated with the hot plate at 115 ℃ for one minute. After the exposure and the development of the edge-bead pattern, the exposure and the development of the mesa etch pattern were completed, respectively, using EVG 620 for the exposure and MF-319 development for the development steps. After ensuring the pattern development on the dies, the hard-bake operation was done at 120 ℃ for five minutes. The images of D1 and D2 are represented in Figure 3.14 and Figure 3.15, respectively.
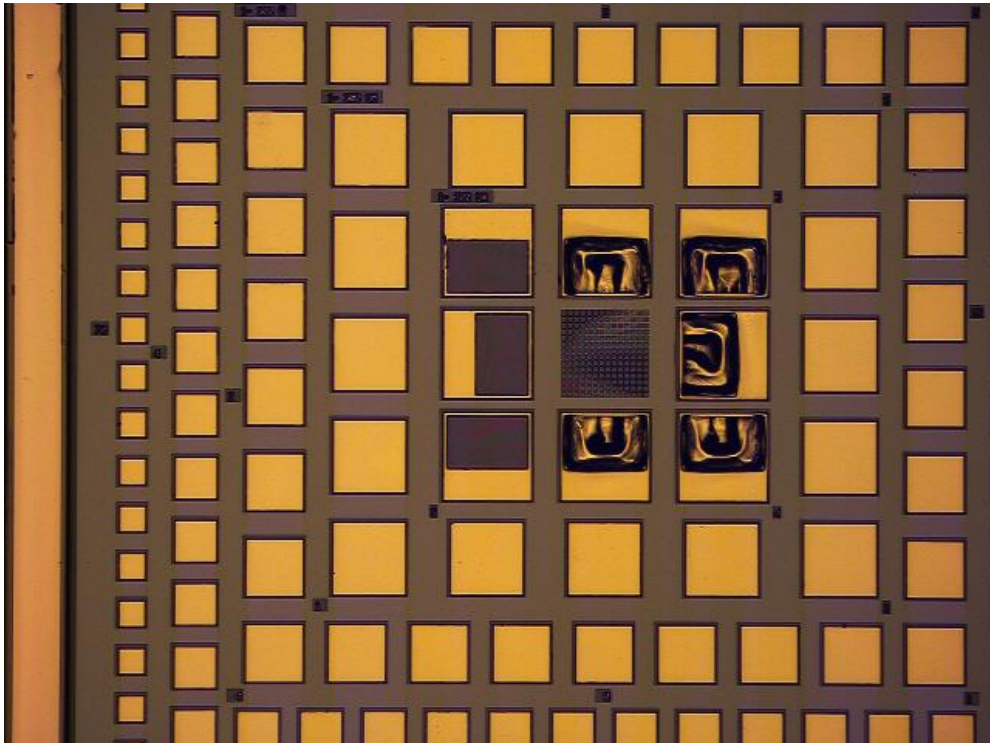
Figure 3.14: The optical microscope image of D1 after hard-bake for mesa etch.
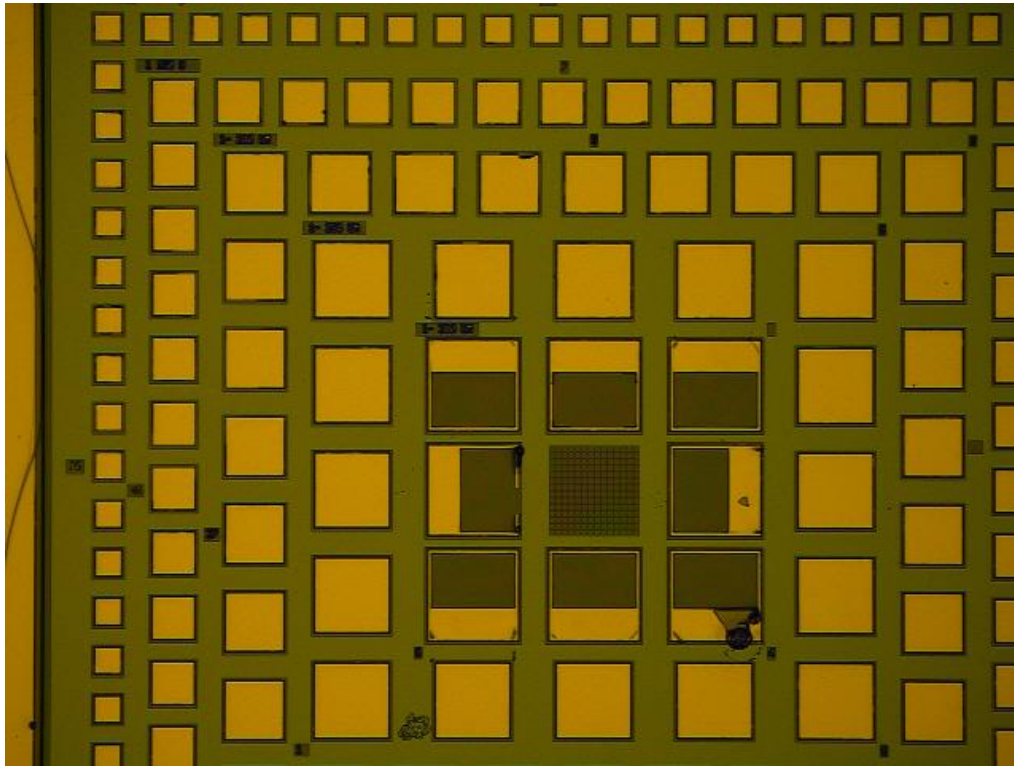
Figure 3.15: The optical microscope image of D2 after hard-bake for mesa etch.

The dies were diced with DISCO, DAD3350 Automatic Dicing Saew Machine to acquire twelve MAPO samples. Some of these samples were damaged during the dicing step. Therefore, these damaged samples were used as reference samples to measure the etch depth using a scanning electron microscope (SEM). The combined image of D2 samples after the dicing is shown in Figure 3.16.
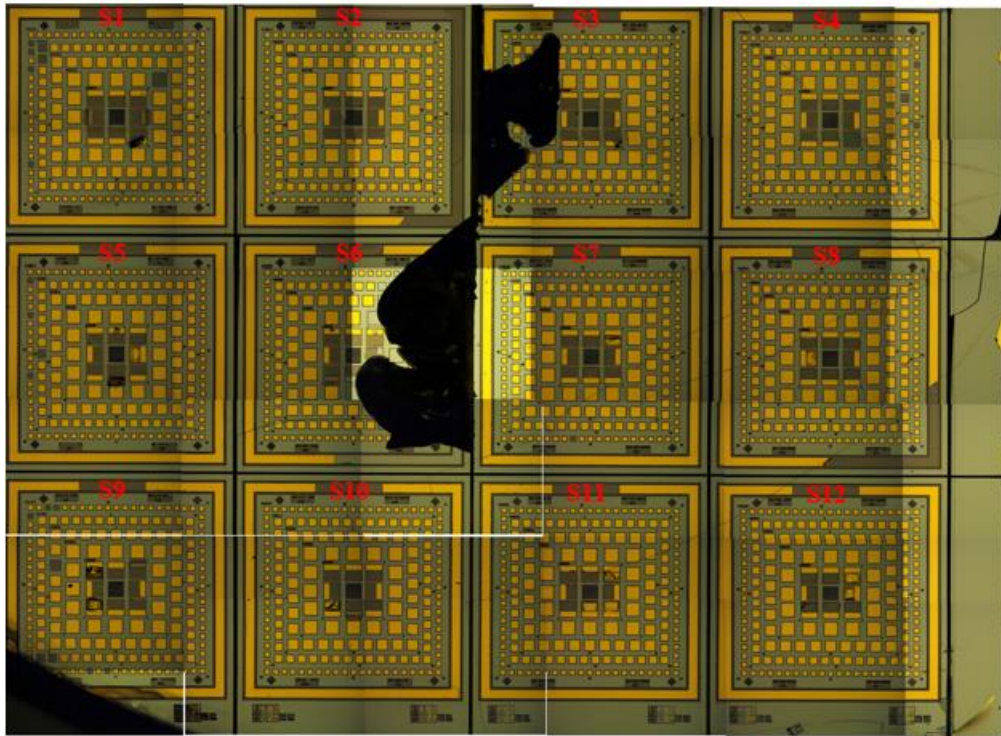
Figure 3.16: The combined image of D2 after the dicing step, the samples labeled as S3 and S6 were damaged as seen.

3.3.5   Mesa Etch and Cleaning

For the mesa etch step, there are two etch profiles. One of them is to etch the sample into the barrier layer, and the other is to etch the sample into the contact layer. The mesa etch profiles of D1 are illustrated in Figure 3.17 and Figure 3.18, respectively. In addition to that, the cap layer of D2 was removed, and the ground contact of its half-right part is in the superlattice layer, unlike D1. The etch profile of D2 for mesa barrier and superlattice etch are shown in Figure 3.19 and Figure 3.20.
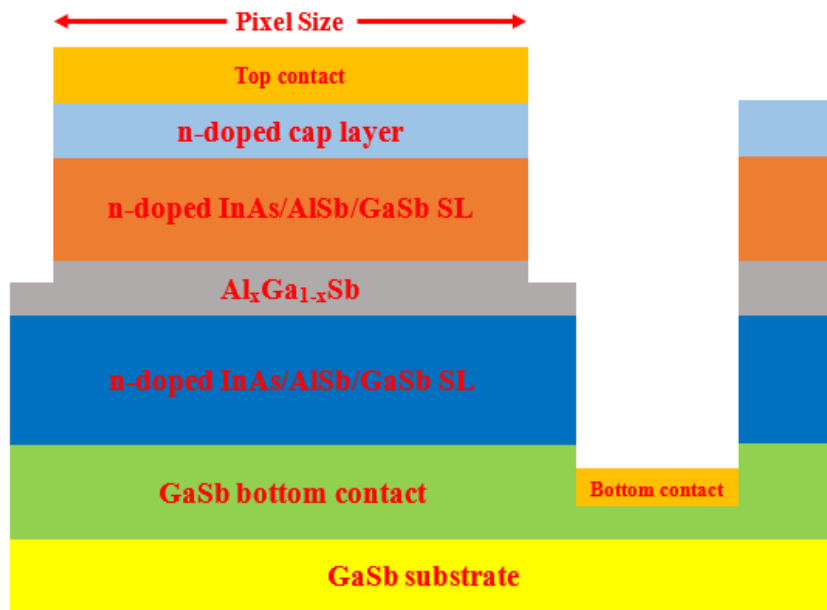
Figure 3.17: The mesa barrier etch profile of D1, the ground contact was taken from the bottom contact layer.
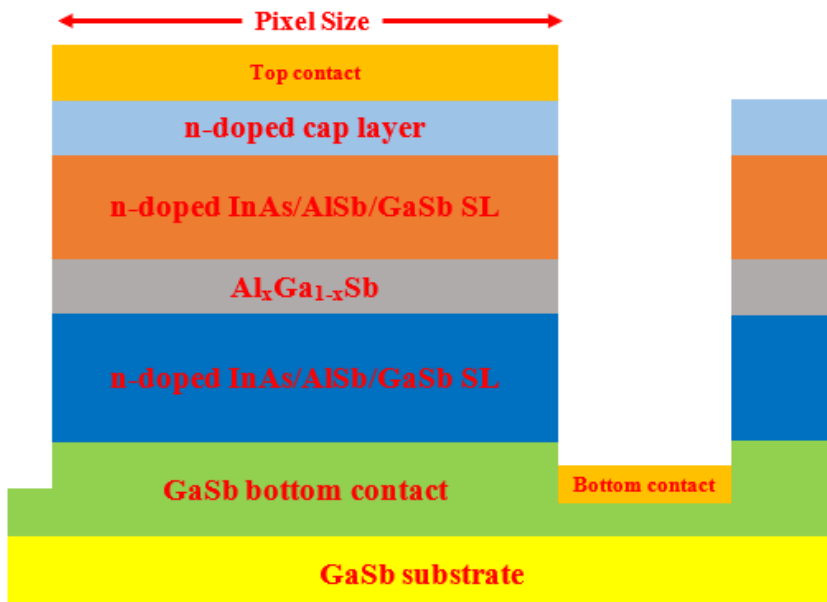
Figure 3.18: The mesa contact etch profile of D1, the ground contact was taken from the bottom contact layer.
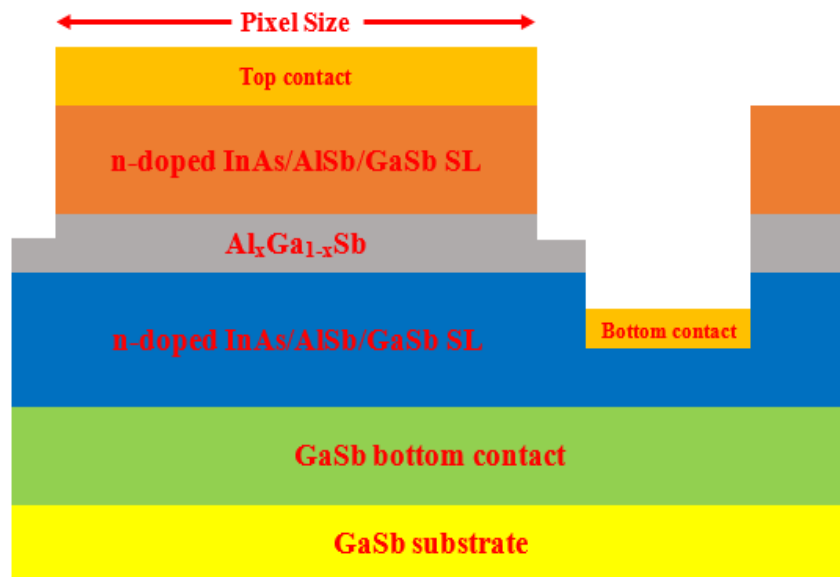
Figure 3.19: The mesa barrier etch profile of the D2 half-right part, the ground contact was taken from the bottom superlattice layer, and the cap layer was etched.
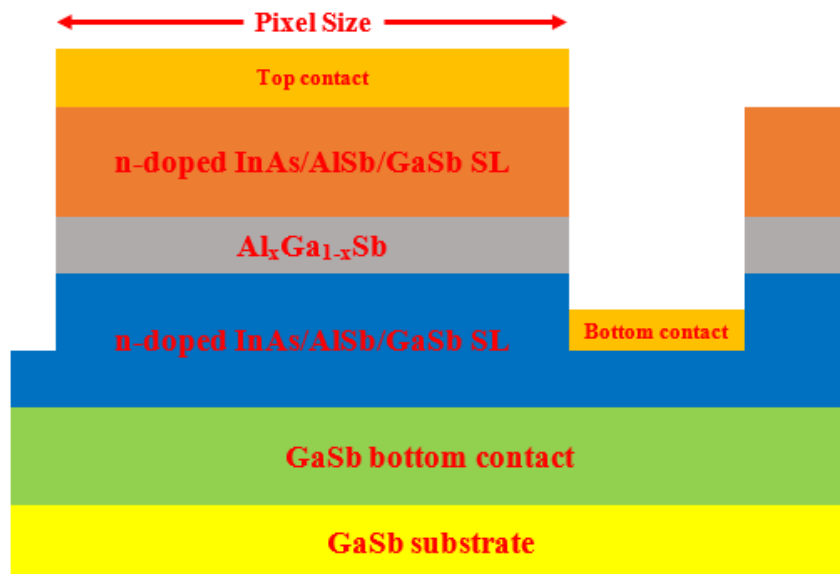
Figure 3.20: The mesa superlattice etch profile of the D2 half-right part, the ground contact was taken from the bottom superlattice layer, and the cap layer was etched.

Before starting to etch D1 and D2, two reference samples named as R1 and R2 were chosen to determine the etching speed of the solvents. Therefore, the mesa etch mask was exposed to R1 and R2, and two etch solutions named the fast etch solution and the slow etch solution were prepared for mesa barrier etch and mesa contact etch. Both etch solutions, which are composed of $C_6H_8O_7$ (citric acid), H_2O (deionized), H_3PO_4 (phosphoric acid), and H_2O_2 (hydrogen peroxide), were prepared at specific rates. Firstly, R1 was immersed in the fast etch solution for five minutes, a small part of R1 was cleaved and investigated in Hitachi SEM after the first dipping. The SEM image of the part of R1 can be seen in Figure 3.21.
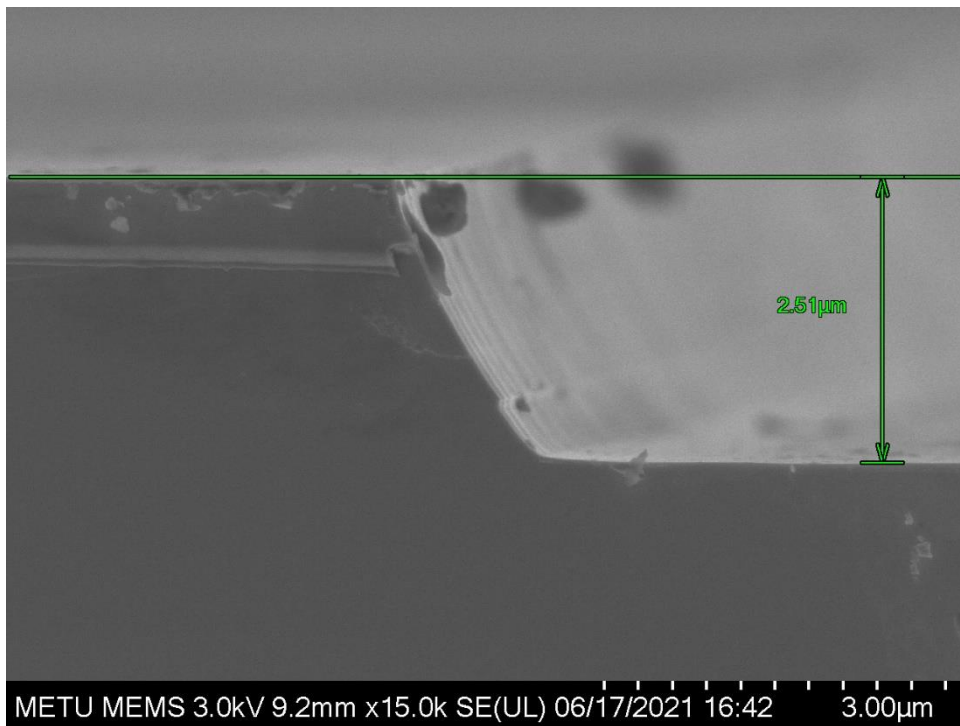
Figure 3.21: Etch depth of R1 after the first immersed for five minutes.

After several dipping, the required depth to etch into the contact layer had been reached, as seen in Figure 3.22.
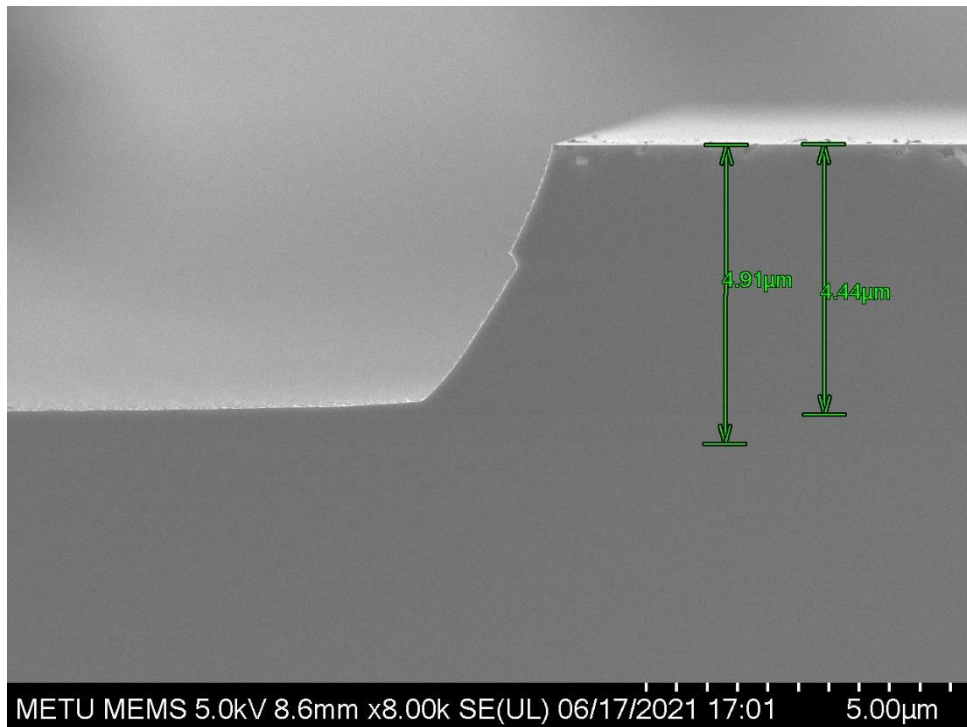
Figure 3.22: The final etch depth of R1, the etch process was stopped within the contact layer as desired.

Two solutions called the fast etch and the slow etch should be used for the mesa barrier etch, respectively. Since the barrier layer in the nBn structure is between 1950 nm and 2050 nm depth, the total etch depth after the mesa barrier etch process should be 2000 nm approximately. Therefore, some part of this depth, around 1500 nm, will be etched with the fast etch solution, and then the rest of etch depth will be etched with the slow etch solution to prevent over etch. The etch depth of R2 at the end of the fast etch and the slow etch processes can be seen n Figure 3.23.
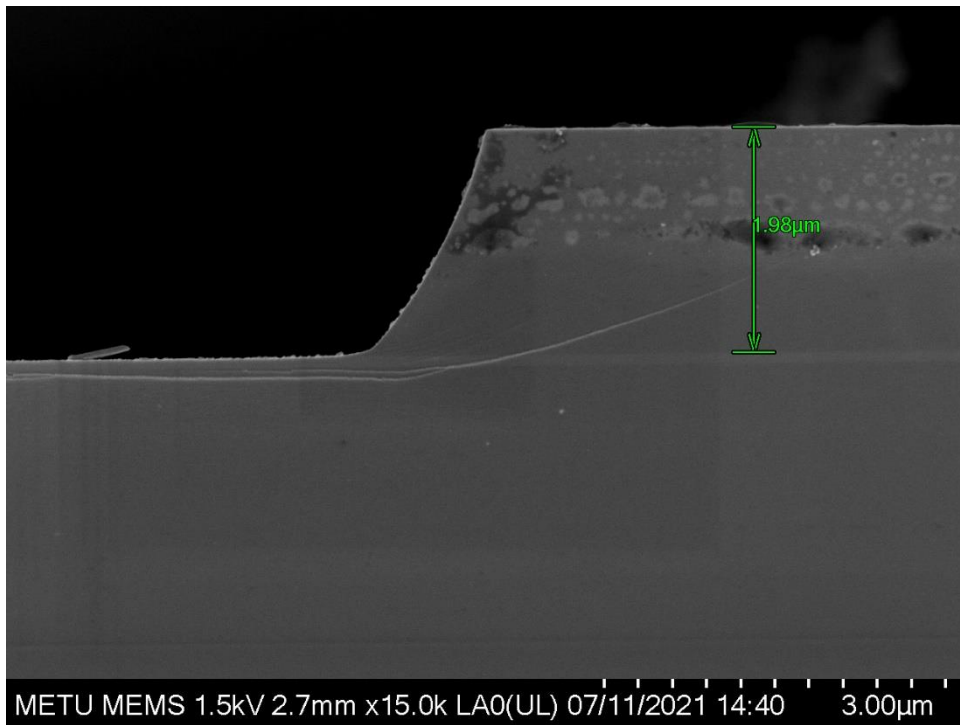
Figure 3.23: The total etch depth of R2 after the dipping into the fast etch solution and the slow etch solution, respectively.

After the etch rate for the fast etch, and the slow etch solution is determined, the samples of the first MESA group from D1, which is labeled as D1N1 from now on, were chosen to create mesa pixels. According to the given numbers in Figure 3.16, D1N1S1 and D1N1S4 were selected as the reference samples during etch process for mesa barrier and mesa contact etch, respectively. D1N1S7 and D1N1S10 were chosen for mesa contact etch, while D1N1S8 and D1N1S9 were selected for mesa barrier etch.

D1N1S1, D1N1S8, and D1N1S9 were immersed in the fast etch solution and the slow etch solution, respectively, a few times. The final etching depth of D1N1S1, the reference sample, was measured with SEM as shown in Figure 3.24.
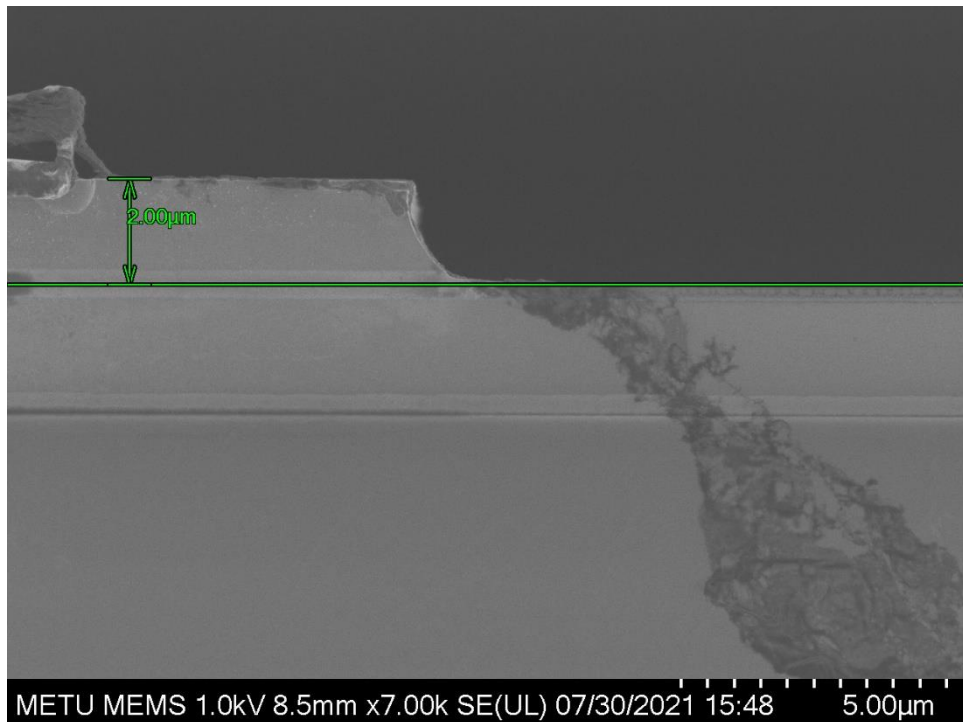
Figure 3.24: The SEM image of the reference sample labeled as D1N1S1 from D1N1 group. The desired etch depth within the barrier layer is achieved.

The fast etch solution was prepared for D1N1S4, D1N1S7, and D1N1S10 to mesa contact etch. At the end of the immersion, the measured final etch depth was 4.6 µm which corresponded to within the bottom contact layer of the structure, as demonstrated in Figure 3.25.

The other samples group from D1 labeled as D1N2 was etched with the same solution. D1N2S9 and D1N2S3 were determined as reference samples for mesa barrier etch and mesa contact etch, respectively. Moreover, D1N2S2 and D1N2S5 were selected for mesa contact etch. The last two samples from D1, D1N2S6, and D1N2S11, were chosen for mesa barrier etch. The SEM images of the reference samples' total depth at the end of the etching process for two-pixel profiles can be seen in Figure 3.26 and Figure 3.27 for mesa barrier etch and mesa contact etch, respectively.
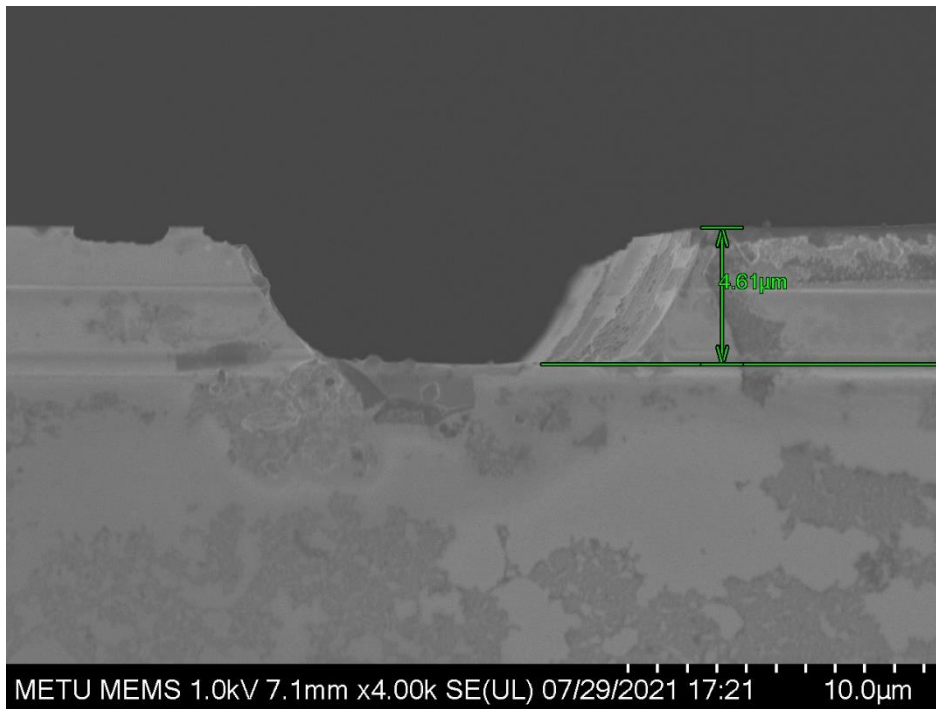
Figure 3.25: D1N1S4 SEM image at the end of the mesa etch to reach the bottom contact layer.
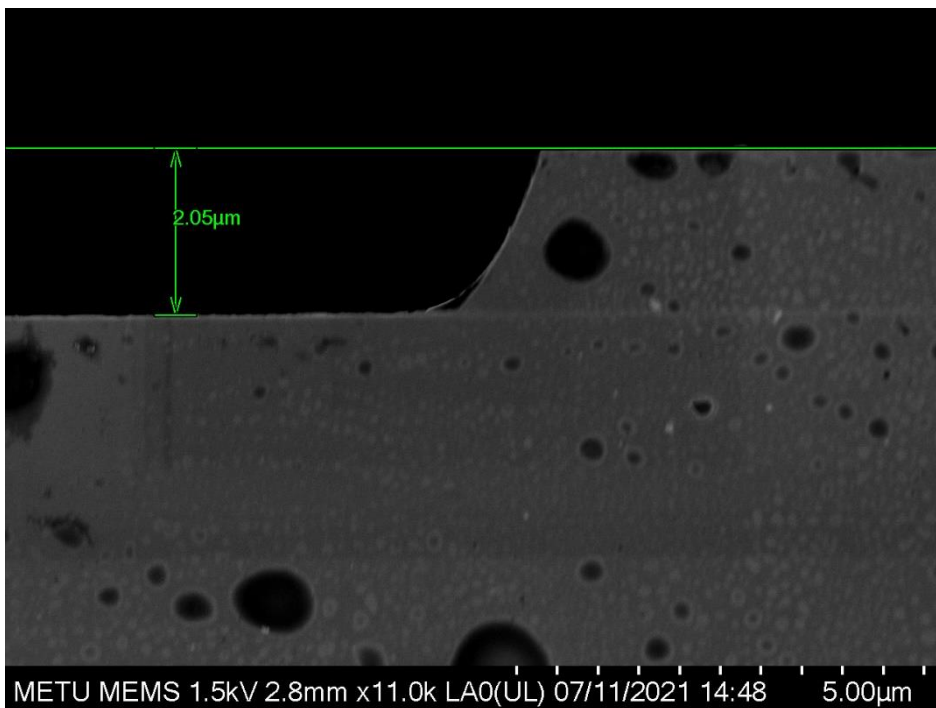
Figure 3.26: The SEM image of D1N2S9 from D1N2 for mesa barrier etch.
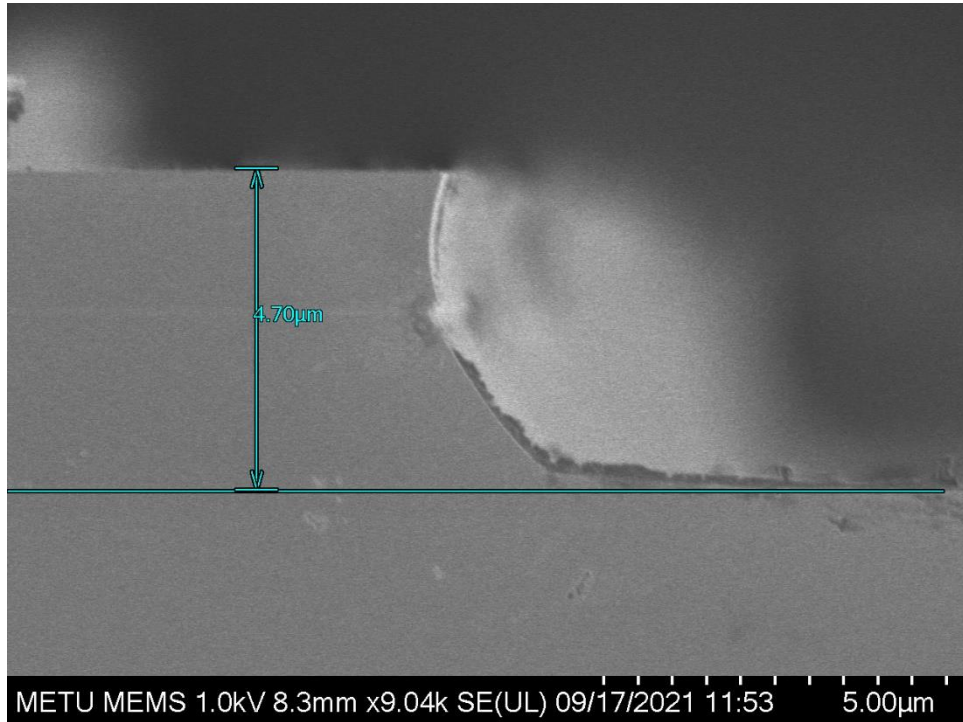
Figure 3.27: The measured etch depth of reference D1N2S3 from D1N2 after mesa contact etch step.

The half-right part of D2 was etched until 3.5 µm for taking ground contact from the bottom superlattice layer in the structure. Therefore, the mesa etch process was completed to stay inside the barrier and bottom superlattice layers. D2N1S8 and D2N1S3 were selected as reference samples for mesa barrier etch, and mesa superlattice etch, respectively, to investigate the etch depth with SEM. Using slow etch solution and fast etch solution, D2N1S8, D2N1S11, and D2N1S12 were etched inside the barrier layer, as seen from the reference D2N1S8 SEM image in Figure 3.28. D2N1S3, D2N1S4, and D2N1S7 were etched into the bottom superlattice layer, as shown from the SEM image of the reference D2N1S3 in Figure 3.29. In order to compare the effect of etching the bottom contact layer and the bottom superlattice layer in structure, the half-left part of D2 was etched at 4.7 µm, corresponding to the bottom contact layer for ground contact. Therefore, the mesa barrier etching depth of the samples on this half was done into the barrier layer such as in previous samples, and the mesa contact etch was applied until inside the bottom contact layer
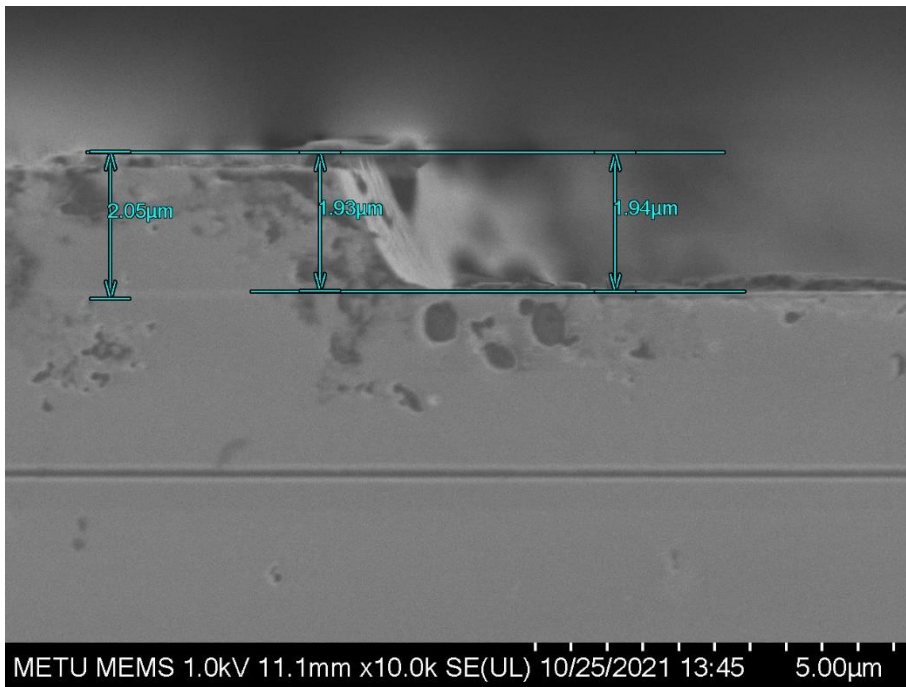
Figure 3.28: The SEM image of reference D2N1S8 for mesa barrier etch.
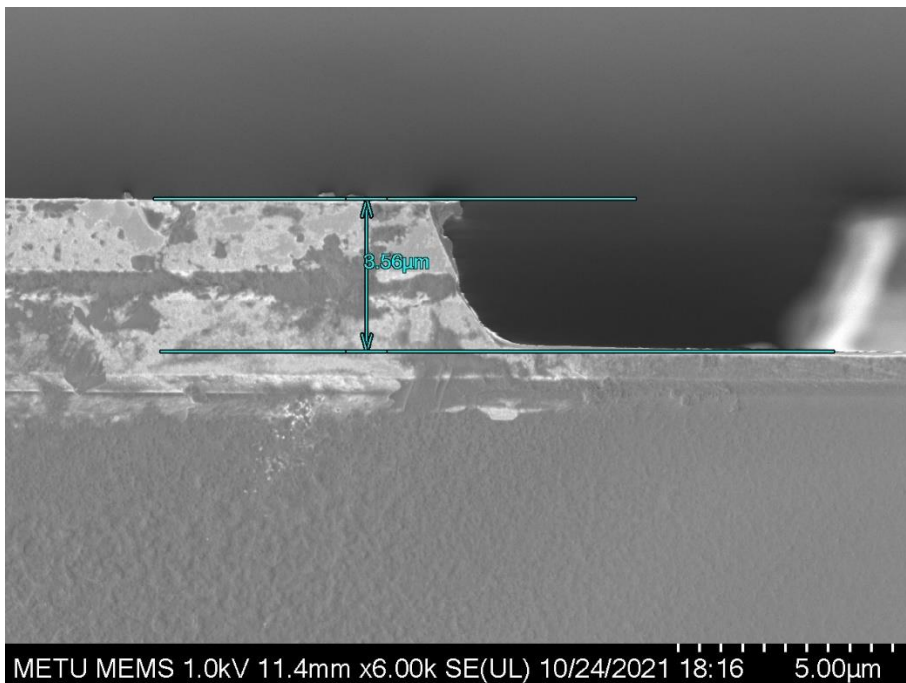
Figure 3.29: The SEM image of reference D2N1S3 for mesa superlattice etch.

for the selected samples. D2N2S9 and D2N2S6 from the half-left part of D2 were chosen as reference samples for mesa barrier and mesa contact etching, respectively. D2N2S1 and D2N2S10 had selected for mesa barrier etching. However, D2N2S1 was damaged during the etching process. Therefore, only D2N2S9 as a reference and D2N2S10 were etched with the fast and slow etching solution. The etch depth of reference D2N2S9 can be seen in Figure 3.30. Moreover, D2N2S2 and D2N2S5 would be etched with the fast etching solution for mesa contact etching, but a problem emerged during the etching preparation of D2N2S2 for mesa contact etching, and it was damaged. For this reason, only D2N2S5 and D2N2S10 were etched with reference samples by dipping the fast and the slow etching solutions to reach the contact layer and the barrier layer, respectively. The SEM images of reference samples, labeled as D2N2S9 for and D2N2S6 for mesa barrier and mesa contact etching, respectively, are in Figure 3.30 and Figure 3.31.
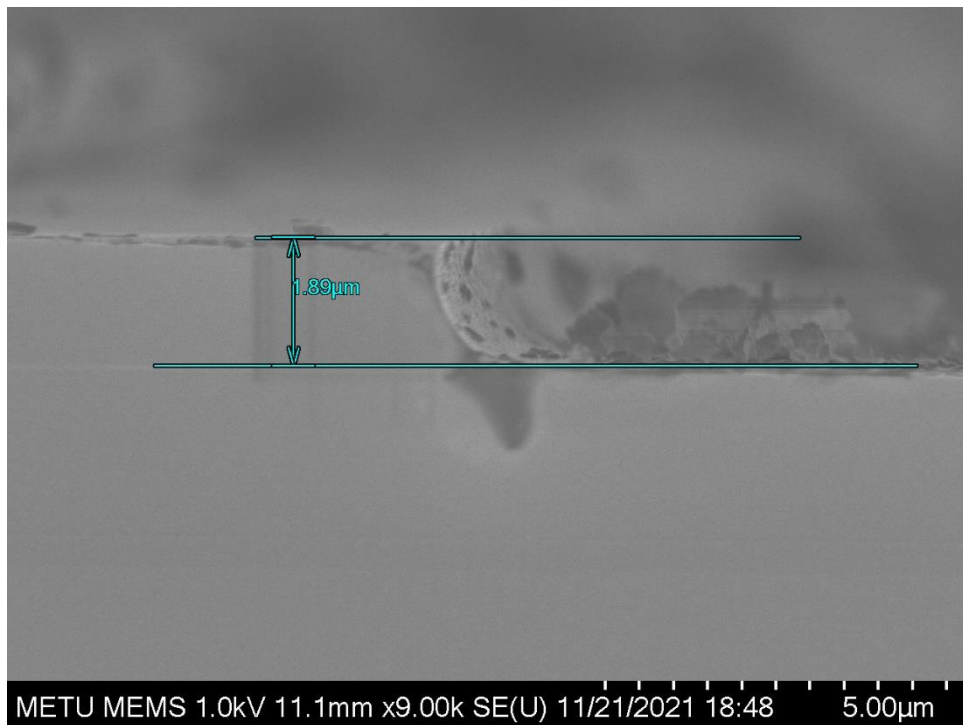
Figure 3.30: The measured etch depth for reference D2N2S9 for mesa barrier etch taken with Hitachi SEM.

71
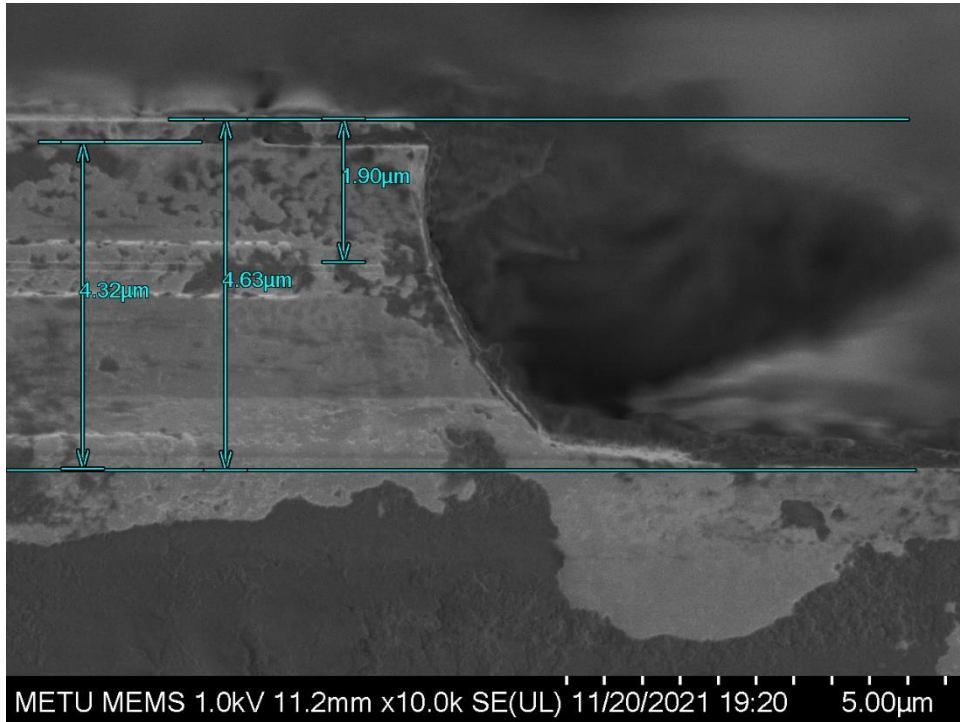
Figure 3.31: The SEM image of reference D2N2S6 for mesa contact etch. The etch depth corresponds to the inside of the bottom contact layer.

After the etching processes were completed, some of the samples were cleaned with the acid solution consisting of $C_6H_8O_7$, H_2O (deionized), and H_2O_2 which was optimized by Seval Şahin for her doctoral study to get rid of the etching residuals. Then, the samples were cleaned with acetone and alcohol to remove photoresist residuals on them. The samples were exposed to oxygen plasma for PR residuals which did not strip from the samples. Lastly, the HCl cleaning process was performed on MAPO samples for uncleaned residuals from the surface.

The combined optical microscope images of D2N1S4 and D2N1S11 samples can be seen in Figure 3.32 and Figure 3.33 at the end of the fabrication, respectively.
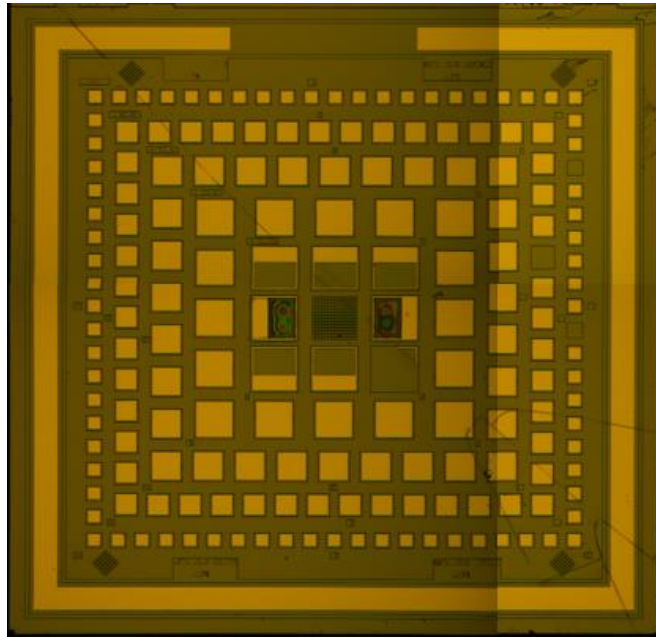
Figure 3.32: The surface of D2N1S4 after citric acid, acetone-alcohol, oxygen plasma, and hydrochloric acid cleaning, respectively.
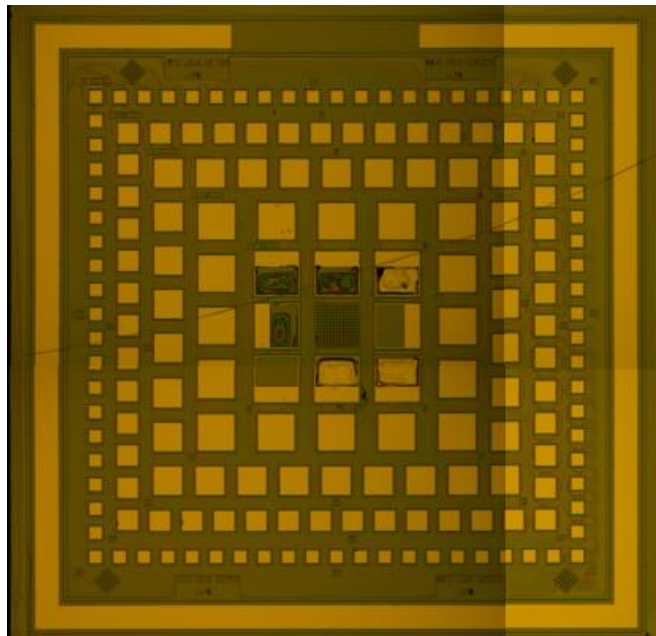
Figure 3.33: The surface of D2N1S11 after citric acid, acetone-alcohol, oxygen plasma, and hydrochloric acid cleaning, respectively.

3.4 Process Steps for SLS-TEST Samples

The SLS-TEST mask set is designed since there is no passivation layer from MAPO mask set to investigate the effect of the passivation process. The final pattern of SLS-TEST mask set can be seen in Figure 3.34. There are different pixels sizes, varying from 20 µm to 300 µm without the optical aperture, varying from 50 µm to 300 µm with the optical aperture, and mesa group pixels of 20 µm on SLS-TEST pattern.
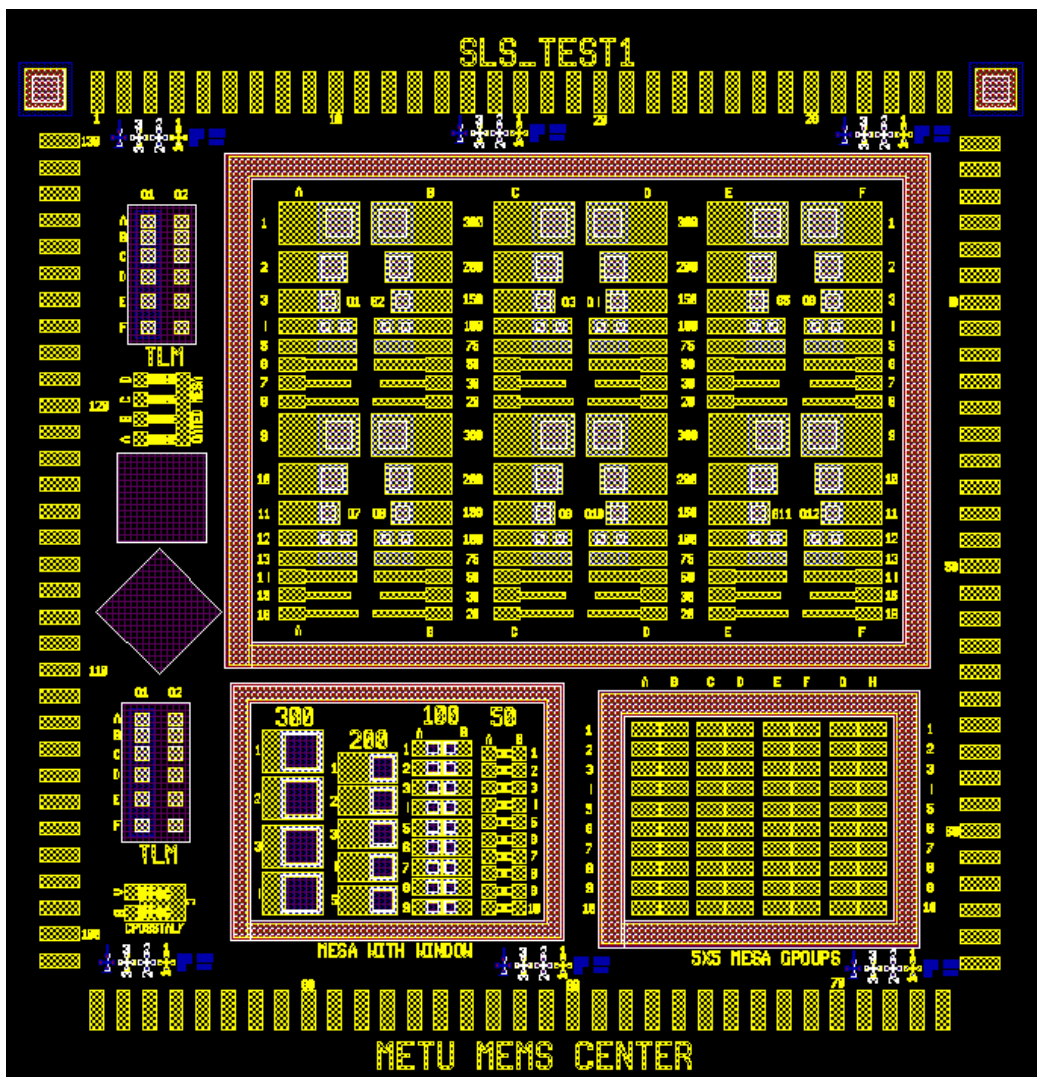
Figure 3.34: Final pattern of SLS-TEST mask set.

The process steps order of SLS-TEST mask has changed with respect to MAPO mask set, and the passivation step is added to flow. The sample cleaning, mesa etch lithography, ground etch lithography, passivation lithography, ohmic contact lithography, annealing, and final cleaning steps were applied to the samples, respectively.

Two dies labeled T1 and T2 with 12 mm × 12 mm size were fabricated with SLS-TEST mask set. The final mesa profiles of these samples are the shallow etch (the mesa barrier etch), and the deep etch (the mesa contact etch) as shown in Figure 3.17 and Figure 3.18, respectively. Since only the passivation step is added to the process flow of MAPO mask set, only the details about the passivation lithography are presented for SLS-TEST mask set.

After the sample cleaning, mesa etch lithography, and ground etch lithography steps were completed for T1 and T2, the passivation process was started. 100 nm SiO_2 was deposited on T1 and T2 with PECVD (Plasma Enhanced Chemical Vapor Deposition). After that, the S1813 photoresist was spin-coated on dies with specific spin speed and time. Then the dies were heated with the hot plate at 115 ℃ for seventy seconds. The exposure and the development of the passivation opening pattern were completed, respectively, using EVG 620 for the exposure and MF-319 development for the development steps. The samples T1 and T2 were immersed in BHF (buffered hydrofluoric acid) to remove SiO_2 on the contact areas, where ohmic metals will be deposited to get contact from the pixels. Then, the ohmic contact lithography, annealing, and final cleaning steps were done for T1 and T2, and the fabrication of the samples with passivation was finished. The optical images of T1 and T2 can be seen in Figure 3.35 and Figure 3.36, respectively.
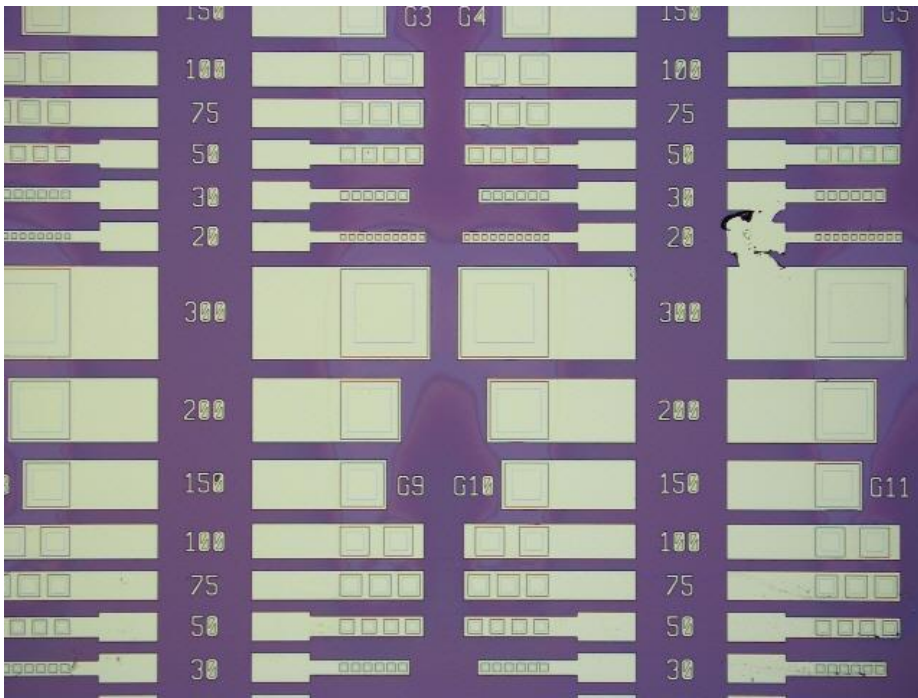
Figure 3.35: The optical image of T1, the shallow etch sample with passivation.
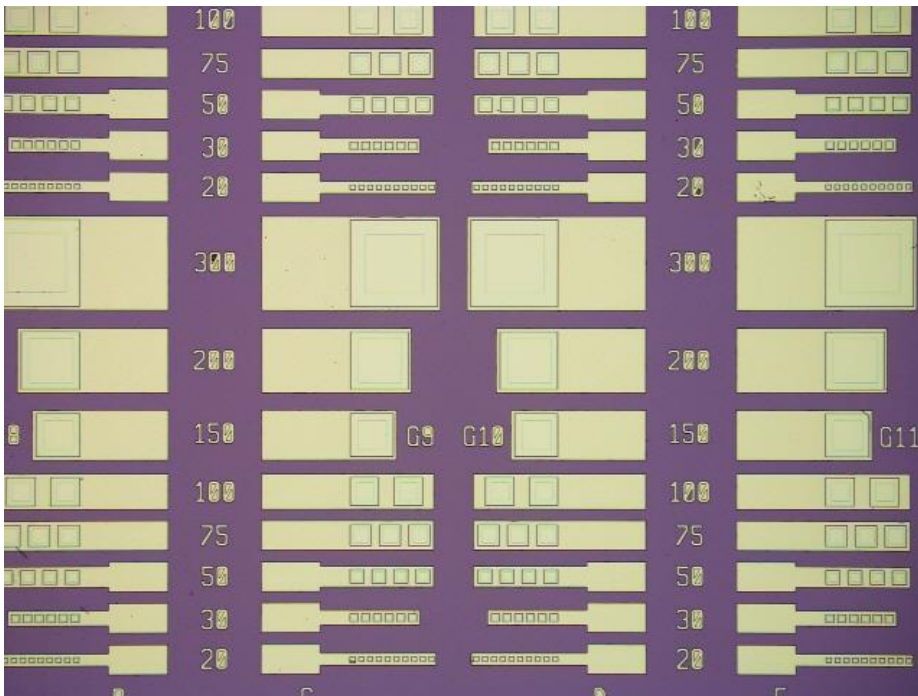
Figure 3.36: The optical image of T2, the deep etch sample with passivation.

The etch types and applied chemical operations to MAPO and SLS-TEST samples are summarized in Table 3.1.

Table 3.1: The applied chemical processes to MAPO and SLS-TEST samples.

Passivation	Sample Group	Sample ID	Shallow Etch	Deep Etch	Superlattice Etch	Citric Acid Cleaning
NO	D1N1	D1N1S7		X		X
		D1N1S8	X			X
		D1N1S9	X			
		D1N1S10		X		
	D1N2	D1N2S2		X		X
		D1N2S5		X		
		D1N2S6	X			X
		D1N2S11	X			
	D2N1	D2N1S4			X	X
		D2N1S7			X	
		D2N1S11	X			
		D2N1S12	X			X
	D2N2	D2N2S5		X		X
		D2N2S10	X			X
YES	-	T1	X			X
	-	T2		X		X

3.5   Packaging

The processed MAPO and SLS-TEST samples were mounted on an 84-pin LCC (Leadless Chip Carrier) package of Spectrum Semiconductor Materials by curing the samples at 120 °C for five minutes. The MAPO samples were grouped as two barriers etched, and two contact etched samples or two barriers etched, and two superlattice etched samples. Therefore, the comparison of barrier and contact etched MAPO

samples can be done, and the effect of the citric acid cleaning can emerge from dark current measurement. The two SLS-TEST samples were mounted separately to 84-pin LCC. Since the samples need the cryogenic temperature to suppress the thermal excitation, the 2N2222 temperature sensor was mounted on the LCC package to measure and ensure the temperature of MAPO and SLS-TEST samples with a small error margin. After the curing, the connections between the samples and the LCC pin were made via Delvotec 5610 Ball Bonder. The image of MAPO samples and SLS-TEST samples on the LCC package with wire-bonded are shown in Figure 3.37.
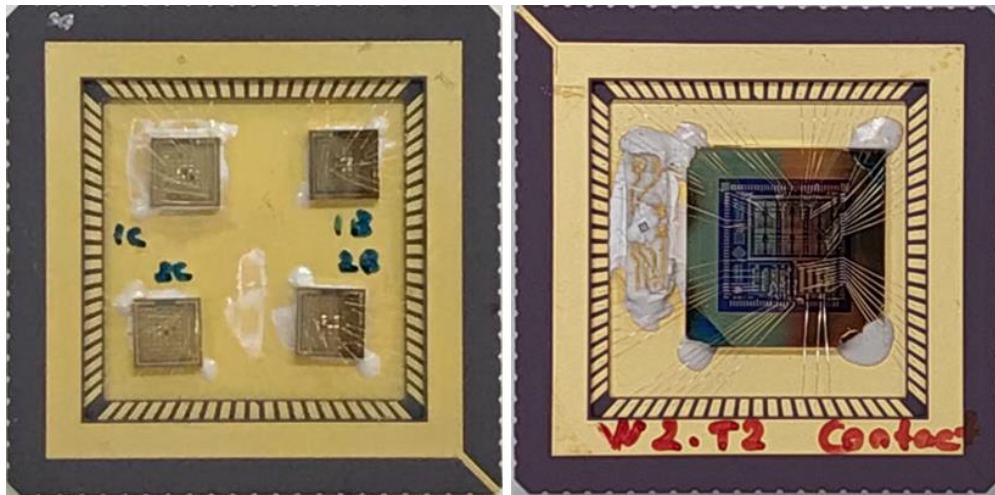
Figure 3.37: The packaged MAPO samples (left) and SLS-TEST sample (right) for measurements.

CHAPTER 4

EXPERIMENTAL RESULTS

The performance measurement setups, test steps, and results are presented in this chapter. The dark current measurements of MAPO sample groups labeled as D1N1, D1N2, D2N1, D2N2, and SLS-TEST samples labeled as T1 and T2 were completed, and the functional samples were determined. Then, the dark current changes of the pixels from these functional samples according to temperature were measured. The dynamic resistance of the functional pixels was calculated by using dark current measurement results and plotted.

The photocurrents of the optical aperture pixels were measured, and their peak responsivity values were estimated. The spectral responsivity measurements of the same pixels could not be measured due to the lack of the measurement set-up, but they were calculated using the data sent from the producing company of the nBn design.

The noise measurement was tried to optimize, but the noise measurement system could not be arisen either. Therefore, the noise of the pixels could not be measured but theoretically calculated. Since the noise could not be measured, the detectivity values of the functional pixels were calculated from the responsivity by assuming the noise values of the pixels are thermal noise limited.

4.1 Dark Current Density Measurement

The main advantage of the processed design is to suppress the SRH-based dark current mechanism with the barrier layer and reduce the diffusion current with the N-structure. Therefore, the dark current measurement system with cryostat was set up, as seen in Figure 4.1, to analyze the dark current density of the processed

samples. There are cryostat, a turbo pump, a mechanical pump, a liquid nitrogen tank, Keithley 2635B source measure unit (SMU), and LabVIEW software for I-V sweep in the dark current measurement system. The packaged samples on LCC are placed inside the cryostat in Figure 4.2. A metal shield is placed to the cryostat by facing the sample. Thus, the sample and the object that the sample is looking at will be at the same temperature, and the sample will have reached the dark condition. The packaged samples are gotten vacuum via the mechanical and the turbo pumps to minimize the environmental effects. When the vacuum level descends below mTorr, the cryostat is cooled with nitrogen by the automatic cooling system. Thus, since the backside of the LCC touches the cold finger of the cryostat, the temperature of the packaged sample on LCC will reduce to cryogenic temperatures.
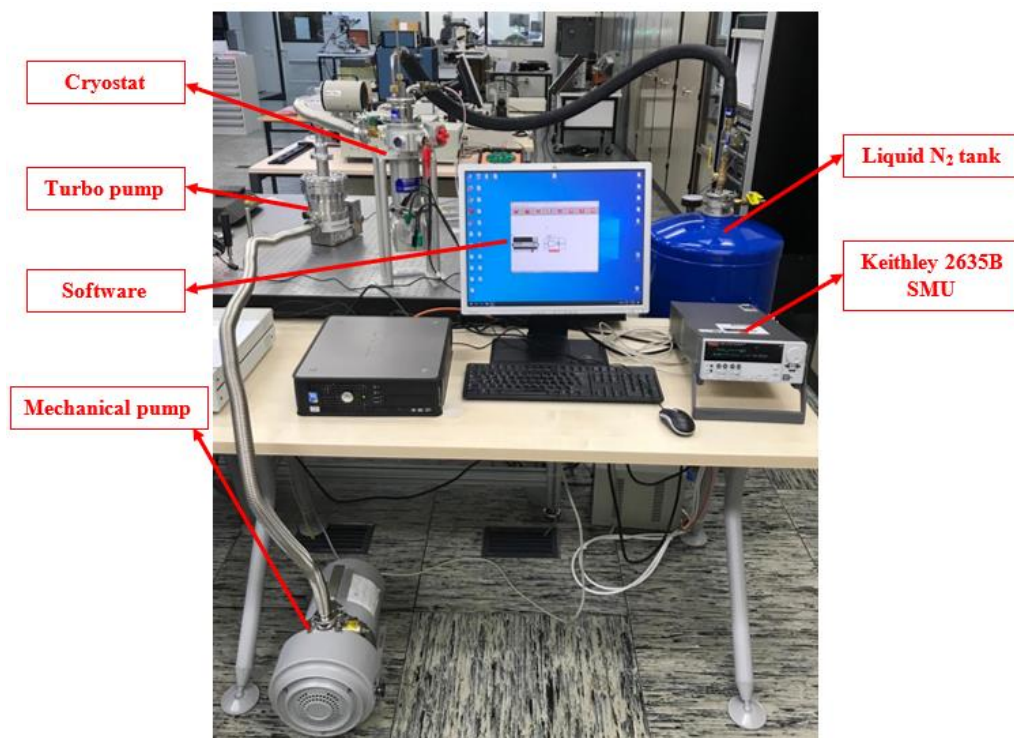
Figure 4.1: The dark current measurement system with the cryostat.

The temperature of the packaged samples on LCC was measured with the help of the 2N222 temperature sensor. When the temperature of LCC is stable, the dark current measurement was measured by sweeping voltage from -2V to +2V by 50 mV.

The dark current density-voltage graphs of the different pixel sizes from the D1N2 samples group are shown in Figure 4.3. A fluctuation emerges at the low bias voltage range. The same measurements were repeated with the other sample groups (D1N2, D2N1) to ensure the cause of the fluctuation, and similar effects were observed. Since the dark current levels to be measured are low, the connection cables between the output of the cryostat and test detectors must be covered to prevent interference. However, the used cables in the cryostat are not shielded. Therefore, the actual dark current density level of the design could not be measured accurately with the cryostat via current connection cables. In order to prove the cable problem, a shielded cable has used in the cryostat, and the interference caused by the unshielded cable has removed, as seen in Figure 4.4.
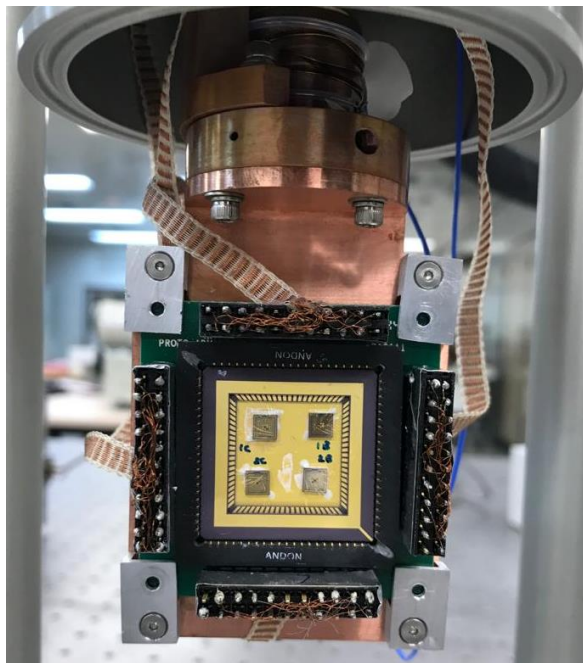
Figure 4.2: The placement of packaged samples with LCC in the cryostat.

The discussion about the dark current level of the design is not possible before fixing this unshielded cable problem. Moreover, the other measurements also can not be completed due to the same reason. Therefore, the unshielded cables inside the cryostat have been shielded carefully by opening the related part of the cryostat.
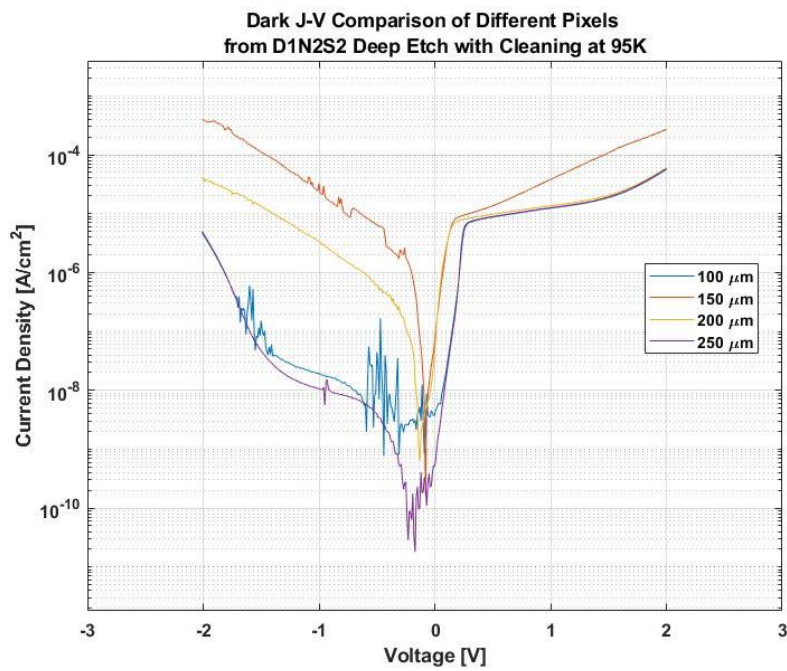
Figure 4.3: The measured J-V graph of D1N2S2 with the cryostat.
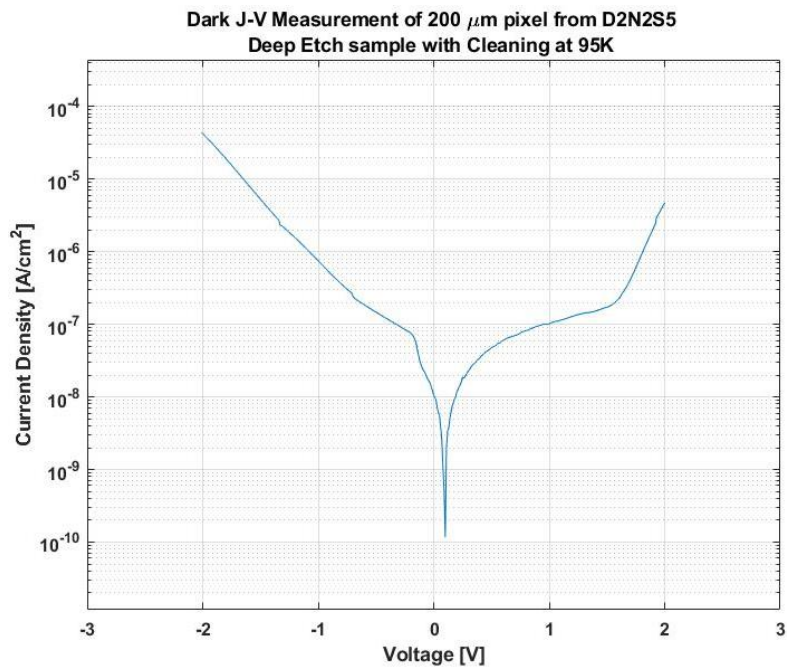
Figure 4.4: The J-V measurement result of 200 µm pixel from D2N2S5 after the
shielded cable was used in the cryostat.

The dark currents of MAPO samples were measured after the cryostat had been fixed. The results were not as expected, as seen in Figure 4.5, and all of the non-passivated sample results are the same.
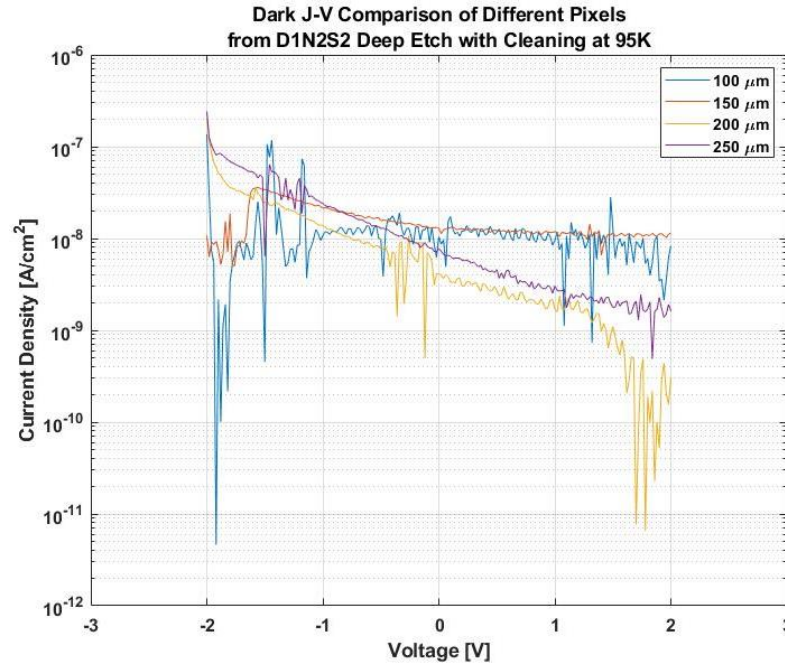
Figure 4.5: The measured J-V graph of D1N2S2 after the cryostat had been fixed.

MAPO samples were fabricated almost eight months ago without the passivation process, and they were subjected to multiple cooling-heating operations while trying to find out the cryostat problems. Therefore, these two reasons can be the primary factors damaging the MAPO samples.

The dark current measurement of SLS-TEST samples labeled as T1 and T2 were completed with the same system. The temperature of the T1 and T2 was measured at 95K via the 2N2222 temperature sensor during the dark current measurement. The change in the dark current density according to the voltage of the samples can be seen in Figure 4.6. The current density level of the shallow etch sample was not changed within a certain voltage range since the minimum current level that Keithley 2635 SMU can measure is 10^{-12} A. Therefore, the dark current density-voltage results of T1 and T2 were compared at 160K temperature, where the device limit is

appropriate. Moreover, the zero-bias resistance of the samples is the crucial parameter in evaluating the passivation quality. Since the structure is bias-selectable for dual-color, the dynamic resistance also should be investigated. The dark current density and the dynamic resistance of T1 and T2 were plotted in Figure 4.7.
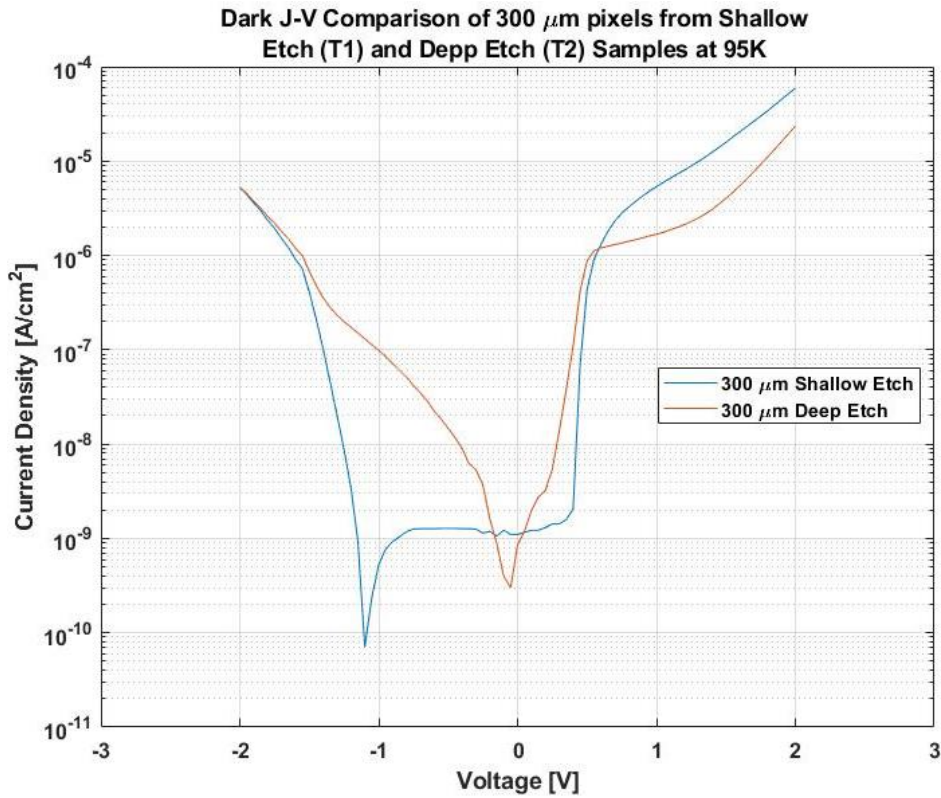
Figure 4.6: Dark J-V comparison of 300 µm pixels from T1 and T2 at 95K.

The lowest dark current level of the measured pixel should be reached at 0 V if the temperature of the sample and the object that is looking at are equal. However, the measured pixels from shallow and deep etch samples have reached the lowest current density level at a higher voltage value than 0 V, as seen in Figure 4.7. That means the temperature of the metal shield is higher than the sample temperature. If the dark current density level of the samples were compared, the pixel with shallow etch has a much lower current density level since the etched mesa sidewalls ratio is lower for the shallow etch sample. The dark current density of T1 and T2 is better than the p-i-n structure in the literature, as expected, since the SRH-based dark current

84

mechanism is suppressed with the nBn structure. When the dark current density results are compared with some nBn structures [95] in literature for 160 K, both shallow etch and deep etch samples have better dark current results.
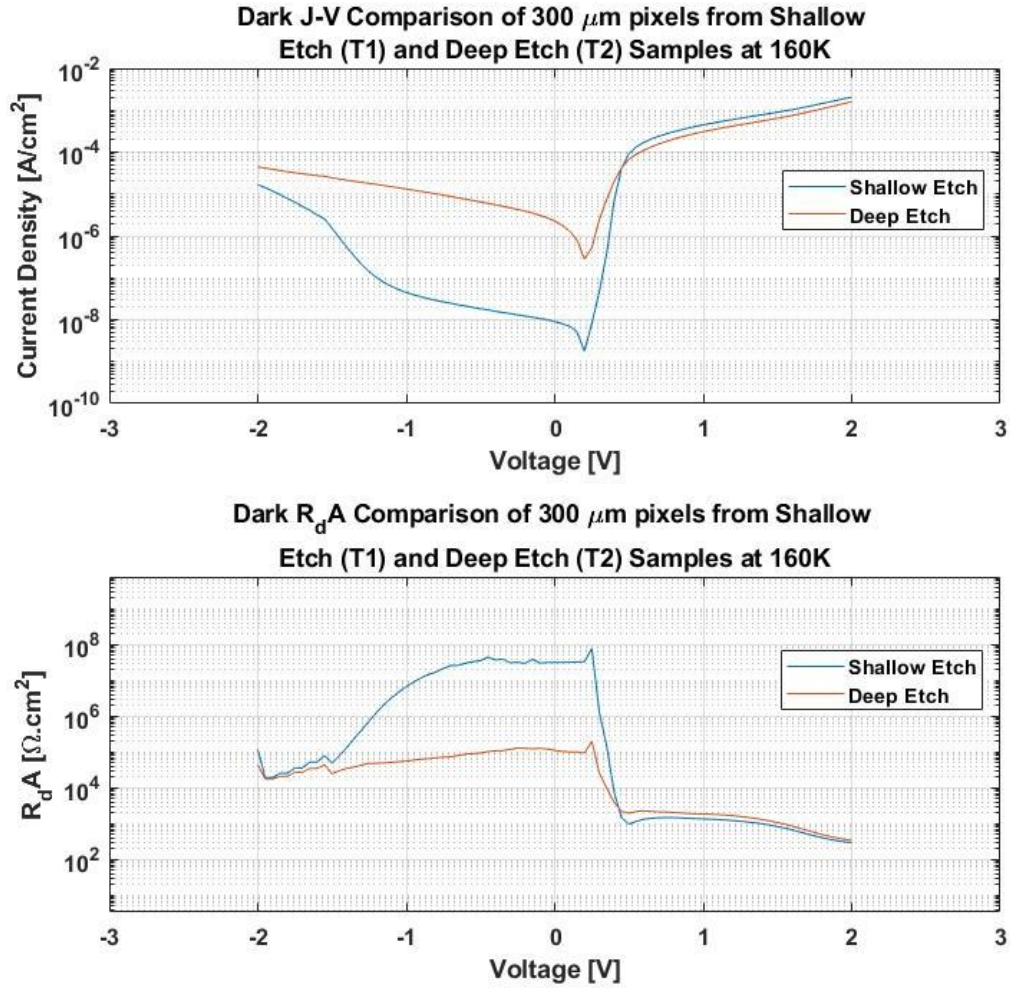
Figure 4.7: Dark J-V and $R_d.A$ comparison of 300 µm pixels from T1 and T2 at 160K.

The zero-bias resistance values of the samples were calculated with the equation shown below.

$$R_0A = \left(\frac{dI}{dV}\right)_{V=0}^{-1} \times A_{det} = \left(\frac{I_{V=0.3} - I_{V=0.2}}{0.3 - 0.2}\right)^{-1} \times A_{det} \qquad (4.1)$$

The lowest dark current density of T1 and T2 was reached at 0.25 V due to the temperature difference between the sample and the metal shield faced to the sample. Therefore, the resistance values of the samples at 0.25 V were calculated as in Equation 4.1 and R_0A values of T1 and T2 were found as 7.86×10^7 and 2.02×10^5, respectively. The detector area (A_{det}) is used to remove the effect of the pixel size.

The dynamic resistance of the samples for each voltage value can also be calculated using Equation 4.1, and they are shown in Figure 4.7. Even though the same passivation process was applied to T1 and T2, the dynamic resistance results of T1 have given better results, such as the dark current density of T1 than T2, because of the advantages of the shallow etch.
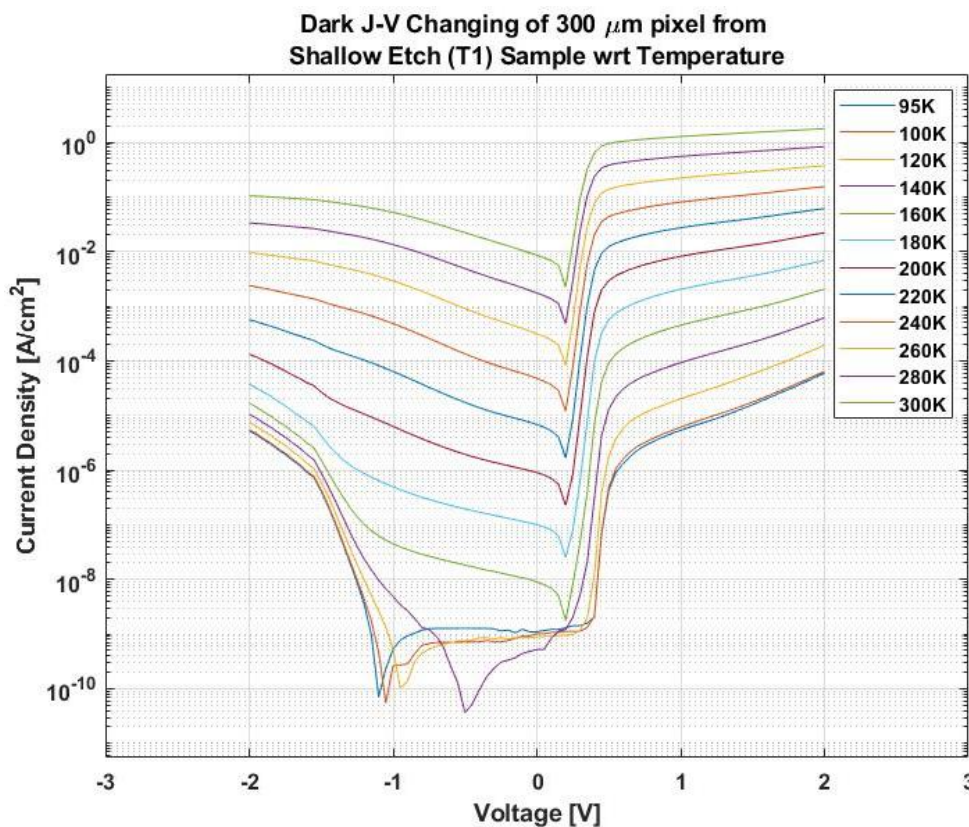
Figure 4.8: The changing of the dark current density with temperature for shallow etch (T1) sample.
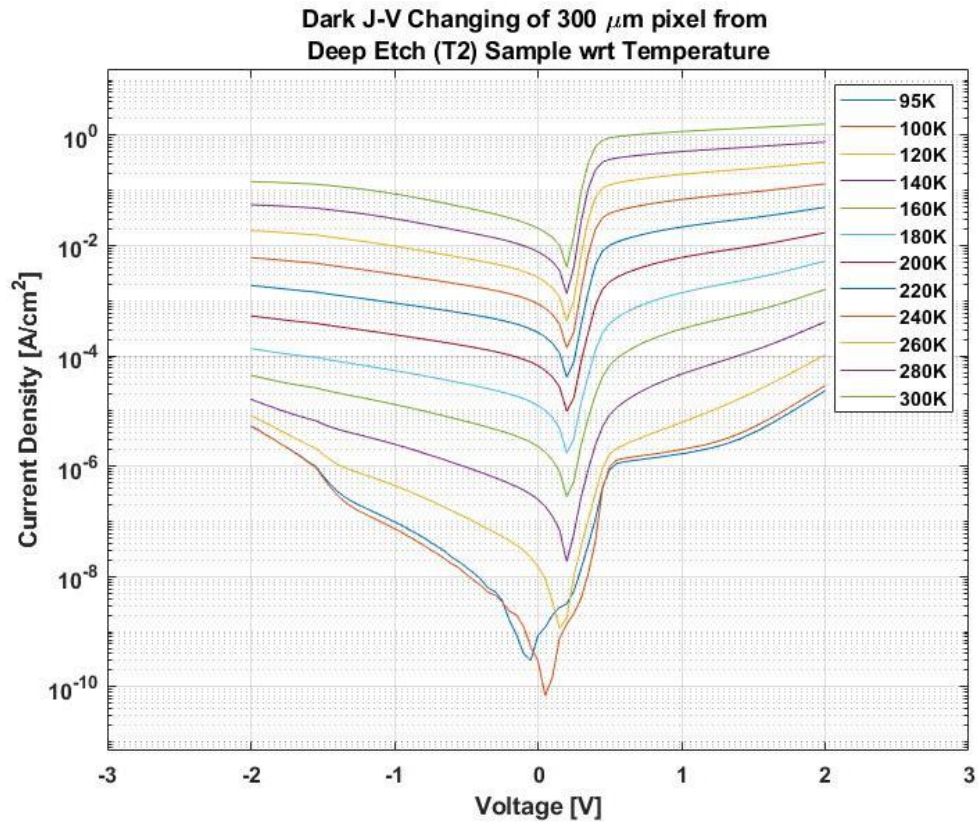
Figure 4.9: The changing of the dark current density with temperature for deep etch (T2) sample.

The temperature of the T1 and T2 was swept from 95K to 300K, and the change of the dark current density according to the temperature was presented in Figure 4.8 and Figure 4.9 for T1 and T2, respectively. The dominant dark current mechanism is changed at higher temperatures; therefore, the dark current density of T1 and T2 are almost equal at 300K. At lower temperature levels (T<140 K), the surface leakage currents are the dominant than the diffusion and the G-R currents. The advantages of the shallow etch sample has disappeared at higher temperatures due to the lateral diffusion mechanism of the shallow etch sample, and the dark current density levels of T1 and T2 have become almost equal, as seen in Figure 4.8 and Figure 4.9. Both samples had better results than some studies in the literature when the dark current density levels of T1 and T2 were compared with these studies according to the temperatures [95] [96] [97].

4.2   Optical Measurement

The optical measurement is a critical step to investigate the responsivity and the quantum efficiency of the structure. The optical measurement is divided into two sections spectral responsivity measurement and peak responsivity measurement. The spectral responsivity measurement should be done with FTIR (Fourier Transform Infrared) spectroscopy or an optical system consisting of the monochromator and the reference detector. In blackbody responsivity measurement, the calibrated blackbody is used.

The spectral responsivity measurement of T1 and T2 could not be completed due to the lack of the measurement system. Instead of this, the spectral responsivity result sent from the manufacturer company of the structure was used for optic analysis. The spectral responsivity plot of the structure with respect to the wavelength can be seen in Figure 4.10.
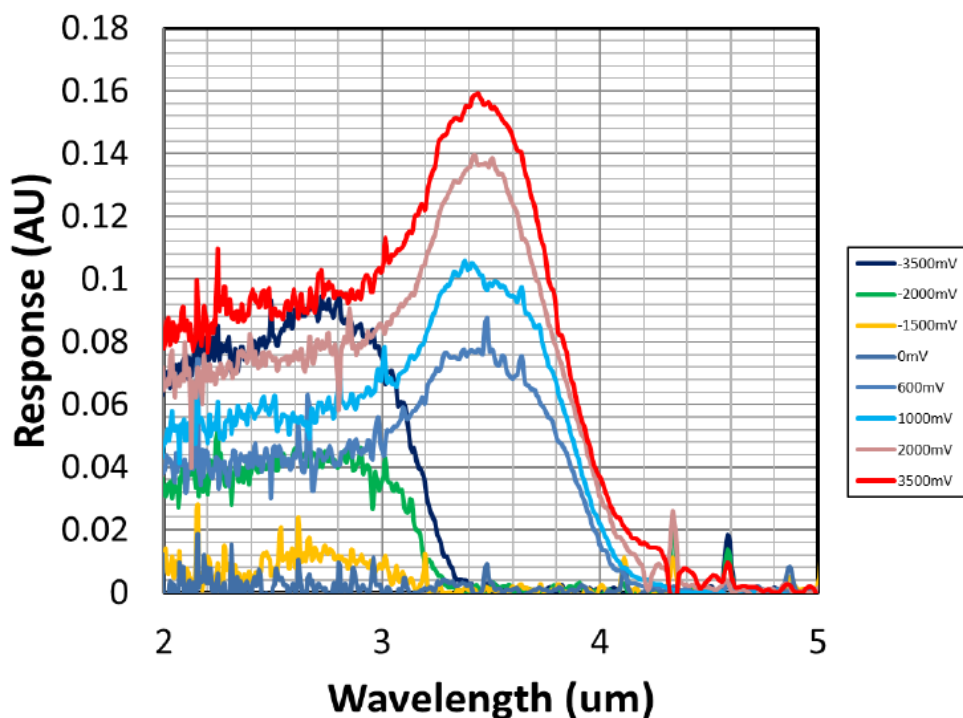
Figure 4.10: The spectral responsivity-wavelength plot of the nBn structure with respect to the bias regime.

The nBn structure is bias-selectable to operate dual-color at MWIR. When the structure is in reverse bias, the detection will occur between 3-4 µm (red channel). In the opposite case, when the structure with forward bias, the structure will detect between 4-5 µm (blue channel), as seen in Figure 4.10. However, the detector gave a response between 3-4 µm at $2\,V$ in forward bias. Therefore, the analysis will be done according to this information.

In order to make the optical analysis, the maximum spectral responsivity values that the structure for the red channel was chosen from Figure 4.10 as 3.6 µm at forward bias. Therefore, the blackbody temperatures used in blackbody responsivity measurement were estimated as 800 K using Equation 1.6.

The Newport 67030 cavity blackbody was placed facing the back of the sample to make detection for both channels, and the distance between them was set as twenty cm for the blackbody responsivity measurement. The samples were gotten vacuum and cooled to 160K. The photocurrent measurements were completed between $-2\,V$ and $2\,V$ when the back-side of the samples was looked at to 800 K.

The results can be seen in Figure 4.11 and Figure 4.12 for T1 and T2, respectively. The peak photocurrent ratio is achieved for the red channel at $-1.2\,V$ and the blue channel at $0.5\,V$, but since the spectral responsivity values of the structure are given at $2\,V$ in Figure 4.10, the photocurrent values of the T1 and T2 were used at this voltage.
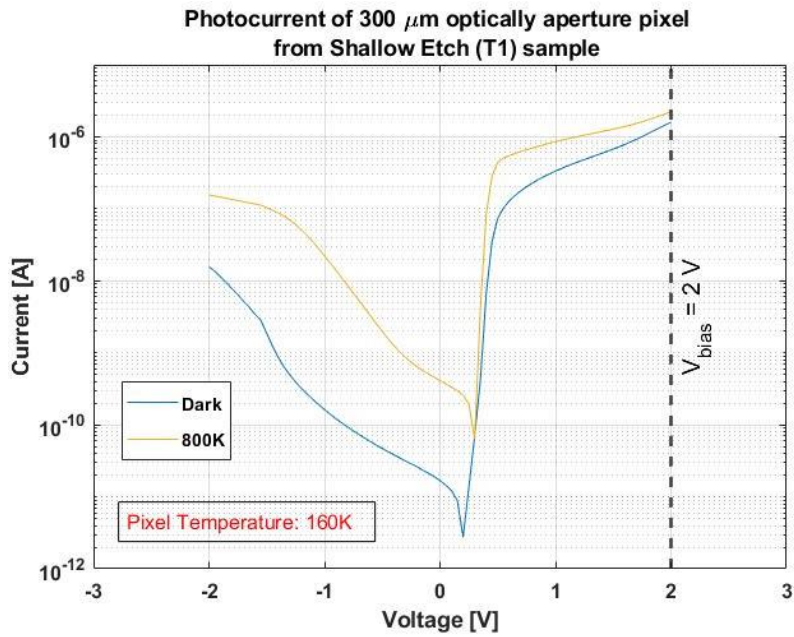
Figure 4.11: Photocurrent of 300 µm optically aperture pixel from T1, the sample temperature is 160 K.
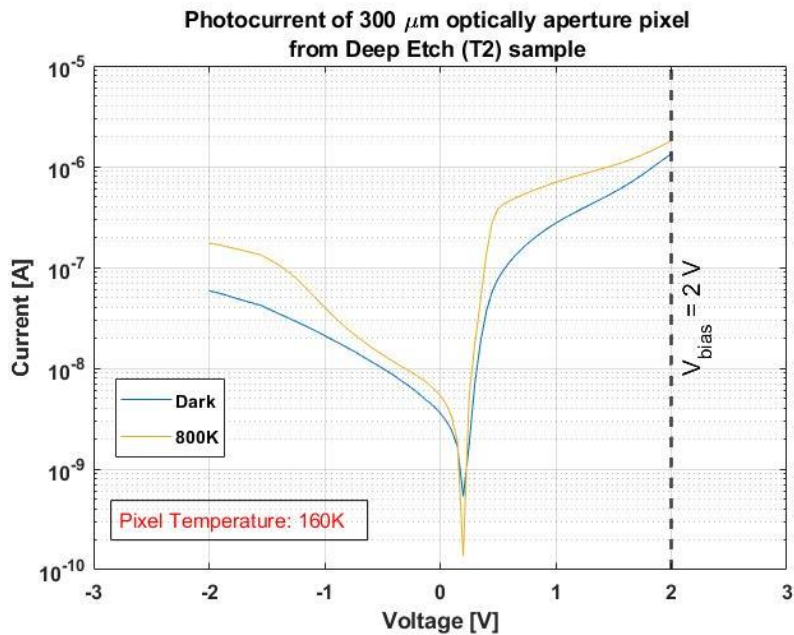
Figure 4.12: Photocurrent of 300 µm optically aperture pixel from T2, the sample temperature is 160 K.

The responsivity of the detector is calculated by using Equation 1.10. This equation can be derived as:

$$I_{photocurrent} = R \times \phi \tag{4.2}$$

Equation 4.2 becomes the formula below when the variables are put in:

$$I_{photocurrent} = \int_0^\infty R_{peak} \times R(\lambda) \times \phi(\lambda)\, d\lambda \tag{4.3}$$

where R_{peak} is the peak responsivity, $R(\lambda)$ is the normalized spectral responsivity, and, $\phi(\lambda)$ corresponds to incident power on the detector. The $\phi(\lambda)$ is calculated as:

$$\phi(\lambda) = \int_0^\infty \frac{M(\lambda, T_{BB})}{\pi} \times A_{BB} \times \frac{A_{det}}{d^2} \times W(\lambda) \times F(\lambda) d\lambda \tag{4.4}$$

where $M(\lambda, T_{BB})$ is spectral radiant exitance of the blackbody at T_{BB} temperature, A_{BB} is the aperture area of the blackbody, A_{det} is the pixel area, d is the distance between the blackbody and the sample, $W(\lambda)$ is the transmission of the window using on the cryostat, and $F(\lambda)$ is the transmission of the filter placed in front of the blackbody aperture. The only unknown variable in this equation which is R_{peak}, can be calculated using the measured and estimated variables for the optical aperture pixels from T1 and T2.

The peak responsivity values of the pixels were calculated as 1.5 A/W and 0.46 A/W for T1 and T2 at 2 V forward bias voltage. The responsivity values of the samples were estimated by multiplying the peak responsivity values with the normalized spectral responsivity, which is taken from Figure 4.10, and the results were plotted in Figure 4.13. Moreover, the quantum efficiencies (QE) of the samples were calculated by using Equation 1.12 and shown in Figure 4.13. The external QEs of the samples were found as 50% and 15% for T1 and T2, respectively, at the peak wavelength.
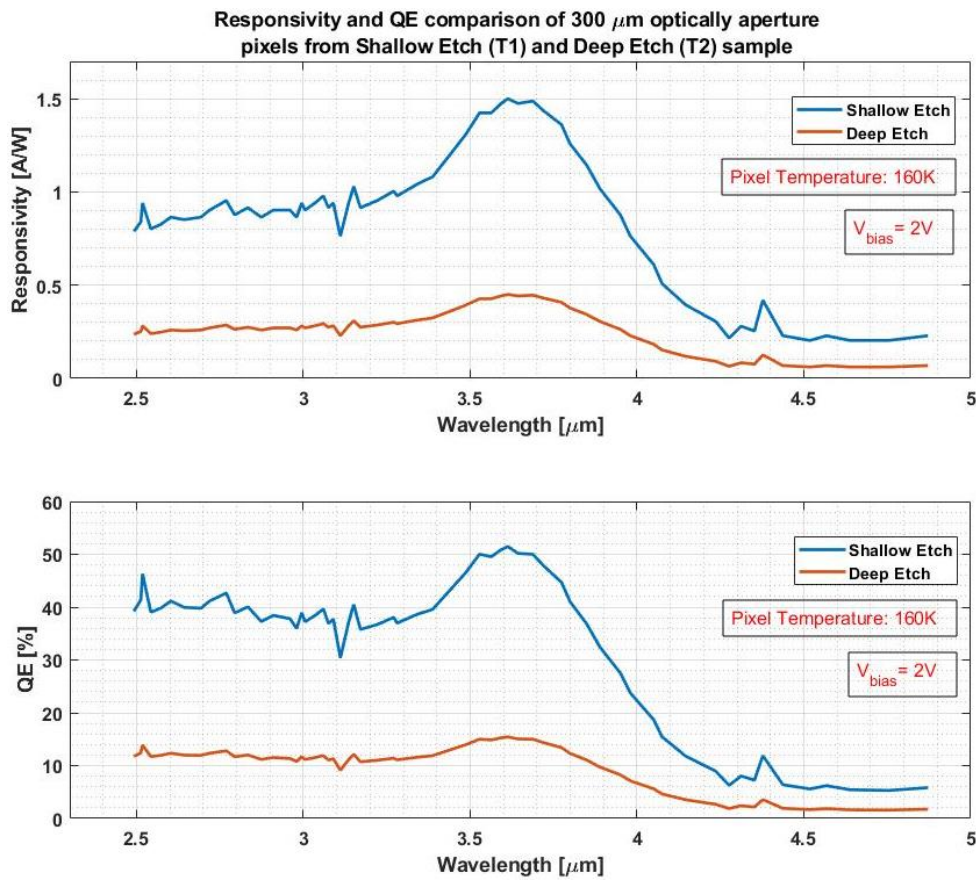
Figure 4.13: Responsivity and QE comparison of pixels from Shallow Etch (T1) and Deep Etch (T2) samples.

The advantages of the shallow etch on the current mechanism are also seen in the responsivity and QE. However, the spectral responsivities and the QEs of T1 and T2 are generally lower than the nBn ones studied in the literature at the peak wavelength, unlike the dark current levels. The reason for that can be explained by the spectral responsivity data obtained from the document. The spectral responsivity values could not be measured due to the device problems, and the real spectral responsivity data could not be obtained for the voltage values, which is the photocurrents of the samples were maximum. The responsivity and the QE results can be better with the real data taken by the spectral responsivity measurement.

4.3   Specific Detectivity (D*) Measurement

The specific detectivity $(D*)$ of the pixels of T1 and T2 were calculated by using Equation 1.16. In this equation, R is the responsivity throughout the wavelength, A_d is the detector area, and i_{noise} is the thermal noise of the sample. Since the noise of the system could not be measured, the thermal noise was estimated as theoretically by using Equation 1.13 via the dynamic resistance value at $2\,V$ due to the responsivity of the pixels found for the same bias voltage value. The specific detectivity values of the T1 and T2 were calculated as thermal noise limited and plotted in Figure 4.14.
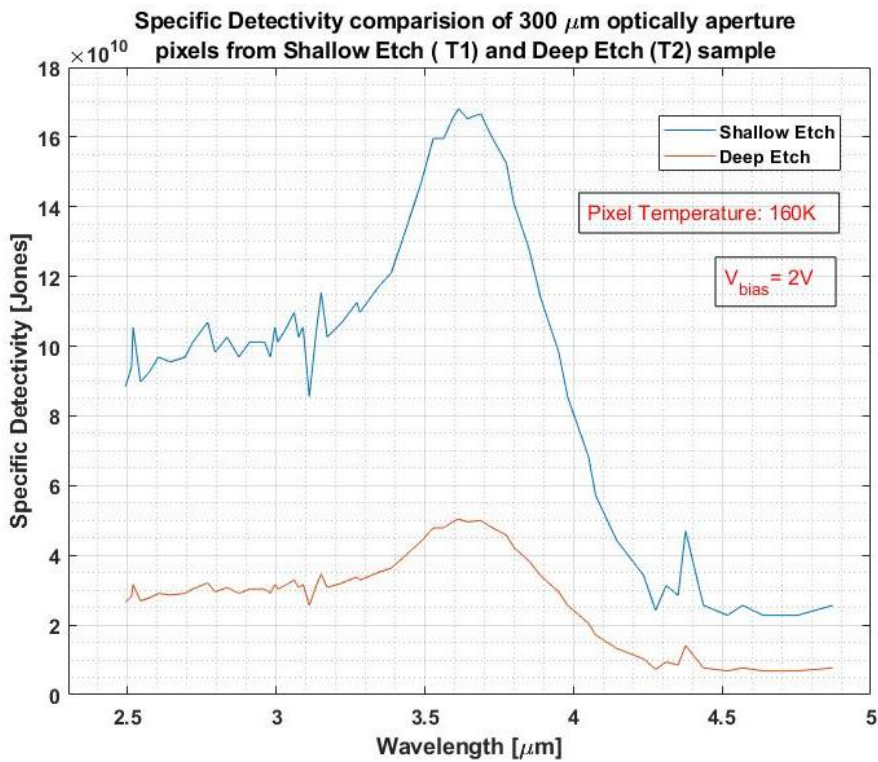
Figure 4.14: Specific detectivity $(D*)$ comparison of the pixels from T1 and T2.

4.4   Noise Measurement

The noise measurement system is shown in Figure 4.15. There are Stanford Research System SR570 Low Noise Amplifier, Keysight 35670A Dynamic Signal Analyzer, a Faraday cage (black), a small Faraday cage (for optimization measurement with resistor), and software for system control. The sample connected to the input of SR570 will be biased with the appropriate voltage, and then the offset of the SR570 will be set to minimize the external noise. The pure sample noise will be amplified, and the amplified noise at the output of SR570 will be plotted with respect to the frequency via DSA (Digital Signal Analyzer).
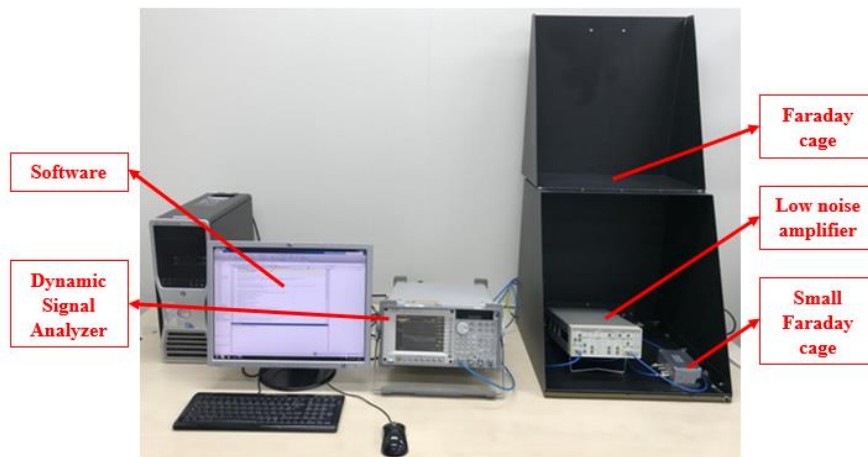
Figure 4.15: Photon noise measurement system.

In order to make sure the system is working correctly, a noise measurement of a 45 kΩ metal resistor was executed with Bolometer Noise setup, which is functional, and Photon Noise setup. The dominant noise mechanism of resistors should be thermal noise at high frequency, and the measured noise plots and the theoretical noise plots have to be overlapped for the chosen resistor, as shown in Figure 4.16 [98]. However, the noise measurement result of Photon Noise setup has not supported this theory, as seen in Figure 4.17.
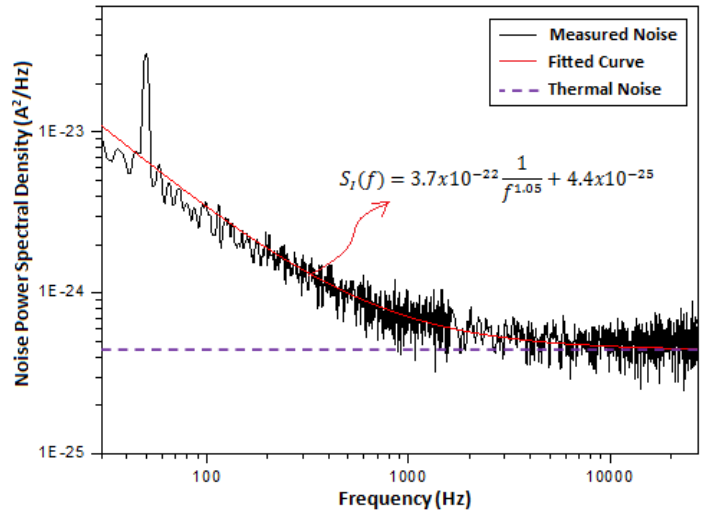
Figure 4.16: Noise measurement result of 75 kΩ metal resistor from Ph.D. thesis of

Özgecan Dervişoğlu [98].
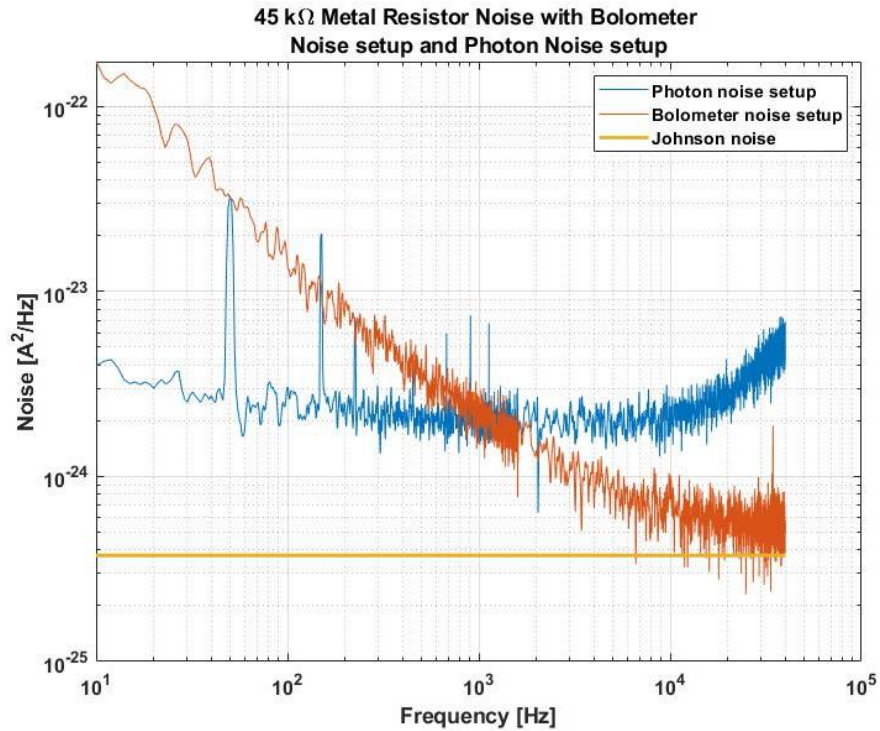
Figure 4.17: Noise spectrum of 45 kΩ metal resistor with respect to frequency for

Bolometer Noise setup and Photon Noise setup.

There is something to interfere with Photon Noise setup and increases the noise of the sample being measured, as seen in Figure 4.17. Although several improvements have been tried, this problem could not be solved. For this reason, the noise values of pixels from T1 and T2 could not be measured but calculated as theoretically with the help of Equations 1.13 and 1.14. The calculated shot noise and thermal noise values should be the same with the shot and thermal noise values to be measured at high frequencies. In order to calculate the thermal noise of the pixels, their dynamic resistance values of them at $2\,V$ voltage level should be used since the samples have photoresponsivity at $2\,V$ for MWIR. The calculated thermal noise of the $300\,\mu m$ pixels from the samples are $1.63 \times 10^{-13}\,A/\sqrt{Hz}$ and $1.51 \times 10^{-13}\,A/\sqrt{Hz}$ at the dark condition and 160 K detector temperature for T1 and T2, respectively.

The estimated shot noise values of the same pixels at $2\,V$ voltage bias were found as $7.70 \times 10^{-13}\,A/\sqrt{Hz}$ and $6.79 \times 10^{-13}\,A/\sqrt{Hz}$ at the dark condition and 160 K detector temperature for T1 and T2, respectively.

The shot noise and the thermal noise were calculated by using the measured current values and the measured zero-bias resistance without the Faraday cage, and while the turbo and the mechanical pumps were active. The calculated results are not bad according to the studied in the literature, but the measured noise values will be better than the calculated results with the appropriate noise measurement setup.

CHAPTER 5

CONCLUSION AND FUTURE WORK

The thesis study presents the fabrication and characterization steps of a new design nBn superlattice detector. The absorption layers of nBn superlattice are designed with n-doped InAs/AlSb/GaSb N-Structure superlattice semiconductors. Thus, it was desired to enhance the quantum efficiency and also to reduce the diffusion-based dark current level. A wide energy-band ternary semiconductor, $Al_xGa_{1-x}Sb$, is used as a barrier layer to suppress the SRH-based dark current and prevent the thermally-generated electron carriers from affecting the photogenerated current.

In Chapter I of the thesis, the fundamental information of infrared technology was presented. The principles of the detection, the detector types, and the figure of merits for photon detectors were explained.

In Chapter II, the history of the Type-II Superlattice technology was expressed. The operation principles and the properties that provide advantages of SL were discussed. The structure type of the SL detector and the recent technologies of SL detectors were demonstrated.

In Chapter III, the nBn structure will be processed was explained. The fabrication steps of the produced samples and the different processes applied to samples were discussed. MAPO samples that have different etch depths without a passivation layer and SLS-TEST samples that have different etch depths with the passivation layer were fabricated. These samples were packaged with 84-pin LCC and made ready for characterization.

In Chapter IV, the experimental measurement systems were demonstrated, and the characterization of the processed samples was completed. The dark current density vs. voltage measurement was done for MAPO samples, but due to the unshielded cables used in the cryostat, the experimental results were acquired with noisy.

Therefore, these unshielded cables were shielded, and MAPO samples were measured again. However, the dark current density results of MAPO samples were not as expected. It was thought that MAPO samples were broken due to the fact that they were produced long ago without passivation and subjected to multiple cooling-heating operations while trying to find out the cryostat problems. For this reason, SLS-TEST samples labeled as T1 (shallow etch) and T2 (deep etch) were used for characterization. The dark current density vs. voltage and temperature-dependent dark current density vs. voltage measurements of different sizes of pixels were done. The dark current density levels of these pixels could not be measured properly at the temperature level lower than 160 K due to the limit of the device since Keithley 2636B SMU cannot measure the current level smaller than 10^{-12} A. Therefore, the dark current analysis of T1 and T2 was completed at 160 K and higher sample temperature.

The dark current density levels of 300 µm pixels from the shallow etch sample is better than the deep etch sample, as expected, thanks to the un-etched mesa sidewalls. The dark current density results of T1 and T2 are better than p-i-n structure superlattice studies in the literature, thanks to the nBn design. Moreover, these dark current density levels are also better than some nBn studies in the literature. The zero-bias resistance values of T1 and T2 were measured at $0.25\,V$ instead of $0\,V$ due to the temperature difference between the sample and the metal shield faced to the sample, and these values are also one of the better results between the nBn studies in the literature.

The spectral responsivity measurement could not be done due to the lack of equipment. Instead of this, the spectral responsivity measurement results for different voltage bias values sent from the manufacturer company were used. As known, the nBn structure has operated at dual-color according to the bias-selectable. For reverse voltage values, the detector will be functional between 3-4 µm (red channel). In the opposite situation, when the detector is biased with forward bias values, it will be active between 4-5 µm (blue channel). However, in the spectral responsivity document sent from the manufacturer company, the peak wavelength is

3.6 µm for 2 V at forward bias. Even though the maximum photocurrent values of T1 and T2 were $-1.2\,V$ and $0.5\,V$ for the red channel and the blue channel, respectively, the responsivity, the QE, and the detectivity characterizations of the samples were analyzed for 3.6 µm peak wavelength at $2\,V$.

The blackbody responsivity measurements of 300 µm optically aperture pixels from T1 and T2 were completed using cavity blackbody at 800 K for 3.6 µm peak wavelength. The peak responsivity values of the detectors from T1 and T2 were calculated as $1.5\,A/W$ and $0.46\,A/W$ at 3.6 µm peak wavelength, respectively, using photocurrent values of detectors from T1 and T2 at $2\,V$ voltage, and the spectral responsivity data from the manufacturer document. The external QE values of the samples were estimated as 50% and 15%, respectively. The specific detectivity values were found as $1.7 \times 10^{11}\,Jones$ and $5 \times 10^{10}\,Jones$. The responsivity, the QE efficiency, and the detectivity values of the samples are lower than the nBn studies in the literature, unlike the dark current density level. These values were estimated by using the spectral responsivity document sent from the manufacturer company. If the spectral responsivity of the samples can be measured with the appropriate setup and the appropriate voltage values which have maximum photocurrent, these results will be better than the present ones.

The dark noise measurement of T1 and T2 could not be completed due to measurement setup problems. The shot noise and the thermal noise of 300 µm pixels were calculated theoretically. The thermal noise values were estimated as $1.63 \times 10^{-13}\,A/\sqrt{Hz}$ and $1.51 \times 10^{-13}\,A/\sqrt{Hz}$ for T1 and T2, respectively. The calculated shot noise values of T1 and T2 are $7.70 \times 10^{-13}\,A/\sqrt{Hz}$ and $6.79 \times 10^{-13}\,A/\sqrt{Hz}$, respectively. Even though the calculated noise values are promising, these results may not be suitable for comparison with the literature since the used zero-bias and current values were measured without the Faraday cage while the mechanical and turbo pumps were on.

The designed nBn structure is a promising superlattice detector even though all characterizations of performance parameters were not completed as supposed to be done. The cut-off wavelengths for dual-color in MWIR are not as desired, a cross-talk between the channels exists, and large bias voltage levels are required for photoresponsivity in MWIR, according to the manufacturer data. A more detailed analysis can be made to eliminate the deficiencies in the structure and fabrication when problems and the missing parts of the measurement systems solve. Thus, the FPAs with high QE and high yield can be produced with this structure as future work.

REFERENCES

[1]   E. F. J. Ring and K. Ammer, "Infrared thermal imaging in medicine," *Physiological Measurement*, vol. 33, no. 3, pp. R33–R46, Mar. 2012, doi: 10.1088/0967-3334/33/3/R33.

[2]   D. L. Mangus, A. Sharda, and N. Zhang, "Development and evaluation of thermal infrared imaging system for high spatial and temporal resolution crop water stress monitoring of corn within a greenhouse," *Computers and Electronics in Agriculture*, vol. 121, pp. 149–159, Feb. 2016, doi: 10.1016/J.COMPAG.2015.12.007.

[3]   A. Rogalski, "New material systems for third generation infrared photodetectors," *Opto-electronics Review*, vol. 16, no. 4, pp. 458–482, 2008, doi: 10.2478/S11772-008-0047-7.

[4]   A. Rogalski, J. Antoszewski, and L. Faraone, "Third-generation infrared photodetector arrays," *Journal of Applied Physics*, vol. 105, no. 9, p. 091101, May 2009, doi: 10.1063/1.3099572.

[5]   E. Barr, "The Infrared Pioneers-III. Samuel Pierpont Langley," *Infrared Physics*, vol. 3, pp. 195–206, 1963.

[6]   T. Case, "Notes on the Change of Resistance of Certain Substances in Light," *Physical Review*, vol. 9, no. 4, pp. 305–310, 1917.

[7]   L. Esaki and R. Tsu, "Superlattice and Negative Differential Conductivity in Semiconductors," *IBM J. Res. Dev*, vol. 14, pp. 61–65, 1970.

[8]   D. Z. Ting *et al.*, "Advances in III-V semiconductor infrared absorbers and detectors," *Infrared Physics & Technology*, vol. 97, Mar. 2019, doi: 10.1016/j.infrared.2018.12.034.

[9]   H. Mohseni, V. I. Litvinov, and M. Razeghi, "Interface-induced suppression of the Auger recombination in type-II InAs/GaSb superlattices".

[10]   C. Besikci, "Infrared Devices and Systems Lecture Notes." Ankara, 2020.

[11]   "BlackbodySpectrum_2.png (800×580)."
https://www.sun.org/uploads/images/BlackbodySpectrum_2.png (accessed
Oct. 30, 2021).

[12]   Y. Arslan, "Large Format Dual-Band Quantum Well Infrared Photodetector
Focal Plane Arrays," Dissertation for the Degree of Master of Science, Middle
East Technical University, 2009.

[13]   "atmospheric_transmittance.png (981×535)."
https://www.usna.edu/Users/oceano/pguth/website/so431/quiz/atmospheric_
transmittance.png (accessed Dec. 02, 2021).

[14]   D. P. Marc Hansen, D. S. Malchow, and M. P. Hansen, "Overview of SWIR
detectors, cameras, and applications," *https://doi.org/10.1117/12.777776*,
vol. 6939, no. 17, pp. 94–104, Mar. 2008, doi: 10.1117/12.777776.

[15]   P.-Y. Delaunay, B. Z. Nosho, A. R. Gurga, S. Terterian, and R. D. Rajavel,
"Advances in III-V based dual-band MWIR/LWIR FPAs at HRL,"
https://doi.org/10.1117/12.2266278, vol. 10177, no. 16, pp. 156–167, May
2017, doi: 10.1117/12.2266278.

[16]   M. Kaldırım, "Dual and Single Color Mid-Wavelength Infrared Quantum
Well Photodetectors," Dissertation for the Degree of Master of Science,
Middle East Technical University, 2008.

[17]   A. Rogalski, *Infrared Detectors*, Second Ed. Boca Raton: CRC Press, 2011.

[18]   O. Temel, "Molecular Beam Epitaxy Growth of InP/InGaAs Structures for
Short Wavelength Infrared Photodetectors," Dissertation for the Degree of
Master of Science, Middle East Technical University, 2014.

[19]   A. Rogalski, M. Kopytko, and P. Martyniuk, "Infrared Detector
Characterization," in *Antimonide-based Infrared Detectors: A New
Perspective*, SPIE, 2018. doi: 10.1117/3.2278814.ch1.

[20] A. Rogalski, "Progress in focal plane array technologies," *Progress in Quantum Electronics*, vol. 36, no. 2–3, pp. 342–473, Mar. 2012, doi: 10.1016/J.PQUANTELEC.2012.07.001.

[21] E. A. Plis, "InAs/GaSb Type-II Superlattice Detectors," *Advances in Electronics*, vol. 2014, pp. 1–12, Apr. 2014, doi: 10.1155/2014/246769.

[22] V. M. Cowan, C. P. Morath, S. Myers, N. Gautam, and S. Krishna, "Low-temperature noise measurements of an InAs/GaSb-based nBn MWIR detector," May 2011, p. 801210. doi: 10.1117/12.884808.

[23] S. Özer, "InSb and InAsSb Infrared Photodiodes on Alternative Substrates and InP/InGaAs Quantum Well Infrared Photodetectors: Pixel And Focal Plane Array Performance," Dissertation for the Degree of Doctor of Philosophy, Middle East Technical University, 2005.

[24] X. Li *et al.*, "Investigation of dark current mechanisms on type-II InAs/GaSb superlattice very long wavelength infrared detectors," *Journal of Physics D: Applied Physics*, vol. 49, no. 16, p. 165105, Apr. 2016, doi: 10.1088/0022-3727/49/16/165105.

[25] E. Plis *et al.*, "Type II InAs/GaSb strain layer superlattice detectors with p-on-n polarity," *Applied Physics Letters*, vol. 91, no. 13, p. 133512, Sep. 2007, doi: 10.1063/1.2790078.

[26] H. Mohseni, V. Litvinov, and M. Razeghi, "Interface-induced suppression of the Auger recombination in type-II InAs/GaSb superlattices," *Physical Review B*, vol. 58, no. 23, p. 15378, Dec. 1998, doi: 10.1103/PhysRevB.58.15378.

[27] G. A. Sai-Halasz, R. Tsu, and L. Esaki, "A new semiconductor superlattice," *Applied Physics Letters*, vol. 30, no. 12, p. 651, Aug. 2008, doi: 10.1063/1.89273.

103

[28] D. , S. Gunapala, R. , D. Rhiger, and Jagadish Chennupati, "Advances in Infrared Photodetectors," *Semiconductors and Semimetals*, vol. 84, pp. 195– 242, 2011.

[29] W. R. Frensley and H. Kroemer, "Theory of the energy-band lineup at an abrupt semiconductor heterojunction," *Physical Review B*, vol. 16, no. 6, pp. 2642–2652, Sep. 1977, doi: 10.1103/PhysRevB.16.2642.

[30] W. A. Harrison, "Elementary theory of heterojunctions," *Journal of Vacuum Science and Technology*, vol. 14, no. 4, pp. 1016–1021, Jul. 1977, doi: 10.1116/1.569312.

[31] G. A. Sai-Halasz, L. Esaki, and W. A. Harrison, "InAs-GaSb superlattice energy structure and its semiconductor-semimetal transition," *Physical Review B*, vol. 18, no. 6, p. 2812, Sep. 1978, doi: 10.1103/PhysRevB.18.2812.

[32] G. A. Sai-Halasz, L. L. Chang, J.-M. Welter, C.-A. Chang, and L. Esaki, "Optical absorption of In1−xGaxAs/GaSb1−yAsy superlattices," *Solid State Communications*, vol. 27, no. 10, pp. 935–937, Sep. 1978, doi: 10.1016/0038-1098(78)91010-4.

[33] J. N. Schulman and T. C. McGill, "The CdTe/HgTe superlattice: Proposal for a new infrared material," *Applied Physics Letters*, vol. 34, no. 10, pp. 663– 665, May 1979, doi: 10.1063/1.90629.

[34] D. L. Smith, T. C. McGill, and J. N. Schulman, "Advantages of the HgTe-CdTe superlattice as an infrared detector material," *Applied Physics Letters*, vol. 43, no. 2, pp. 180–182, Jul. 1983, doi: 10.1063/1.94272.

[35] Y. C. Chang and J. N. Schulman, "Interband optical transitions in GaAs-Ga1−xAlxAs and InAs-GaSb superlattices," *Physical Review B*, vol. 31, no. 4, p. 2069, Feb. 1985, doi: 10.1103/PhysRevB.31.2069.

[36] H. Kroemer, Kroemer, and Herbert, "The 6.1 Å family (InAs, GaSb, AlSb) and its heterostructures: a selective review," *PhyE*, vol. 20, no. 3, pp. 196–203, Jan. 2004, doi: 10.1016/J.PHYSE.2003.08.003.

[37] D. L. Smith and C. Mailhiot, "Proposal for strained type II superlattice infrared detectors," *Journal of Applied Physics*, vol. 62, no. 6, p. 2545, Aug. 1987, doi: 10.1063/1.339468.

[38] R. H. Miles, D. H. Chow, J. N. Schulman, and T. C. McGill, "Infrared optical characterization of InAs/Ga1−xInxSb superlattices," *Applied Physics Letters*, vol. 57, no. 8, p. 801, Jun. 1990, doi: 10.1063/1.103425.

[39] D. H. Chow, R. H. Miles, J. N. Schulman, D. A. Collins, and T. C. McGill, "Type II superlattices for infrared detectors and devices," *Semiconductor Science and Technology*, vol. 6, no. 12C, pp. C47–C51, Dec. 1991, doi: 10.1088/0268-1242/6/12C/010.

[40] C. H. Grein, P. M. Young, and H. Ehrenreich, "Minority carrier lifetimes in ideal InGaSb/InAs superlattices," *Applied Physics Letters*, vol. 61, no. 24, p. 2905, Jun. 1992, doi: 10.1063/1.108480.

[41] E. R. Youngdale *et al.*, "Auger lifetime enhancement in InAs–Ga1−xInxSb superlattices," *Applied Physics Letters*, vol. 64, no. 23, p. 3160, Jun. 1994, doi: 10.1063/1.111325.

[42] R. H. Miles, J. N. Schulman, D. H. Chow, and T. C. McGill, "Electronic band structure of far-infrared Ga1-xInxSb/InAs superlattices," *Semiconductor Science and Technology*, vol. 8, no. 1S, pp. S102–S105, Jan. 1993, doi: 10.1088/0268-1242/8/1S/023.

[43] R. M. Feenstra, D. A. Collins, D. Z. Y. Ting, M. W. Wang, and T. C. McGill, "Interface roughness and asymmetry in InAs/GaSb superlattices studied by scanning tunneling microscopy," *Physical Review Letters*, vol. 72, no. 17, p. 2749, Apr. 1994, doi: 10.1103/PhysRevLett.72.2749.

[44] A. Lew, S. Zuo, E. Yu, and R. Miles, "Correlation between atomic-scale structure and mobility anisotropy in InAs/Ga1-xInxSb superlattices," *Physical Review B*, vol. 57, no. 11, p. 6534, Mar. 1998, doi: 10.1103/PhysRevB.57.6534.

[45] J. Steinshnider, J. Harper, M. Weimer, C. H. Lin, S. S. Pei, and D. H. Chow, "Origin of Antimony Segregation in GaInSb/InAs Strained-Layer Superlatices," *Physical Review Letters*, vol. 85, no. 21, p. 4562, Nov. 2000, doi: 10.1103/PhysRevLett.85.4562.

[46] F. Fuchs *et al.*, "High performance InAs/Ga1-xInxSb superlattice infrared photodiodes," *Applied Physics Letters*, vol. 71, no. 22, p. 3251, Jun. 1998, doi: 10.1063/1.120551.

[47] J. L. Johnson *et al.*, "Electrical and optical properties of infrared photodiodes using the InAs/Ga1−xInxSb superlattice in heterojunctions with GaSb," *Journal of Applied Physics*, vol. 80, no. 2, p. 1116, Jun. 1998, doi: 10.1063/1.362849.

[48] M. Walther *et al.*, "256×256 focal plane array midwavelength infrared camera based on InAs/GaSb short-period superlattices," *Journal of Electronic Materials 2005 34:6*, vol. 34, no. 6, pp. 722–725, 2005, doi: 10.1007/S11664-005-0010-Z.

[49] N. Herres *et al.*, "Effect of interfacial bonding on the structural and vibrational properties of InAs/GaSb superlattices," *Physical Review B*, vol. 53, no. 23, pp. 15688–15705, Jun. 1996, doi: 10.1103/PhysRevB.53.15688.

[50] F. Fuchs *et al.*, "InAs/Ga1-xInxSb infrared superlattice diodes: correlation between surface morphology and electrical performance," Oct. 1999, p. 41. doi: 10.1117/12.366728.

[51] B. R. Bennett, "Strain relaxation in InAs/GaSb heterostructures," *Applied Physics Letters*, vol. 73, no. 25, p. 3736, Dec. 1998, doi: 10.1063/1.122878.

[52] G. J. Brown *et al.*, "Type-II superlattice photodetector on a compliant GaAs substrate," *IEEE Photonics Technology Letters*, vol. 12, no. 6, pp. 684–686, Accessed: Jan. 06, 2022. [Online]. Available: https://www.academia.edu/4416396/Type_II_superlattice_photodetector_on _a_compliant_GaAs_substrate

[53] S. Maimon and G. W. Wicks, "nBn detector, an infrared detector with reduced dark current and higher operating temperature," *Applied Physics Letters*, vol. 89, no. 15, p. 151109, Oct. 2006, doi: 10.1063/1.2360235.

[54] S. Maimon, "Reduced Dark Current Photodetector," 7687871-B2, 2010

[55] P. Klipstein, "'XBn' barrier photodetectors for high sensitivity and high operating temperature infrared sensors," Apr. 2008, p. 69402U. doi: 10.1117/12.778848.

[56] P. Y. Delaunay, A. Hood, B. M. Nguyen, D. Hoffman, Y. Wei, and M. Razeghi, "Passivation of type-II InAs∕GaSb double heterostructure," *Applied Physics Letters*, vol. 91, no. 9, p. 091112, Aug. 2007, doi: 10.1063/1.2776353.

[57] J. B. Rodriguez *et al.*, "nBn structure based on InAs∕GaSb type-II strained layer superlattices," *Applied Physics Letters*, vol. 91, no. 4, p. 043514, Jul. 2007, doi: 10.1063/1.2760153.

[58] A. Khoshakhlagh *et al.*, "Bias dependent dual band response from InAs∕Ga(In)Sb type II strain layer superlattice detectors," *Applied Physics Letters*, vol. 91, no. 26, p. 263504, Dec. 2007, doi: 10.1063/1.2824819.

[59] B. M. Nguyen, S. Bogdanov, S. A. Pour, and M. Razeghi, "Minority electron unipolar photodetectors based on type II InAs/GaSb/AlSb superlattices for very long wavelength infrared detection," *Applied Physics Letters*, vol. 95, no. 18, p. 183502, Nov. 2009, doi: 10.1063/1.3258489.

[60] A. D. Hood, A. J. Evans, A. Ikhlassi, D. L. Lee, and W. E. Tennant, "LWIR Strained-Layer Superlattice Materials and Devices at Teledyne Imaging

Sensors," *Journal of Electronic Materials 2010 39:7*, vol. 39, no. 7, pp. 1001–1006, Feb. 2010, doi: 10.1007/S11664-010-1091-X.

[61]   B. M. Nguyen, D. Hoffman, P. Y. Delaunay, and M. Razeghi, "Dark current suppression in type II InAs∕GaSb superlattice long wavelength infrared photodiodes with M-structure barrier," *Applied Physics Letters*, vol. 91, no. 16, p. 163511, Oct. 2007, doi: 10.1063/1.2800808.

[62]   D. Z. Y. Ting *et al.*, "A high-performance long wavelength superlattice complementary barrier infrared detector," *Applied Physics Letters*, vol. 95, no. 2, p. 023508, Jul. 2009, doi: 10.1063/1.3177333.

[63]   J. C. Kim *et al.*, "Controlling interfacial disorder and strain of W-structured type-II superlattices using As2 flux," *Journal of Crystal Growth*, vol. 303, no. 2, pp. 515–519, May 2007, doi: 10.1016/J.JCRYSGRO.2007.01.016.

[64]   O. Salihoglu *et al.*, "'N' structure for type-II superlattice photodetectors," *Applied Physics Letters*, vol. 101, no. 7, p. 073505, Aug. 2012, doi: 10.1063/1.4745841.

[65]   E. K. W. Huang, D. Hoffman, B. M. Nguyen, P. Y. Delaunay, and M. Razeghi, "Surface leakage reduction in narrow band gap type-II antimonide-based superlattice photodiodes," *Applied Physics Letters*, vol. 94, no. 5, p. 053506, Feb. 2009, doi: 10.1063/1.3078282.

[66]   S. Li *et al.*, "Dry etching and surface passivation techniques for type-II InAs/GaSb superlattice infrared detectors," *https://doi.org/10.1117/12.864787*, vol. 7838, no. 13, pp. 318–325, Oct. 2010, doi: 10.1117/12.864787.

[67]   P. Of Spie Spiedigitallibrary *et al.*, "Passivation of type II InAs/GaSb superlattice photodetectors," *https://doi.org/10.1117/12.597140*, vol. 5732, no. 25, pp. 316–325, Mar. 2005, doi: 10.1117/12.597140.

[68]   M. Herrera *et al.*, "Atomic scale analysis of the effect of the SiO2 passivation treatment on InAs/GaSb superlattice mesa sidewall," *Applied Physics Letters*, vol. 93, no. 9, p. 093106, Sep. 2008, doi: 10.1063/1.2977589.

[69]   H. S. Kim *et al.*, "Improved performance of InAs/GaSb strained layer superlattice detectors with SU-8 passivation," *Nanophotonics and Macrophotonics for Space Environments III*, vol. 7467, p. 74670U, Aug. 2009, doi: 10.1117/12.826775.

[70]   M. Razeghi, *Technology of Quantum Devices*. Boston, MA: Springer US, 2010. doi: 10.1007/978-1-4419-1056-1.

[71]   al Z. David Ting *et al.*, "Antimonide-based barrier infrared detectors," *https://doi.org/10.1117/12.851383*, vol. 7660, no. 3, pp. 552–565, May 2010, doi: 10.1117/12.851383.

[72]   B.-M. Nguyen, M. Razeghi, V. Nathan, and G. J. Brown, "Type-II M structure photodiodes: an alternative material design for mid-wave to long wavelength infrared regimes," Feb. 2007, p. 64790S. doi: 10.1117/12.711588.

[73]   A. Rogalski, *Infrared and Terahertz Detectors, Third Edition*. CRC Press, 2019. doi: 10.1201/b21951.

[74]   V. M. More, Y. Kim, J. Jeon, J. C. Shin, and S. J. Lee, "Dual-band unipolar barrier infrared photodetector based on InGaAsSb bulk and type-II InAs/GaSb superlattice absorbers," *Journal of Alloys and Compounds*, vol. 868, p. 159195, Jul. 2021, doi: 10.1016/j.jallcom.2021.159195.

[75]   Z. Jiang *et al.*, "Bias-selectable mid-/long-wave dual band infrared focal plane array based on Type-II InAs/GaSb superlattice," *Infrared Physics & Technology*, vol. 86, pp. 159–164, Nov. 2017, doi: 10.1016/J.INFRARED.2017.08.024.

[76] M. Razeghi *et al.*, "Type II superlattice photodetectors for MWIR to VLWIR focal plane arrays," *https://doi.org/10.1117/12.661170*, vol. 6206, no. 17, pp. 218–224, May 2006, doi: 10.1117/12.661170.

[77] M. Walther *et al.*, "InAs/GaSb type-II short-period superlattices for advanced single and dual-color focal plane arrays," *https://doi.org/10.1117/12.719227*, vol. 6542, pp. 83–90, May 2007, doi: 10.1117/12.719227.

[78] P.-Y. Delaunay, B. M. Nguyen, D. Hoffman, and M. Razeghi, "320 × 256 infrared focal plane array based on type-II InAs/GaSb superlattice with a 12-μm cutoff wavelength," Apr. 2007, p. 654204. doi: 10.1117/12.723832.

[79] H. S. Kim *et al.*, "Mid-IR focal plane array based on type-II InAs∕GaSb strain layer superlattice detector with nBn design," *Applied Physics Letters*, vol. 92, no. 18, p. 183502, May 2008, doi: 10.1063/1.2920764.

[80] E. Plis *et al.*, "nBn based infrared detectors using type-II InAs/(In,Ga)Sb superlattices," Apr. 2008, p. 69400E. doi: 10.1117/12.780375.

[81] F. Rutz *et al.*, "InAs/GaSb superlattice focal plane array infrared detectors: manufacturing aspects," May 2009, p. 72981R. doi: 10.1117/12.819090.

[82] M. Sundaram *et al.*, "SLS technology: the FPA perspective," Apr. 2010, p. 76601P. doi: 10.1117/12.853662.

[83] M. Walther *et al.*, "Defect density reduction in InAs/GaSb type II superlattice focal plane array infrared detectors," Jan. 2011, p. 79451N. doi: 10.1117/12.875159.

[84] M. Razeghi *et al.*, "Advances in antimonide-based Type-II superlattices for infrared detection and imaging at center for quantum devices," *Infrared Physics & Technology*, vol. 59, pp. 41–52, Jul. 2013, doi: 10.1016/j.infrared.2012.12.008.

[85] H. Martijn, C. Asplund, R. M. von Würtemberg, and H. Malm, "High-performance MWIR type-II superlattice detectors," Jun. 2013, p. 87040Z. doi: 10.1117/12.2016602.

[86] H. Katayama *et al.*, "Development status of Type-II superlattice infrared detector in JAXA," *https://doi.org/10.1117/12.2240300*, vol. 9933, no. 4, pp. 21–27, Sep. 2016, doi: 10.1117/12.2240300.

[87] A. Haddadi, A.-M. Hoang, G. Chen, M. Razeghi, and R. Chevallier, "Demonstration of type-II superlattice MWIR minority carrier unipolar imager for high operation temperature application," *Optics Letters, Vol. 40, Issue 1, pp. 45-47*, vol. 40, no. 1, pp. 45–47, Jan. 2015, doi: 10.1364/OL.40.000045.

[88] al Kouhei Miura *et al.*, "High Performance TypeII Superlattice Focal Plane Array with 6μm Cutoff Wavelength," *https://doi.org/10.1117/12.2223634*, vol. 9819, pp. 226–231, May 2016, doi: 10.1117/12.2223634.

[89] X. Zhou *et al.*, "Mid-wavelength type II InAs/GaSb superlattice infrared focal plane arrays," *Infrared Physics & Technology*, vol. 78, pp. 263–267, Sep. 2016, doi: 10.1016/j.infrared.2016.08.014.

[90] P. C. Klipstein *et al.*, "Development and Production of Array Barrier Detectors at SCD," *Journal of Electronic Materials*, vol. 46, no. 9, pp. 5386–5393, Sep. 2017, doi: 10.1007/s11664-017-5590-x.

[91] H. Sharifi *et al.*, "Advances in III-V bulk and superlattice-based high operating temperature MWIR detector technology," Feb. 2017, p. 101770U. doi: 10.1117/12.2266281.

[92] J. Jenkins *et al.*, "Fabrication of small pitch, high definition (HD) 1kx2k/5μm MWIR focal-plane-arrays operating at high temperature (HOT)," Feb. 2017, p. 101771J. doi: 10.1117/12.2267879.

[93] D. Z. Ting *et al.*, "Antimonide e-SWIR, MWIR, and LWIR barrier infrared detector and focal plane array development," in *Infrared Technology and Applications XLIV*, Jul. 2018, p. 37. doi: 10.1117/12.2305248.

[94] M. Razeghi, A. Dehzangi, and J. Li, "Multi-band SWIR-MWIR-LWIR Type-II superlattice based infrared photodetector," *Results in Optics*, vol. 2, p. 100054, Jan. 2021, doi: 10.1016/j.rio.2021.100054.

[95] D. Z. Ting *et al.*, "Mid-wavelength high operating temperature barrier infrared detector and focal plane array," *Applied Physics Letters*, vol. 113, no. 2, p. 021101, Jul. 2018, doi: 10.1063/1.5033338.

[96] H. S. Kim *et al.*, "Suppressed Surface Leakage Current Using nBn Infrared Detector Based on Type II InAs/GaSb Strain Layer Superlattices," in *LEOS 2007 - IEEE Lasers and Electro-Optics Society Annual Meeting Conference Proceedings*, Oct. 2007, pp. 648–649. doi: 10.1109/LEOS.2007.4382573.

[97] M. Razeghi, A. Haddadi, A. Dehzangi, R. Chevallier, and T. Yang, "Recent advances in InAs/InAs$_{1-x}$Sb$_x$/AlAs$_{1-x}$Sb$_x$ gap-engineered type-II superlattice-based photodetectors," Feb. 2017, p. 1017705. doi: 10.1117/12.2267044.

[98] Ö. Dervişoğlu, "A Microbolometer Detector Based on A Sol-Gel Technology," Dissertation for the Degree of Doctor of Philosophy, Middle East Technical University, 2013.